



**Republic of Iraq**  
**Ministry of Higher**  
**Education**  
**and Scientific Research**  
**University of Diyala**  
**College of Science**  
**Department of Physics**

*Structural, Electrical and magnetic properties of  
superparamagnetic  $TiO_2$  mixed  $Zn_xMn_{1-x}Fe_2O_4$  Nanoferrites*

*A Thesis*

*Submitted to The Council of the College of Sciences,  
University of Diyala in Partial Fulfillment of the  
Requirements for the Degree of Master of science in Physics*

*By*

*Muthana Elttayef Abbas*

*B. S.C. in Physics (2006-2007)*

*Supervised By*

*Assit.Prof. Zena Mohammed Ali Abbas*

*2022 AD*

*1443AH*

بِسْمِ اللَّهِ الرَّحْمَنِ الرَّحِيمِ

(أَوْ كَظُلُمَاتٍ فِي بَحْرٍ لُجِّيٍّ يَغْشَاهُ مَوْجٌ مِّنْ فَوْقِهِ مَوْجٌ مِّنْ فَوْقِهِ سَحَابٌ ظُلُمَاتٌ  
بَعْضُهَا فَوْقَ بَعْضٍ إِذَا أَخْرَجَ يَدَهُ لَمْ يَكَدْ يَرَاهَا ۗ وَمَنْ لَّمْ يَجْعَلِ اللَّهُ لَهُ نُورًا فَمَا لَهُ مِنْ  
نُّورٍ)

صدق الله العظيم

سورة النور

الآية 40

*Dedication*

*My M.Sc. is dedicated to...*

*My merciful parents.*

*My lovely wife.*

*My beautiful children.....Ellen and Taleen*

*Muthana El ttayef Abbas*

*2022*

## ***Acknowledgments***

I would like to express my sincere gratitude to the Assistant supervisor ***Assistant Professor Zena Mohammed Ali abbas***, thank ***Prof. Dr. Tahseen Hussein Mubarak, Dr. Ziad Tariq Khodair*** thank ***Dr. Sabah Anwer Salman, Dr. Ammar A. Habeeb*** thank ***Dr. Mohammad Hameed*** and all my professors in the Physics department who gave me the opportunity. perform this research. I am indebted to them for their suggestions and valuable remarks. special thanks are extended to the Dean of the College of Science and all the staff of the Department of Physics for their assistance.

To the one who honored me by bearing his name, ***my Dear father***.. To the light of my eyes, the light of my path, and the joy of my life, ***my mother***, To ***my dear wife***, thank you for always being by my side, taking care of me and supporting me from the bottom of my heart. Thank you for every moment that you accompanied me during my study period and for your encouragement to me. I ask God to give you goodness and open the doors of His mercy for you. To my beautiful flowers, ***Elaine*** and ***Taleen***.and to my supporters ***brothers*** and ***sisters***.I certainly cannot mention the names of everyone who contributed towards the success of this research, but as they have always known, I am very grateful.

**Muthana El ttayef Abbas**

**2022**

## ***Supervisors Certification***

I certify that this thesis entitled, ***Structural, Electrical and magnetic properties of superparamagnetic TiO<sub>2</sub> mixed Zn<sub>x</sub>Mn<sub>1-x</sub>Fe<sub>2</sub>O<sub>4</sub> Nanoferrites***, for the student (***Muthana Elttayef Abbas***), was prepared under supervisions at the Department of Physics, College of Science, Diyala University in part, of the prerequisites for the awarding the M.Sc in Physics.

Signature:

Name: ***Assit.Prof. Zena  
Mohammed Ali Abbas***

Title: ***Assist. Prof.***

Address: College of Science

University of Diyala

Date:     /     / 2022

## ***Head of the Physics Department***

In view of available recommendation, I forward this thesis for debate by the examining committee.

Signature:

Name: ***Dr. AmmarA. Habeeb***

Title: *Assist. Professor*

Head of the Physics Department

Address: College of Science, University of Diyala

Date:    /    / 2022

## ***Linguistic Amendment***

I certify that the thesis entitled " ***Structural, Electrical and magnetic properties of superparamagnetic TiO<sub>2</sub> mixed Zn<sub>x</sub>Mn<sub>1-x</sub>Fe<sub>2</sub>O<sub>4</sub> Nanoferrites*** " presented by student (***Muthana El ttayef Abbas*** ) has been corrected linguistically, therefore, it is suitable for debate by examining committee.

Signature:

Name: ***Dr.***

Title: ***Professor***

Address: ***University of Diyala /College of Sciences***

Date:    /    / 2022

## ***Scientific Amendment***

I certify that the thesis entitled " ***Structural, Electrical and magnetic properties of superparamagnetic TiO<sub>2</sub> mixed Zn<sub>x</sub>Mn<sub>1-x</sub>Fe<sub>2</sub>O<sub>4</sub> Nanoferrites*** " presented by student (***Muthana El ttayef Abbas*** ) has been evaluated scientifically, therefore, it is suitable for debate by examining committee.

Signature:

Name: **Dr. Nadia Abbas Ali**

Title: *Professor*

Address:

Date:    /    / 2022

## ***Scientific Amendment***

I certify that the thesis entitled " ***Structural, Electrical and magnetic properties of superparamagnetic TiO<sub>2</sub> mixed Zn<sub>x</sub>Mn<sub>1-x</sub>Fe<sub>2</sub>O<sub>4</sub> Nanoferrites*** " presented by student (***Muthana El ttayef Abbas*** ) has been evaluated scientifically, therefore, it is suitable for debate by examining committee.

Signature:

Name: **Dr.Enas Mohi Hadi**

Title: *Professor*

Address: Date:    /    / 2022

## ***Examination Committee Certificate***

We certify that we have read this thesis entitled " ***Structural Electrical and magnetic properties of superparamagnetic titanium doped Mn-Zn nanoferrites for high frequency applications*** " and, as an examining committee, we examined the student (***Muthana El ttayef Abbas*** ) on its content, and in what is related to it, and that in our opinion it meets the standard of a thesis for the degree of master in Physics Sciences.

Signature

Name: **Dr.Sabah Anwer Salman**

Title: *Professor*

Address: *University of*

Data:    /    / 2022

(Chairman)

Signature

Name: **Dr.Ali Ahmed Yousif**

Title: *Professor*

Address: *University of*

Data:    /    / 2022

(Member)

Signature

Name:**Dr.ZiadTariqKhodair**

Title: *Assist. Professor*

Address: *University of*

Data:    /    / 2022

(Member)

Signature

Name: *Assit. Prof. Zena Mohammed*

*Ali Abbas*

Title: *Professor*

Address: *University of*

Data: / / 2022

(Member /Supervisor)

Approved by the Council of the College of Science.

(The Dean)

Signature:

Name: *Dr. Tahseen H. Mubarak*

Title: *Professor*

Date: / /2022

## Contents

<i>No.</i>	<i>Subjects</i>	<i>Page No.</i>
	Contents	I
	List of Figures	VII
	List of Tables	XVII
	List of Symbols	XX
	List of Abbreviations	XXII
	Abstract	XXIII

---

### *Chapter One*

#### *Concept of Nanoparticles and Literature Review*

1.1	Introduction	1
1.2	Literature Review	2
1.3	Aim of the Study	8

---

### *Chapter Two*

#### *Theoretical Part*

2.1	Introduction	9
2.2	Origin of Magnetism	9
2.3	Magnetic properties	10
2.4	Types of Magnetic Materials	11
2.4.1	Diamagnetism	12
2.4.2	Paramagnetic materials	13

2.4.3	Ferromagnetic materials	14
2.4.4	Antiferromagnetism	15
2.4.5	Ferrimagnetism	16
2.5	Titanium Dioxide	17
2.6	Ferrite Materials	17
2.6.1	Spinel Ferrite	18
2.6.1.1	Normal Spinel	19
2.6.1.2	Inverse Spinel	19
2.6.1.3	Random (mixed) spinel	19
2.6.2	Garnet Ferrite	19
2.6.3	Hexagonal Ferrite	20
2.7	Characterization of Mn-Zn-Ferrite	20
2.8	Magnetic materials types	20
2.8.1	Soft magnetic materials	21
2.8.2	Hard magnetic materials	21
2.9	Dielectric properties	22
2.10	Structural Properties of ferrites	23
2.10.1	Lattice Constant (a)	24
2.10.2	Spacing of Lattice Planes	24
2.10.3	Average crystallite Size	25
2.11	Applications of the hard ferrites	25
2.12	Fourier Transform Infrared (FTIR) spectroscopy	26
2.13	Vibrating sample magnetometer	27
2.14	Hysteresis loop and magnetic parameters	27

2.15	Dielectric Parameters	30
2.16	Electrical Conductivity	31
2.17	Preparation Methods	32
2.17.1	Sol-Gel Auto Combustion method	32
2.18	Polarization	34
2.19	Types of Polarization	34
2.19.1	Electronic or Induced Polarization	34
2.19.2	Atomic or Ionic Polarization	34
2.19.3	Dipolar or Orientation Polarization	34
2.19.4	Interfacial or Space Charge Polarization	35

### *Chapter three*

### *Experimental Part*

3.1	Introduction	36
3.2	The devices used	36
3.2.1	Mass Measurement Instrument	36
3.2.2	Magnetic Stirrer	38
3.2.3	Electrical furnace	37
3.2.4	Hydraulic press	38
3.3	The materials used	38
3.4.1	Preparation of (Zn Mn Fe <sub>2</sub> O <sub>4</sub> )	39

3.4.2	Preparation of (Zn Mn Fe <sub>2</sub> O <sub>4</sub> /TiO <sub>2</sub> ) nano composites	40
3.5	Calcinations and Pellet Formation	41
3.6	Measurements and testing	43
3.6.1	X-ray Diffraction (XRD)	43
3.6.2	Fourier Transform Infrared (FTIR)	43
3.6.3	Field emission scanning electron microscopy (FE-SEM)	44
3.6.4	Energy - Dispersive X - ray Spectroscopy (EDS)	45
3.7	Magnetic properties measurements	45
3.7.1	Vibrating Sample Magnetometer (VSM)	45
3.8	The Electrical Properties Measurements	46

---

## *Chapter Four*

### *Result and Discussion*

4.1	Introduction	48
4.2	Structural Characterization	48
4.2.1	X-ray Diffraction (XRD) of $\text{MnFe}_2\text{O}_4$ , $\text{Zn}_x\text{Mn}_{1-x}\text{Fe}_2\text{O}_4$ , and $\text{Zn}_x\text{Mn}_{1-x}\text{Fe}_2\text{O}_4/\text{TiO}_2$ prepared by Sol-Gel method	48
4.2.2	Field Emission Scanning Electron Microscopy (FE-SEM) of $(\text{Zn}_x\text{Mn}_{1-x}\text{Fe}_2\text{O}_4)$	53
4.2.3	Field Emission Scanning Electron Microscopy (FE-SEM) of $(\text{Zn}_{0.45}\text{Mn}_{0.55}\text{Fe}_2\text{O}_4/\text{TiO}_2)$	57
4.2.4	Energy Dispersive Spectroscopy (EDS) of $(\text{Zn}_x\text{Mn}_{1-x}\text{Fe}_2\text{O}_4)$	58
4.2.5	Energy Dispersive Spectroscopy (EDS) of $\text{Zn}_{0.45}\text{Mn}_{0.55}\text{Fe}_2\text{O}_4/\text{TiO}_2$	61
4.2.6	Fourier Transform Infrared (FT-IR) spectrum of $(\text{Zn}_x\text{Mn}_{1-x}\text{Fe}_2\text{O}_4)$ and $\text{Zn}_x\text{Mn}_{1-x}\text{Fe}_2\text{O}_4/\text{TiO}_2$	63
4.3	Magnetization Characterization	70
4.3.1	Vibrating Sample Magnetometer (VSM) analysis of $(\text{Zn}_x\text{Mn}_{1-x}\text{Fe}_2\text{O}_4)$ and $\text{Zn}_x\text{Mn}_{1-x}\text{Fe}_2\text{O}_4/\text{TiO}_2$	70

4.4	Electrical Characterization	78
4.4.1	Electrical Properties of $(\text{Zn}_x\text{Mn}_{1-x}\text{Fe}_2\text{O}_4)/\text{and}$ $\text{Zn}_x\text{Mn}_{1-x}\text{Fe}_2\text{O}_4 / \text{TiO}_2$	79
4.4.1.1	Dielectric constant	79
4.4.1.2	Dielectric loss	84
4.4.1.3	Dielectric loss ( $\tan \delta$ )	88
4.4.1.4	AC conductivity	93
4.5	Conclusions	107
4.6	Future Work	108
References		

## List of Figures

No.	Title	Page No.
2.1	Schematic magnetic phenomena in a 1D crystal: (a) paramagnetism; (b) ferromagnetism; (c) antiferromagnetism; (d) ferrimagnetism	11
2.2	Periodic table showing different kinds of magnetic materials	12
2.3	(a) Diamagnetic material: When $H=0$ , the atoms have no magnetic moment, hence $M=0$ . (b) When a magnetic field $H_0$ is applied to the atoms, the atoms acquire an induced magnetic moment in the opposite direction of the applied field, resulting in negative susceptibility	13
2.4	Each atom in a paramagnetic substance has a permanent magnetic moment. All magnetic moments are randomly orientated when $H=0$ , hence $M=0$ . (b) When a magnetic field of $H_0$ is applied, the atomic magnetic moments prefer to align themselves with the field's direction. As a result, the has a net magnetization $M=M_0$ and a positive susceptibility	14
2.5	Ferromagnetism	15
2.6	Antiferromagnetism	16
2.7	Ferrimagnetism	16
2.8	The structure of titanium dioxide	17
2.9	Schematic representation of spinel structure	18
2.10	Comparison of hysteresis loops for: (a) soft ferrites; (b) hard ferrites	22
2.11	Schematic representation of x-ray diffraction	24
2.12	Block diagram of FTIR	26

2.13	Schematic diagram of vibrating sample magnetometer system	27
2.14	Hysteresis loop for ferromagnetic materials	28
2.15	Phase diagram between voltage and current	31
2.16	Schematic diagram of (a) Electronic polarization, (b) Ionic polarization, (c) Orientation polarization, (d) Space-charge polarization	35
3.1	The diagram of sol-gel auto combustion synthesis of $Zn_xMn_{1-x}Fe_2O_4$ Nano ferrites and $Zn_{0.45}Mn_{0.55}Fe_2O_4/TiO_2$ nanocomposites.	36
3.2	Electric Balance used	37
3.3	Magnetic stirrer	38
3.4	Electrical furnace	38
3.5	Hydraulic press	41
3.6	Photograph of (a) nitrates-citrate solution, (b) The solution after the Adding of ammonia, (c) dry gel, (d) Dry bulk temperature of 150°C, (e) Dry bulk temperature of 250°C and (f) auto combustion and become Nano powder ferrite	41
3.7	Transformation of powder to compact sample	42
3.8	Photograph of X-ray diffraction instrument	43
3.9	FTIR spectrophotometer	44
3.10	Photograph of field emission scanning electron microscopy instrument	45
3.11	Photograph of vibrating sample magnetometer (VSM) instrument	46
3.12	Photograph of LCR meter instrument	47

4.1	XRD patterns of $\text{MnFe}_2\text{O}_4$ ferrite at different calcination temperatures (650, 750, 850 °C)	49
4.2	XRD patterns of $\text{Zn}_{0.15}\text{Mn}_{0.85}\text{Fe}_2\text{O}_4$ ferrite at different calcination temperatures (650, 750, 850 °C)	49
4.3	XRD patterns of $\text{Zn}_{0.25}\text{Mn}_{0.75}\text{Fe}_2\text{O}_4$ ferrite at different calcination temperatures (650, 750, 850 °C)	50
4.4	XRD patterns of $\text{Zn}_{0.35}\text{Mn}_{0.65}\text{Fe}_2\text{O}_4$ ferrite at different calcination temperatures (650, 750, 850 °C)	50
4.5	XRD patterns of $\text{Zn}_{0.45}\text{Mn}_{0.55}\text{Fe}_2\text{O}_4$ ferrite at different calcination temperatures (650, 750, 850 °C)	51
4.6	XRD patterns of (a) pure $\text{TiO}_2$ , (b), (c), (d), (e) and (f) are $\text{Zn}_{0.45}\text{Mn}_{0.55}\text{Fe}_2\text{O}_4$ mixed with different ratios of $\text{TiO}_2$ (20, 30, 40, 50 and 60%) respectively	51
4.7	FE-SEM micrographs of $\text{MnFe}_2\text{O}_4$ nanoferrites for (a) calcined specimen at 650 °C (c) at 750 °C and (c) at 850 °C	54
4.8	FE-SEM micrographs of $\text{Zn}_{0.15}\text{Mn}_{0.85}\text{Fe}_2\text{O}_4$ nanoferrites for (a) calcined specimen at 650 °C (c) at 750 °C and (c) at 850 °C.	54
4.9	FE-SEM micrographs of $\text{Zn}_{0.25}\text{Mn}_{0.75}\text{Fe}_2\text{O}_4$ nanoferrites for (a) calcined specimen at 650 °C (c) at 750 °C and (c) at 850 °C	55
4.10	FE-SEM micrographs of $\text{Zn}_{0.35}\text{Mn}_{0.65}\text{Fe}_2\text{O}_4$ nanoferrites for (a) calcined specimen at 650 °C (c) at 750 °C and (c) at 850 °C	55
4.11	FE-SEM micrographs of $\text{Zn}_{0.45}\text{Mn}_{0.55}\text{Fe}_2\text{O}_4$ nanoferrites for (a) calcined specimen at 650 °C (c) at 750 °C and (c) at 850 °C	56

4.12	: FE-SEM of $(\text{Zn}_{0.45}\text{Mn}_{0.55}\text{Fe}_2\text{O}_4)$ mixed with different ratios of $\text{TiO}_2$ (20%, 30%, 40%, 50% and 60%) respectively	58
4.13	EDS spectra of $\text{MnFe}_2\text{O}_4$ nanoferrites for (a) calcined specimen at 650. (b) at 750. and (c) at 850	59
4.14	EDS spectra of $\text{Zn}_{0.15}\text{Mn}_{0.85}\text{Fe}_2\text{O}_4$ nanoferrites for (a) calcined specimen at 650. (b) at 750. and (c) at 850	59
4.15	EDS spectra of $\text{Zn}_{0.25}\text{Mn}_{0.75}\text{Fe}_2\text{O}_4$ nanoferrites for (a) calcined specimen at 650. (b) at 750. and (c) at 850	60
4.16	EDS spectra of $\text{Zn}_{0.35}\text{Mn}_{0.65}\text{Fe}_2\text{O}_4$ nanoferrites for (a) calcined specimen at 650. (b) at 750. and (c) at 850	60
4.17	EDS spectra of $\text{Zn}_{0.45}\text{Mn}_{0.55}\text{Fe}_2\text{O}_4$ nanoferrites for (a) calcined specimen at 650. (b) at 750. and (c) at 850	61
4.18	EDS spectra of $\text{Zn}_{0.45}\text{Mn}_{0.55}\text{Fe}_2\text{O}_4$ nanoferrites mixed with ratio different $\text{TiO}_2$ for (a) 20%, (b) 30%, (c) 40%, (d) 50%, (e) 60%	63
4.19	FT-IR spectrum of $\text{MnFe}_2\text{O}_4$ ferrite at different calcination temperatures (650, 750, and 850 °C) by sol-gel method	65
4.20	FT-IR spectrum of $\text{Zn}_{0.15}\text{Mn}_{0.85}\text{Fe}_2\text{O}_4$ ferrite at different calcination temperatures (650, 750, and 850 °C) by sol-gel method	65
4.21	FT-IR of $\text{Zn}_{0.25}\text{Mn}_{0.75}\text{Fe}_2\text{O}_4$ ferrite at different calcination temperatures (650, 750, and 850 °C) by sol-gel method	66
4.22	FT-IR spectrum of $\text{Zn}_{0.35}\text{Mn}_{0.65}\text{Fe}_2\text{O}_4$ ferrite at different calcination temperatures (650, 750, and 850 °C) by sol-gel method	66

4.23	FT-IR spectrum of $Zn_{0.45}Mn_{0.55}Fe_2O_4$ ferrite at different calcination temperatures (650, 750, and 850 °C) by sol-gel method	67
4.24	FTIR spectrum of $Zn_{0.45}Mn_{0.55}Fe_2O_4$ mixed with different ratios of $TiO_2$ (20%, 30%, 40%, 50% and 60%) respectively	68
4.25	(a-b): VSM analysis of $MnFe_2O_4$ ferrite at different calcination temperatures (650, 750, and 850 °C)	73
4.26	VSM analysis of $Zn_{0.15}Mn_{0.85}Fe_2O_4$ ferrite at different calcination temperatures (650, 750, and 850 °C)	74
4.27	VSM analysis of $Zn_{0.25}Mn_{0.75}Fe_2O_4$ ferrite at different calcination temperatures (650, 750, and 850 °C)	74
4.28	VSM analysis of $Zn_{0.35}Mn_{0.65}Fe_2O_4$ ferrite at different calcination temperatures (650, 750, and 850 °C)	75
4.29	(a-b): VSM analysis of $Zn_{0.45}Mn_{0.55}Fe_2O_4$ ferrite at different calcination temperatures (650, 750, and 850 °C).	76
4.30	VSM analysis of $Zn_{0.45}Mn_{0.55}Fe_2O_4$ mixed with different ratios of $TiO_2$ (20, 30, 40, 50 and 60%) respectively.	77
4.31	Frequency dependence of real part ( $\epsilon'$ ) of $MnFe_2O_4$ ferrite at different calcination temperatures (400, 600, 800 °C).	81
4.32	Frequency dependence of real part ( $\epsilon'$ ) of $Zn_{0.15}Mn_{0.85}Fe_2O_4$ ferrite at different calcination temperatures (400, 600, 800 °C).	82
4.33	Frequency dependence of real part ( $\epsilon'$ ) of $Zn_{0.25}Mn_{0.75}Fe_2O_4$ ferrite at different calcination temperatures (400, 600, 800 °C).	82

4.34	Frequency dependence of real part ( $\epsilon'$ ) of $\text{Zn}_{0.35}\text{Mn}_{0.65}\text{Fe}_2\text{O}_4$ ferrite at different calcination temperatures (400, 600, 800 °C)	83
4.35	Frequency dependence of real part ( $\epsilon'$ ) of $\text{Zn}_{0.45}\text{Mn}_{0.55}\text{Fe}_2\text{O}_4$ ferrite at different calcination temperatures (400, 600, 800 °C).	83
4.36	Frequency dependence of real part ( $\epsilon'$ ) of $\text{TiO}_2$ $\text{Zn}_{0.45}\text{Mn}_{0.55}\text{Fe}_2\text{O}_4$ mixed with different ratios of $\text{TiO}_2$ (20, 30, 40, 50 and 60%) respectively.	84
4.37	variation of ( $\epsilon''$ ) with f (Hz) of $\text{MnFe}_2\text{O}_4$ ferrite at different calcination temperatures (400, 600, and 800 °C).	85
4.38	variation of ( $\epsilon''$ ) with f (Hz) of $\text{Zn}_{0.15}\text{Mn}_{0.85}\text{Fe}_2\text{O}_4$ ferrite at different calcination temperatures (400, 600, 800 °C).	86
4.39	variation of ( $\epsilon''$ ) with f (Hz) of $\text{Zn}_{0.25}\text{Mn}_{0.75}\text{Fe}_2\text{O}_4$ ferrite at different calcination temperatures (400, 600, 800 °C).	86
4.40	variation of ( $\epsilon''$ ) with f (Hz) of $\text{Zn}_{0.35}\text{Mn}_{0.65}\text{Fe}_2\text{O}_4$ ferrite at different calcination temperatures (400, 600, 800 °C).	87
4.41	variation of ( $\epsilon''$ ) with f (Hz) of $\text{Zn}_{0.45}\text{Mn}_{0.55}\text{Fe}_2\text{O}_4$ ferrite at different calcination temperatures (400, 600, 800 °C)	87
4.42	variation of ( $\epsilon''$ ) with f (Hz) of $\text{TiO}_2$ $\text{Zn}_{0.45}\text{Mn}_{0.55}\text{Fe}_2\text{O}_4$ mixed with different ratios of $\text{TiO}_2$ (20%, 30%, 40%, 50% and 60%) respectively	88
4.43	variation of $\tan\delta$ with f (Hz) of $\text{MnFe}_2\text{O}_4$ ferrite at different calcination temperatures (400, 600, and 800 °C)	90
4.44	variation of $\tan\delta$ with f (Hz) of $\text{Zn}_{0.15}\text{Mn}_{0.85}\text{Fe}_2\text{O}_4$ ferrite at different calcination temperatures (400, 600, and 800 °C)	90

4.45	variation of $\tan\delta$ with $f$ (Hz) of $\text{Zn}_{0.25}\text{Mn}_{0.75}\text{Fe}_2\text{O}_4$ ferrite at different calcination temperatures (400, 600, and 800 °C)	91
4.46	variation of $\tan\delta$ with $f$ (Hz) of $\text{Zn}_{0.35}\text{Mn}_{0.65}\text{Fe}_2\text{O}_4$ ferrite at different calcination temperatures (400, 600, 800 °C)	91
4.47	variation of $\tan\delta$ with $f$ (Hz) of $\text{Zn}_{0.45}\text{Mn}_{0.55}\text{Fe}_2\text{O}_4$ ferrite at different calcination temperatures (400, 600, 800 °C)	92
4.48	variation of $\tan\delta$ with $f$ (Hz) of $\text{TiO}_2$ $\text{Zn}_{0.45}\text{Mn}_{0.55}\text{Fe}_2\text{O}_4$ mixed with different ratios of $\text{TiO}_2$ (20%, 30%, 40%, 50% and 60%) respectively	92
4.49	The AC conductivity of $\text{MnFe}_2\text{O}_4$ ferrite at different calcination temperatures (400, 600, and 800 °C)	94
4-50	The AC conductivity of $\text{Zn}_{0.15}\text{Mn}_{0.85}\text{Fe}_2\text{O}_4$ ferrite at different calcination temperatures (400, 600, and 800 °C)	95
4-51	The AC conductivity of $\text{Zn}_{0.25}\text{Mn}_{0.75}\text{Fe}_2\text{O}_4$ ferrite at different calcination temperatures (400, 600, and 800 °C)	95
4-52	The AC conductivity of $\text{Zn}_{0.35}\text{Mn}_{0.65}\text{Fe}_2\text{O}_4$ ferrite at different calcination temperatures (400, 600, and 800 °C)	96
4-53	The AC conductivity of $\text{Zn}_{0.45}\text{Mn}_{0.55}\text{Fe}_2\text{O}_4$ ferrite at different calcination temperatures (400, 600, 800 °C)	96
4-54	The AC conductivity of $\text{Zn}_{0.45}\text{Mn}_{0.55}\text{Fe}_2\text{O}_4$ mixed with different ratios of $\text{TiO}_2$ (20, 30, 40, 50 and 60%)	97
	respectively	

## List of Tables

No.	Title	Page No.
2.1	Types of Magnetism	12
3.1	The chemical materials and their properties	39
4.1	XRD calculations of $Zn_xMn_{1-x}Fe_2O_4$ with different content of zinc metal ( $x=0, 0.15, 0.25, 0.35$ and $0.45$ ) at different calcination temperatures.	52
4.2	XRD calculations of $Zn_{0.45}Mn_{0.55}Fe_2O_4$ mixed with different content of $TiO_2$	52
4.3	Average crystallite size and particle size of $Zn_xMn_{1-x}Fe_2O_4$ nanoferrites ( $x = 0, 0.15, 0.25, 0.35,$ and $0.45$ ) for diferent calcined temperature determined from XRD and FE-SEM.	56
4.4	FT-IR measurements of $Zn_xMn_{1-x}Fe_2O_4$ with different content of zinc metal ( $x=0, 0.15, 0.25, 0.35$ and $0.45$ ) at different calcination temperatures	69
4.5	FT-IR measurements of $Zn_{0.45}Mn_{0.55}Fe_2O_4$ mixed with different content of $TiO_2$	70
4.6	VSM measurements of $MnFe_2O_4$ with different content of zinc metal at different calcination temperatures ( $650, 750,$ and $860$ ) °C	77
4.7	VSM measurements of $Zn_{0.15}Mn_{0.85}Fe_2O_4$ with different content of zinc metal at different calcination temperatures ( $650, 750,$ and $860$ ) °C	77

4.8	VSM measurements of $Zn_{0.25}Mn_{0.75}Fe_2O_4$ with different content of zinc metal at different calcination temperatures (650, 750, and 860) °C	78
4.9	VSM measurements of $Zn_{0.35}Mn_{0.65}Fe_2O_4$ with different content of zinc metal at different calcination temperatures (650, 750, and 860) °C	78
4.10	VSM measurements of $Zn_{0.45}Mn_{0.55}Fe_2O_4$ with different content of zinc metal at different calcination temperatures (650, 750, and 860) °C.	78
4.11	VSM measurements of $Zn_{0.45}Mn_{0.55}Fe_2O_4$ mixed with different content of $TiO_2$ .	78
4.12	LCR measurements the dielectric parameters ( $\epsilon''$ ), ( $\epsilon'$ ), ( $\tan \delta$ ) and ( $\sigma_{ac}$ ) of $MnFe_2O_4$ with at different calcination temperatures (400, 600, and 800) °C.	97
4.13	LCR measurements of the dielectric parameters ( $\epsilon''$ ), ( $\epsilon'$ ), ( $\tan \delta$ ) and ( $\sigma_{ac}$ ) of $Zn_{0.15}Mn_{0.85}Fe_2O_4$ with at different calcination temperatures (400, 600, 800) °C.	99
4.14	LCR measurements the dielectric parameters ( $\epsilon''$ ), ( $\epsilon'$ ), ( $\tan \delta$ ) and ( $\sigma_{ac}$ ) of $Zn_{0.25}Mn_{0.75}Fe_2O_4$ with at different calcination temperatures (400, 600, and 800) °C.	100
4.15	LCR measurements the dielectric parameters ( $\epsilon''$ ), ( $\epsilon'$ ), ( $\tan \delta$ ) and ( $\sigma_{ac}$ ) of $Zn_{0.35}Mn_{0.65}Fe_2O_4$ with at different calcination temperatures (400, 600, and 800) °C.	102
4.16	LCR measurements the dielectric parameters ( $\epsilon''$ ), ( $\epsilon'$ ), ( $\tan \delta$ ) and ( $\sigma_{ac}$ ) of $Zn_{0.45}Mn_{0.55}Fe_2O_4$ with at different calcination temperatures (400, 600, and 800) °C.	103
4.17	LCR measurements the dielectric parameters ( $\epsilon''$ ), ( $\epsilon'$ ), ( $\tan \delta$ ) and ( $\sigma_{ac}$ ) of $Zn_{0.45}Mn_{0.55}Fe_2O_4$ nanocomposite mixed with different content of $TiO_2$ .	105

## List of Symbols

<i>Symbol</i>	<i>Definition</i>
$\theta$	Bragg's angle
$\lambda$	Wavelength
$M$	Magnetization
$H$	Magnetic field
$M_S$	Saturation magnetization
$H_c$	Coercivity
$M_r$	Remanence magnetization
$n_B$	Magnetic moment
$K$	Magnetic anisotropy
$T$	Temperature
$a$	Lattice parameters
$\epsilon'$	Dielectric constant
$\epsilon''$	Dielectric loss factor
$\tan \delta$	Dielectric loss angle
$\sigma_{ac}$	ac conductivity
$T_c$	Curie temperature
$T_N$	Neel temperature,
$\mu_r$	Relative permeability
$\mu_o$	Vacuum permeability

$\mu$	Permeability of specific medium
$\chi$	Susceptibility
$\chi_m$	Magnetic susceptibility
$c$	Curie constant.
$P$	Polarization
$C$	Capacitance
$C_o$	Capacitance of air
$f$	Frequency
$d$	Spacing between the atomic planes
$D$	Crystallite size
$hkl$	Miller indices
$\rho_x$	X-ray density
$M$	Molecular weight
$^{\circ}\text{C}$	Degrees celsius
$P_e$	Electric polarization
$P_i$	Ionic polarization
$P_o$	Orientation polarization
$P_s$	Space-charge polarization
$D_c$	Critical diameter
$\alpha$	Polarizability
$E_a$	Activation energy

## List of Abbreviations

<i>Abbreviations</i>	<i>Definition</i>
NPs	Nanoparticles
NCs	Nano composites
XRD	X-ray diffraction
TEM	Transmission electron microscopy
FT-IR	Fourier transform infrared spectroscopy
SEM	Scanning electron microscopy
FE-SEM	Field emission-scanning electron microscopes
VSM	Vibrating sample magnetometer
MRI	Magnetic resonance imaging
FWHM	Full width at half-maximum
PXRD	Powder X-ray diffraction
GMR	Giant magneto resistance

## **Abstract**

The objective of this thesis is to synthesize and study the structural, magnetic and electrical properties of nanoparticles made of ferrite zinc manganese using the stoichiometric formula  $Zn_xMn_{1-x}Fe_2O_4$  ( $X= 0, 0.15, 0.25, 0.35, \text{ and } 0.45$ ) respectively, were prepared using the sol-gel auto-combustion process. After combustion, the as-burnt powders were calcined at 650, 750, and 850 °C for 2 hrs to increase homogeneity and remove organic waste, where the as-burnt specimens and the specimens that calcined at 650, 750, and 850 °C added with a five-drop PVA as a binder to press it into circular pellets of diameter 1cm with thickness about 3 mm. The prepared pellets were sintered at 400, 600, and 800 °C for 2 hrs to intensify of the specimens and, slowly allowed to be cooled naturally to examine the dielectric properties. Another purpose of this work is to blend and study the structural, magnetic and electrical properties of zinc manganese nitrate ferrite and titanium nanocomposites at 500 using the formula  $ZnMnFe_2O_4/TiO_2$  in different proportions (20%, 30%, 40%, 50% and 60%) respectively. prepared using the traditional ceramic method. The best results were the crystal size in this paper with a size of 15 to 38 nm with a cubic structure which was determined by XRD, while the crystal size of Mn-Zn-ferrites/ $TiO_2$  was from 10 to 30 nm with a cubic structure determined by X-ray diffraction (XRD) analyses. FE-SEM reveled Nano ferrites ( $ZnMnFe_2O_4$ ) having a particle size of 25 to

66 nm were found. While the particle size of  $Zn_xMn_{1-x}Fe_2O_4/TiO_2$  the range from 37 to 72 nm. It observed the result is less than the Zn-Mn- $Fe_2O_4$  nano composite.

Prominent FT- IR absorption peaks at 400 and 500  $cm^{-1}$  indicated the presence of Fe-O, Mn-O, and Zn-O vibrational bands. Results from the VSM demonstrated that the magnetic nature of materials changed dramatically from pristine as magnetization rose and coercivity decreased with Mn-Zn-ferrites nanoparticles. Finally, an optimal magnetic parameter value ( $M_s = 0.80$  emu/g and  $H_c = 75$  Oe) at (850) °C was obtained from the data. The dielectric properties are measured using a (LCR) meter in the frequency range of (200Hz-1MHz) at room temperature. The dielectric constant ( $\epsilon'$ ), dielectric loss angle ( $\tan\delta$ ) and dielectric loss factor ( $\epsilon''$ ) are for Mn-Zn- $Fe_2O_4$  nanoferrites at 400, 600, and 800 °C and Mn-Zn- $Fe_2O_4/TiO_2$  nanocomposites in different proportions (20%, 30%, 40%, 50% and 60%) respectively are found to decrease with increasing temperatures. The prepared pellets were sintered at 500 °C for 2 hrs to intensify of the specimens and slowly allowed to be cooled naturally to examine the dielectric properties.



---

# Chapter one

---

Introduction & Literature  
Review





## 1.1 Introduction

Researchers are continuous work on new materials that could be applied to a range of industries. fabric, glass, wood, metals, ceramics, alloys, petroleum fuels, radioactive materials, polymers, coal, stone, semiconductors, and other materials have ushered in significant advances in humanity's history. The investigation of innovative materials with superior properties, on the other hand, stretches back to the stone age. The study of material synthesis and properties has only recently emerged as a distinct field of science with technical and practical ramifications. In the domains of physics and other sciences, nanotechnology is one of the most important and intriguing technologies. It has made a significant contribution to the events of great scientific revolutions that are hoped to change the course of technologies and applied sciences, as it provides a high ability to settings and control in the composition of matter at the level of atomic dimensions, as well as a high potential in nanofabrication, resulting in amazing physical qualities and properties. because of this nanotechnology has been used to create systems and devices with unique features by manipulating the form and size of the nanosphere [1]. Due to the enormous ratio of the surface of the grains to their size, magnetic materials in general, and nanoferrite in particular, have a significant impact on physical, electrical, and magnetic properties. Due to its magnetic properties and a wide range of uses, nanoferrite has sparked interest in the sphere of science and technology in recent years [2]. High frequency transformer cores, antenna bars, and choke coils are all made of ferrites [3,4]. nanoelectronic devices, integrated circuits, and magnetic resonance imaging (MRI) are all examples of this [5-8]. The typical formula for ferrites is  $(MFe_2O_4)$ , where M represents , one of the divalent metallic elements ( $Zn^{+2}, Cu^{+2}, Fe^{+2}, Mg^{+2}$ ). The ferrites are divided into three groups based on their chemical composition: Garnet, Hexagonal and Spinal ferrite [9]. Because of its strong electrical and magnetic properties and wide range of uses, we will concentrate our research on this last type. Spinal ferrites are materials with good magnetic and electrical properties that are highly influenced by the distribution pattern of positive ions (cations) between the tetrahedral and octahedral sites [10]. One of the most important methods of preparing nanoferrite is the sol-gel method auto-combustion since it is simple to prepare, takes little time, and does not require high temperatures [11]. Ferrite is made from a powder that is compressed and sintered to take the desired shape. It is one of the simplest

and cheapest materials to make, and its properties are determined by a number of factors, including the shape and size of the grains, the method of preparation, the sintering temperature, the type of materials that make up ferrites, and their quantity [12]. In this study, the synthesis of Zn-Mn-Fe<sub>2</sub>O<sub>4</sub>, and Zn<sub>x</sub>Mn<sub>1-x</sub>Fe<sub>2</sub>O<sub>4</sub> /TiO<sub>2</sub> nanocomposite by Sol-Gel method at different temperatures (650, 750, and 850) °C Nano-size Mn–Zn particles were synthesized by the sol–gel combustion method. These particles were prepared from metal nitrates and citric acid. Also, the Zn-Mn-Fe<sub>2</sub>O<sub>4</sub>, and Zn<sub>x</sub>Mn<sub>1-x</sub>Fe<sub>2</sub>O<sub>4</sub>/TiO<sub>2</sub> nanocomposite were characterized by (XRD) (XRD-6000/Japan) and the results compare with the JCPDS card (Joint Committee on Powder Diffraction Standards), (FE-SEM) by "(Tescan Mira3 SEM-Czechia)" in Iran-Mashhad, (VSM), (LCR) for study structure, magnetic, and electrical properties.

## 1.2 Literature Review

The study of nanospinel ferrite has piqued the interest of researchers in recent years due to its unique properties and wide variety of applications. The following is a list of some works on the properties of nanospinel ferrites that have been studied, including structural, electrical, and magnetic properties:

In 2010 Bhalla et al., manufactured Mn-Zn soft ferrites by powder metallurgy and overall output yield of it's plant. The efforts have been made to synthesize the crucial parameters which are responsible for better material preparation, pressing and sintering. By adopting these recommendations, the rejection rate is substantially reduced and the variation in magnetic properties is less. Data which give more uniformity in bigger lots and are responsible for more uniform magnetic properties, have been discussed. Simple, quality-control instruments and their measurement methods which can be incorporated for stage inspection have been explained. The additives for better ferrite powder preparation, granules making and to obtain better magnetic have been discussed. Improved pressing, sintering, porosity, density and permeability relationship have been drawn. A sintering method to obtain better sintered density and high permeability in ferrites is also explained [13].

In 2012 Deraz and Aarifi, prepared Co<sub>1-x</sub> Zn<sub>x</sub>Fe<sub>2</sub>O<sub>4</sub> used sol-gel auto combustion to make nanocrystalline Zn-substituted cobalt ferrite powders, (x = 0, 0.25, 0.5, 0.75, and 1). The specimens had a cubic spinel structure, and the X-ray

diffraction investigation revealed that the crystallite size decreased from 70 to 51nm as the zinc content was increased to ( $x=1$ ). The lattice constant increased from (0.8370 to 0.8400 nm) with increasing the concentration of zinc to ( $x=1$ ), while the X-ray density increased from (5.293 to 5.381 g/cm<sup>3</sup>) as the concentration of zinc increased to ( $x=1$ ). The saturation magnetization of Co-Zn nanoferrites was examined using a vibrating sample magnetometer (VSM) at room temperature, and the results showed that the saturation magnetization increased as zinc substitution increased. Increased Zn concentrations resulted in a drop in coercivity ( $H_c$ ) from 807.7 to 46.0 Oe [14].

In 2011 Varshney et al., The prepared  $Zn_xMn_{1-x}Fe_2O_4$  ( $x = 0.0, 0.25, 0.50, 0.75, 1.0$ ) mixed ferrites, by chemical co-precipitation method. and studied crystal structure, average crystallite size, Raman spectra and magnetic properties, The X-ray diffraction pattern confirms that the mixed ferrite samples are in cubic inverse spinel structure. The variation of lattice parameter with increased Zn doping concentration illustrates a decreasing trend. The mixed ferrite crystallite size gradually increases with enhanced Zn doping concentration. Porosity shows decreasing trend with increased Zn doping concentration and confirms that the synthesized samples have dense random packing. The absorption band at about 500–600 cm<sup>-1</sup> in the IR spectra corresponds to the vibration of Fe<sup>2+</sup>–O<sup>2-</sup> bond related to tetrahedral (A) site without any traces of impurity (NO<sub>3</sub>) peak. [15].

In 2012 Arana et al., The Studied structural and magnetic properties after different thermal treatments, Spinel ferrites of composition  $Zn_{0.6}Mn_{0.4}Fe_2O_4$  and  $Li_{0.2}Zn_{0.2}Mn_{0.4}Fe_{2.5}O_4$  were prepared by the self-combustion sol-gel method. The samples were heat-treated in different atmospheres and temperatures, producing different effects on their morphological and structural properties. The resulting products of each treatment were structurally and magnetically characterized. Incorporating Li to the crystalline lattice increases saturation magnetization and promotes a decrease in secondary phases segregation. This result is explained assuming that Li incorporation produces a cationic redistribution in the spinel structure [16].

In 2013 M. Zhang et al., The Studied and prepared  $Ni_{1.5}Zn_{0.5}Fe_2O_4$  by the sol-gel method to (9) specimens of the chemical. After completing an X-ray diffraction investigation, it was discovered that all specimens of the produced ferrite

compound formed the spinel phase, with average crystallite sizes ranging from 9 to 96 nm, if the average crystallite size increasing with the increase in the annealing temperature. When the annealing temperature is raised, the lattice constant decreases. The results of the magnetic measurements performed on the specimens of the synthesized chemical revealed that all of the specimens were paramagnetic. It was also discovered that when particle size rises, saturation magnetization increases, which can be explained by action redistribution on tetrahedral A and octahedral B sites, as well as domain wall motion [17].

In 2014 Veverka et al., The prepared  $\text{Co}_{0.4}\text{Zn}_{0.6}\text{Fe}_2\text{O}_4$  by the co-precipitation method to make magnetic cores of two different sizes, which were annealed at temperatures of 500 °C and 650 °C. The nanoparticles were encapsulated in silica, which resulted in colloid ally stable water suspensions. The increase of annealing temperatures had caused a significant rise in Curie temperatures ( $T_c$ ) and blocking temperature ( $T_B$ ), additionally the heating efficiency of sample had been enhanced [18].

In 2014 Rajendra et al., The studied the structural and electric properties of Titanium Substituted Ni-Cu-Zn Ferrite by solid state reaction. In work, the impact of  $\text{Ti}^{4+}$  substituted  $\text{Ti}_x(\text{Ni}_{0.35}\text{Cu}_{0.05}\text{Zn}_{0.60}\text{Fe}_{1.98}\text{O}_{4+\delta})_{1-x}$  ferrite is investigated by varying the concentration of the  $\text{Ti}^{4+}$  with  $x = 0.003, 0.0765, 0.15$ . The compound is synthesized by solid state method. Structural and electrical properties have been explored using XRD, FTIR, and dielectric spectroscopy technique. X-ray diffraction (XRD) patterns reveal the formation of the cubic spinel phase in the samples after sintering the compound at 10000C The mean crystallite size DXRD of the samples determined from XRD line broadening is 35.18–44.68 nm. The dielectric constant vary as a function of frequency and composition at room temperature. It is observed that with the increase in the concentration of  $\text{Ti}^{4+}$  ions dielectric constant increases [19].

In 2015 Joseyphus et al., The studied and prepared  $\text{Mn}_{0.67}\text{Zn}_{0.33}\text{Fe}_2\text{O}_4$  nanoparticles with size ranging from 20 to 80 nm using the modified oxidation method. The Curie temperatures for all the samples are found to be within  $630 \pm 5$  K suggesting that there is no size-dependent cation distribution. The critical particle size limit for super paramagnetism is found to be 25 nm at 293 K. The

modified oxidation method can be used to synthesise ferrite nanoparticles of the required size range with specific magnetic properties suitable for applications [20].

In 2016, C. Stergiou, The studied microstructure and electromagnetic properties of Ni-Zn-Co Ferrite up to 20 GHz, The present paper examines the relation between different developed microstructures and the microwave electromagnetic properties in Ni-Zn-Co ferrite. To this end, the  $\text{Ni}_{0.25}\text{Zn}_{0.25}\text{Co}_{0.5}\text{Fe}_2\text{O}_4$  composition has been prepared with the conventional ceramic process with varied pre-firing  $T_P$  (750°C, 1000°C) and sintering  $T_S$  top temperatures (1200 °C, 1250 °C). When lower temperatures are applied in these production stages, incomplete microstructures with low density, higher porosity, or finer grains are achieved. On account of these features, the contributions of domain wall motion and spin rotation to the complex permeability  $\mu^*$  move to higher frequencies, whereas microwave dielectric permittivity  $\varepsilon^*$  is decreased. In particular in conjunction with the high Co content, the wall relaxation and spin resonance are interestingly forced to occur at 850 MHz and 8.05 GHz, respectively. [21].

In 2016 Singh et al., The studied and prepared  $\text{Mg}_x\text{Zn}_{1-x}\text{Fe}_2\text{O}_4$  ( $x=0.5, 0.6, 0.7$ ) by co-precipitation technique and then subsequently heated to 800 °C in order to investigate structural, thermal and magnetic properties. The samples are characterized by using XRD, FTIR, TGA-DSC, SQUID and Mössbauer spectroscopy techniques. The synergic effect of heat treatment with substitution of  $\text{Mg}^{2+}$ , results in random variation of lattice parameter ( $a$ ) and crystallite size ( $D$ ). FTIR studies revealed the formation of cubic spinel structure. The broadening at octahedral bands for compositions  $x=0.6$  and  $0.7$  attributes to distribution of ferrite particles of different sizes in these samples. The characteristic feature of hysteresis loops reflects the nature of ferrite particles in the state of super para magnetism. The saturation magnetization at room temperature has been reported for composition  $x=0.7$  is 44.03 emu/g. [22].

In 2017 Angadi et al., The studied and prepared  $\text{Mn}_{0.5}\text{Zn}_{0.5}\text{Sc}_y\text{Fe}_{2-y}\text{O}_4$  ( $y=0.00, 0.01, 0.03$  and  $0.05$ ) nanoparticles by solution combustion method using mixture of fuels were reported for the first time. The mixture of fuels plays an important role in obtaining nano crystalline, single phase present without any heat treatment. X-ray diffraction (XRD) results confirm the formation of the single-phase ferrites which crystallize in cubic spinel structure. The Fourier transform infrared spectra

(FTIR) exhibit two prominent bands around  $360\text{ cm}^{-1}$  and  $540\text{ cm}^{-1}$  which are characteristic feature of spinel ferrite. The transmission electron microscope (TEM) micrographs revealed the nanoparticles to be nearly spherical in shape and of fairly uniform size. The room temperature impedance spectra (IS) and vibrating sample magnetometry (VSM) measurements were carried out in order to study the effect of doping ( $\text{Sc}^{3+}$ ) on the characteristic properties of Mn-Zn ferrites. Further, the frequency dependent dielectric constant and dielectric loss were found to decrease with increasing multiple  $\text{Sc}^{3+}$  concentration. Magnetic measurements reveals that saturation magnetization ( $M_s$ ), remnant magnetization ( $M_r$ ), magnetic moment ( $\eta_B$ ) and magnetic particle size ( $D_m$ ) increase with  $\text{Sc}^{3+}$  ion concentration up to  $x=0.03$  and then decrease. The values of spin canting angle ( $\alpha_{Y-K}$ ) and the magnetic particle size ( $D_m$ ) are found to be in the range of  $68\text{--}75^\circ$  and  $10\text{--}19\text{ nm}$  respectively with  $\text{Sc}^{3+}$  concentration. [23].

In 2019 Petrescu et. al, The studied the morphological, structural, and chemical composition of the  $\text{Mn}_x\text{Zn}_{(1-x)}\text{Fe}_2\text{O}_4$  ferrites are produced by using a mixture of finely-powdered nitrogen-based salt precursors pressed into a mold, and subsequently sintering the resulting powder. The bulk samples are cut into smaller prismatic shapes (rectangular prisms) of various volumes, by using a diamond coated steel wire. The magnetic characterization of the MnZn type ferrite provides one with valuable information, as the open sample results have been corrected with demagnetization factors, which consider the punctual susceptibility of the material. The novelty of this work consists of the estimation of these factors by an iterative procedure, i.e., by using an exponential fitting procedure. The corrected values are presented and discussed and fit manufacturers' data, which are provided as a range of values. The last part of the study focuses on estimating the magnetic losses in high frequencies for this ferrite by using the Steinmetz approach, i.e., the hysteresis losses are determined for the MnZn ferrite. All these properties make MnZn-type ferrites ideal for applications in a variety of high frequency transformers, adjustable inductors, wide band transformers, and high frequency circuits from  $10\text{ kHz}$  to  $50\text{ MHz}$  [24].

In 2020 Vahdati and Sedghi, studied the properties of zinc-manganese nanoferrite to compare organic fuels that were produced in conditions created by the auto gel combustion method, using citric acid, glycine, and urea with different pH. The samples were prepared in stoichiometric ratios to gain  $\text{Mn}_{0.5}\text{Zn}_{0.5}\text{Fe}_2\text{O}_4$ ,

and all the samples were calcined in the same condition (500 °C and 30 minutes). It should be noted that the entire process of synthesis was photographed to analyze the effect of fuels during the combustion process. Combustion reactions were studied by simultaneous thermal analysis (STA), FT-IR spectroscopy, and X-ray diffraction (XRD), also the rietveld method was used to determine the type and amount of crystalline phases. Magnetic properties of the samples were measured by vibration sample magnetometer (VSM), and their morphology and powder agglomeration was observed by field emission scanning electron microscopy (FE-SEM) and transmission electron microscopy (TEM). Superior magnetic properties of the sample synthesized with glycine were achieved. Urea gave the smallest particle size, while citric acid produced intermediate properties [25].

In 2021 Jahan et al., In the study,  $\text{Al}^{3+}$  substituted Ni–Zn–Co nanocompositions were successfully synthesized through the sol–gel technique. Rietveld refinement X-ray diffraction data evidenced the formation of the nanospinel structure with phase group  $\text{Fd}3\text{m}$  for all of the compositions. The cation distributions were established through the Rietveld refinement technique. Average particle sizes were in the regime of 25–29 nm, as demonstrated by TEM examinations. Thin areas of Al–O–Al structures were formed around the grain boundaries that hindered particle growth. The vibrational modes' characteristic peaks are red-shifted and blue-shifted, as exhibited in the samples' Raman spectra. Enhanced  $M_s$  with low values of  $H_c$  and  $M_r$  was found for the compositions. Magnetic outcomes revealed that the prepared nanocompositions are soft ferromagnetic materials and suitable for numerous technological applications. Frequency-dependent dielectric constants and ac resistivity indicated that the ferrites were highly resistive. Introducing  $\text{Al}^{3+}$  in Ni–Zn–Co ferrites makes the nanosamples highly resistive while maintaining the high magnetizations 86.39 emu/g for the  $x = 0.12$  compositions. [26].

In 2021 Akhter et. al, prepared and studied  $\text{Cu}_{1-x}\text{Zn}_x\text{Fe}_2\text{O}_4$  (where  $x = 0.0$ – $1.0$  with step of 0.1) ferrites by double sintering solid state reaction method to explore disorder magnetic behavior. The room temperature (300 K) and low temperature (5 K) magnetic behavior has been analyzed using M-H curve, B–H loop,  $\mu$ i-T curve and M-T curve. The saturation magnetization for sample  $x = 0.0$  to 0.6 and non-saturation magnetization for sample  $x = 0.7$  to 1.0 designate the existence of long-range and short-range ferromagnetic order respectively. The Curie temperature has

been derived from the sharp fall of permeability for sample  $x = 0.0-0.6$  which is declining with raising Zn content due to redistribution of cations and weakening of A-B exchange interaction. The shrinking of coercivity affirms softer nature which can be used as high frequency soft magnetic materials. For M-T curve, when temperature is lowered from 300 K to 5 K, different disorder magnetic transition such as paramagnetic-ferromagnetic-reentrant spin glass-spin glass has been remarked for sample  $x > 0.6$ . All these feature of magnetic behavior of Cu-Zn ferrites has been studied in details in this paper [27].

### 1.3 Aim of the Study

- 1- Synthesis of  $Zn_xMn_{1-x}Fe_2O_4$  nanoferrites by a sol-gel auto-combustion method and  $Zn_xMn_{1-x}Fe_2O_4/TiO_2$  by the conventional ceramic method.
- 2- Studying the effect of increasing the content ( $x$ ) and calcination, temperature of  $Zn_xMn_{1-x}Fe_2O_4$ , and studying the influence of ( $TiO_2$ ) concentration on the structural, magnetic, and dielectric properties (XRD, FT-IR, FE-SEM and EDS).
- 3- Testing the magnetic parameters such as (saturation magnetization ( $M_s$ ), remanence magnetization ( $M_r$ ), and coercivity ( $H_c$ )) of synthesized ferrite nanoparticles in applied field  $\pm 15$  kOe through vibrating sample magnetometer (VSM) at room temperature.
- 4- Measurements of the electrical properties (dielectric constant ( $\epsilon'$ ), dielectric loss angle ( $\tan \delta$ ), dielectric loss factor ( $\epsilon''$ ), and ac conductivity ( $\sigma_{ac}$ )) of synthesized nanoferrite with the frequency from (50 Hz) to (2MHz) by using LCR meter at room temperature.
- 5- Magnetically flexible ferrites are used in cores for transformer windings, electric motors, and transceiver antennas, In HF technology, in the construction of antennas and in parts for moderators, In headphones for electronic recording equipment, video equipment, and hard disks, and Stealth and camouflage technology (ferrites absorb radar waves).



---

# Chapter Two

---

Theoretical part





## (2-1) Introduction

The need for modern technology at a faster rate than ever before with the development of society. As a result, information technology, which has grown at an exponential rate over the last half-century, is one of the cornerstones of this advancement. In recent years, the demand for smaller transistors and other important components has shifted emphasis to various approaches to boost computer performance without drastically reducing structural dimensions. One solution to this problem has been to use multi-ferric instead of single-ferric materials in the process. Multi-ferric materials contain two or more of the major ferric orders, Nano-sized due to a special property known as super-paramagnetic, magnetic materials have unique magnetic properties. Magnetic nanoparticles are important for biological applications because of their small size in comparison to biological entities, as well as their unique magnetic properties. Magnetic nanoparticles have been used in a variety of biological applications, including MRI, hyperthermia treatment, medication delivery, tissue engineering, and bioanalysis [28-29].

## (2.2) Origin of Magnetism

A magnetic field is a force field similar to gravitational and electrical fields that is surrounding a source of potential; there is a contoured sphere of influence or field. The origin of the magnetic potential is known as magnetic dipoles. Magnetism basically results from two electronic motions accompanying with the atom; the orbital motion of the electron and the spin motion of the electron. For macroscopic purposes these small currents due to these motions can be consider as magnetic dipoles, as a rule they cancel each other out due to the random orientation of the atoms. But when a magnetic field is applied, a net alignment of these magnetic dipoles implement and the medium becomes magnetically polarized [30,31] Magnetic field H (Amperes per meter) is the intensity of the magnetic field that magnetizes the substance; B is the magnetic field. The magnetic flux density inside a magnetized substance that is subjected to a H field is called induction. B is measured in teslas (or webers per square meter). The strength of the magnetic field and the flux density are proportional to:

$$B = \mu H \quad \dots\dots\dots \quad \dots\dots\dots \quad \dots\dots\dots \quad (2.1)$$

The permeability parameter is a property of the specific medium through which the H field passes and in which B is measured. Webers per ampere-meter (Wb/A-m) or henries per meter (H/m) are the units of permeability [30]. Magnetization M is the total of the magnetic moments  $m_j$  per unit volume and is used to calculate the magnetic moment per unit volume of the magnetized material. [30].

$$M = \sum_{\text{volume}} m_j \dots\dots\dots (2.2)$$

The magnitude and sign of M, as well as the way M fluctuates with H, are used to explain the magnetic properties of magnetic materials. Magnetic susceptibility is the ratio of these two quantities. [30].

$$\chi = \frac{M}{H} \dots\dots\dots (2.3)$$

The magnetization M of a material is expressed by the relation:

$$\mu = \mu_0 (1 + \chi) \dots\dots\dots (2.4)$$

The value of  $\mu$  and  $\mu_r$  characterizes the magnetic properties of a material [30].

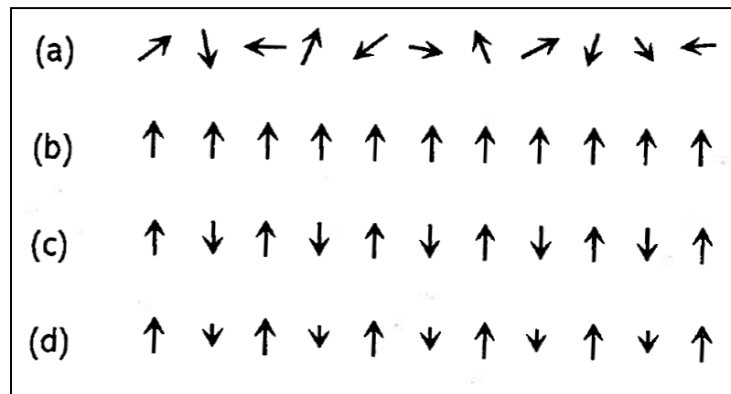
$$B = \mu_0 (H + M) = \mu_r \mu_0 H = \mu H \dots\dots\dots (2.5)$$

Where  $\mu_0 = 4\pi \times 10^{-7} \text{ Hm}^{-1}$  is the permeability of free space and B and H are measured in Tesla (T) and  $\text{Am}^{-1}$  respectively.  $\mu_r$  is termed as the relative permeability of the material, subsequently from the relations (2.3) and (2.4) [31].

### (2.3) Magnetic properties

Ferromagnetism is defined as the presence of a spontaneous magnetization that can be reversed by an opposing magnetic field, similar to how electric polarization may be reversed by an electric field. A diamagnetic response to an applied magnetic field exists in all materials in nature [32]. Other magnetic phenomena generated by unpaired electrons can be found in some inorganic materials. Typically found on metal cations. Figure (2-1) [33] depicts the various effects for a hypothetical 1D crystal. Paramagnetic (a) is a magnetic polarization state with a positive magnetic susceptibility that is arbitrarily oriented, The material is attracted to the magnetic field, which means it is in a state of attraction. In contrast to ferromagnetism (b), where the induced magnetic

moment is preserved in the absence of an externally applied magnetic field, thermal motion causes the spins to become randomly orientated, lowering total magnetization to zero when the field is removed. Because neighboring spins point in opposing directions in antiferromagnetism (c), the overall magnetic moment is zero, whereas ferrimagnetism (d) arises when neighboring spins point in opposite directions but are of unequal size,



**Figure(2-1) Schematic magnetic phenomena in a 1D crystal: (a) paramagnetic; (b)ferromagnetism; (c) antiferromagnetism; (d) ferrimagnetism [33].**

## (2.4) Types of Magnetic Materials

The magnetic forces of a material's electrons will be changed when it is placed in a magnetic field. Faraday's Law of Magnetic Induction describes this phenomenon. Materials, on the other hand, can respond to an external magnetic field in a variety of ways. The atomic and molecular structure of the material, as well as the net magnetic field associated with the atoms, all influence this reaction. The electron orbital motion, the change in orbital motion generated by an external magnetic field, and the spin motion of the electron are all magnetic moments associated with atoms. Some materials develop a magnetization that is parallel to  $B$  (paramagnets), whereas others acquire a magnetization that is opposed to  $B$  (antimagnets) (Diamagnetism) [34]. Electrons are found in pairs in most atoms. A pair of electrons spins in opposing directions. When electrons are coupled together, their magnetic fields cancel each other out due to their opposing spins. As a result, there is no net magnetic field.

Materials having some unpaired electrons, on the other hand, will have a net magnetic field and react more to an external field.

The periodic table is color-coded to show magnetic material classes. The legend indicates: Ferromagnetic (light blue), Paramagnetic (white), Antiferromagnetic (pink), and Diamagnetic (green). The following table summarizes the classification of elements based on the image:

Element	Magnetic Class
H	Diamagnetic
He	Diamagnetic
Li	Paramagnetic
Be	Diamagnetic
Na	Paramagnetic
Mg	Diamagnetic
Al	Paramagnetic
Si	Diamagnetic
P	Diamagnetic
S	Diamagnetic
Cl	Diamagnetic
Ar	Diamagnetic
K	Paramagnetic
Ca	Diamagnetic
Sc	Paramagnetic
Ti	Paramagnetic
V	Paramagnetic
Cr	Antiferromagnetic
Mn	Paramagnetic
Fe	Ferromagnetic
Co	Ferromagnetic
Ni	Ferromagnetic
Cu	Diamagnetic
Zn	Diamagnetic
Ga	Diamagnetic
Ge	Diamagnetic
As	Diamagnetic
Se	Diamagnetic
Br	Diamagnetic
Kr	Diamagnetic
Rb	Paramagnetic
Sr	Diamagnetic
Y	Paramagnetic
Zr	Paramagnetic
Nb	Paramagnetic
Mo	Paramagnetic
Tc	Paramagnetic
Ru	Paramagnetic
Rh	Paramagnetic
Pd	Paramagnetic
Ag	Diamagnetic
Cd	Diamagnetic
In	Diamagnetic
Sn	Diamagnetic
Sb	Diamagnetic
Te	Diamagnetic
I	Diamagnetic
Xe	Diamagnetic
Cs	Paramagnetic
Ba	Diamagnetic
La	Paramagnetic
Hf	Paramagnetic
Ta	Paramagnetic
W	Paramagnetic
Re	Paramagnetic
Os	Paramagnetic
Ir	Paramagnetic
Pt	Paramagnetic
Au	Diamagnetic
Hg	Diamagnetic
Tl	Diamagnetic
Pb	Diamagnetic
Bi	Diamagnetic
Po	Diamagnetic
At	Diamagnetic
R	Diamagnetic
Fr	Paramagnetic
Ra	Diamagnetic
Ac	Paramagnetic
Ce	Paramagnetic
Pr	Paramagnetic
Nd	Paramagnetic
Pm	Paramagnetic
Sm	Paramagnetic
Eu	Paramagnetic
Gd	Paramagnetic
Tb	Paramagnetic
Dy	Paramagnetic
Ho	Paramagnetic
Er	Paramagnetic
Tm	Paramagnetic
Yb	Paramagnetic
Lu	Paramagnetic

Figure (2.2): Periodic table showing different kinds of magnetic materials [34].

As indicated in table 2.1, the most prevalent magnetic material classes are diamagnetism, paramagnetic, ferromagnetism, antiferromagnetism, and ferrimagnetism [35]

Table (2.1): Types of Magnetism [36].

Type of Magnetism	Susceptibility	Example
Diamagnetism	Small & negative	Au, Cu
Paramagnetic	Small & positive	Pt, Mn
Ferromagnetism	Large & positive, function of applied field, microstructure dependent	Fe, Co
Antiferromagnetism	Small & positive	Cr, MnO
Ferrimagnetism	Large & positive, function of applied field, microstructure dependent	BaFe <sub>12</sub> O <sub>19</sub> , Fe <sub>3</sub> O <sub>4</sub>

### (2.4.1) Diamagnetism

Diamagnetism, or a weak, negative magnetic susceptibility, is present to some amount in all materials. A magnetic field produces a magnetic moment in a diamagnetic material that opposes the magnetic field that creates it [37]. When there is no applied field, the atoms of a diamagnetic

material have no magnetic moment. Under the influence of an applied field ( $H$ ), electrons spin, producing a magnetization ( $M$ ) in the opposite direction of the applied field. The diamagnetism effect is present in all materials, although it is usually eclipsed by the larger paramagnetic or ferromagnetic terms. Temperature has no effect on the value of susceptibility. In September 1845, Michael Faraday discovered and termed diamagnetism [36].

Figures (2.3) (a) and (b) show how diamagnetism works. The atoms have zero magnetic moment in the absence of an external magnetic field, as seen in Fig (2.8a).

When an external magnetic field  $H_0$  is applied in the direction depicted in Figure (2.3) (b), however, the atoms acquire an induced magnetic moment in the opposite direction as the field.

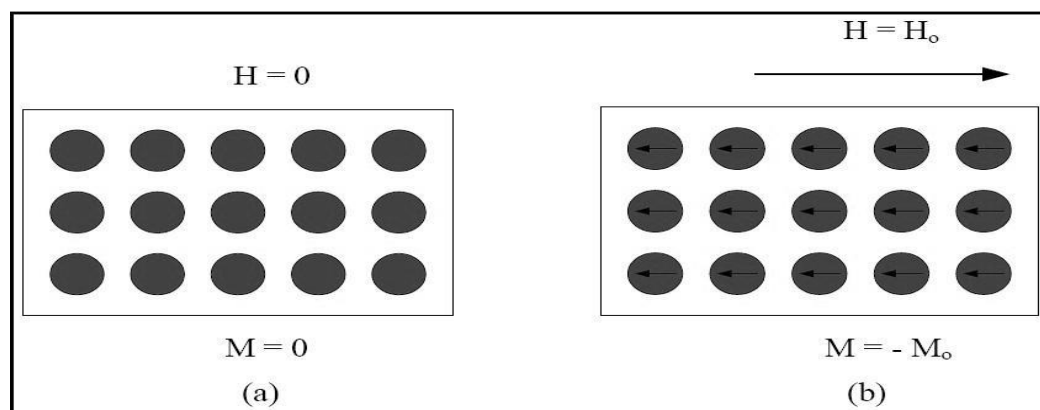


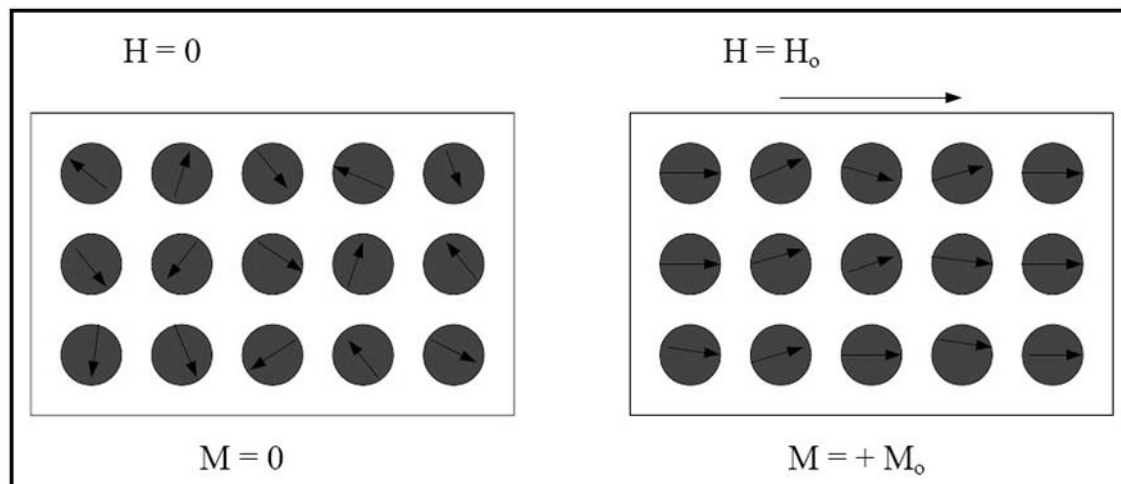
**Figure (2.3): (a) Diamagnetic material: When  $H=0$ , the atoms have no magnetic moment, hence  $M=0$ . (b) When a magnetic field  $H_0$  is applied to the atoms, the atoms acquire an induced magnetic moment in the opposite direction of the applied field, resulting in negative susceptibility [35].**

### (2.4.2) Paramagnetic materials

Atoms, molecules, and matter ions with unsaturated exterior orbits produce magnetic barrages, which act as a form of guidance, and so have a persistent magnetic impulse caused by the directed aggregation of the electron's spinel. The intensity of the external magnetic field and the temperature affect the direction of magnetism in magnetic materials. This behavior depicts the material at the Curie Temperature's greatest temperatures ( $T_c$ ). Is the temperature degree at which the energy of thermal irritation triumphs over the quantum interaction forces that guide

and filter magnetic moments between the atoms of the material, and the Korean degree varies from one substance to the next. When the baramagnetic materials' total gamma is not zero, and their magnetic susceptibility is positive and smaller than one lot ( $\chi \ll 1$ ), However, its effectiveness is larger than one, and this behavior vanishes when the field vanishes. Chlorides, sulfates, chromium carbonate, iron, cobalt, salts, and trace elements like deserosium are all examples of these elements [39,38].

The material's net magnetic moment and magnetization both reach zero. When an external magnetic field is introduced, however, the individual atomic magnetic moments tend to align themselves in the direction of the external magnetic field, resulting in a nonzero weak magnetization, as illustrated in figures (2.4) (a) and (b). These materials are paramagnetic, and the phenomena is referred to as paramagnetism [40].



**Figur (2.4):** Each atom in a paramagnetic substance has a permanent magnetic moment. All magnetic moments are randomly orientated when  $H=0$ , hence  $M=0$ . (b) When a magnetic field of  $H_0$  is applied, the atomic magnetic moments prefer to align themselves with the field's direction. As a result, the [35] has a net magnetization  $M=M_0$  and a positive susceptibility.

### (2.4.3) Ferromagnetic materials

The interactions between atomic magnetic moments of identical size in ferromagnetic materials align them in a common direction, resulting in a significant net magnetization even in the absence of a magnetic field [41, 42]. Ferromagnetism in Fe, Co, and Ni (magnetic susceptibilities nearing  $10^{+6}$ ) is owing mostly to the self-alignment of groups of atoms bearing permanent magnetic moments in the same direction. As a result,

they have a significant and positive magnetic susceptibility to an external field, demonstrating a strong attraction to magnetic fields while retaining their magnetic characteristics after the external field has been removed [43]. When ferromagnetic materials are heated, the thermal agitation of the atoms results in a drop in the alignment degree of the atomic magnetic moments, and hence a decrease in saturation magnetization. Eventually, the material becomes paramagnetic due to the high thermal agitation. In the case of a ferromagnetic substance, Only below a particular temperature ( $\theta_f$ ) known as the ferromagnetic Curie temperature may spontaneous magnetization occur. Such materials act like paramagnetic materials far above the Curie temperature and have a well-defined susceptibility as specified by the Curie-Weiss equation [44].

$$\chi = \frac{C}{(T - \theta_f)} \quad (2.2)$$

A ferromagnetic material becomes paramagnetic above the transition temperature because the parallel spin alignment energy is inadequate to counteract the randomizing effect, which causes the spin direction to rotate [45]. Furthermore, even in the absence of an external field, coupling interactions lead neighboring atoms' net spin magnetic moments to align with one another in a ferromagnetic material (Figure 2.5)

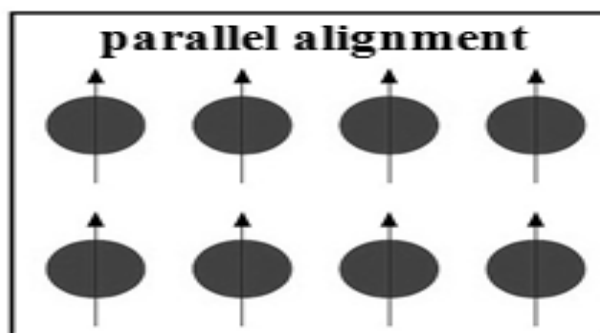


Figure (2.5): Ferromagnetism [35].

#### (2.4.4.) Antiferromagnetism

Magnetic moment coupling between nearby atoms or ions causes anti-parallel alignment of magnetic dipoles in several other types of materials. Antiferromagnetism is defined as the alignment of spin moments of nearby atoms or ions in exactly opposite orientations [46,47]. At all temperatures, they exhibit a weak positive magnetic susceptibility on the order of paramagnetic material, but their susceptibilities fluctuate

in an unusual way. MnO, NiO, and CoO are examples of antiferromagnetic materials [48].

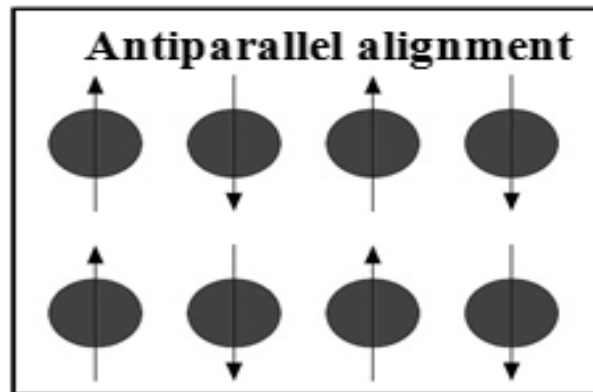


Figure (2.6): Antiferromagnetism [35].

### (2.4.5) Ferrimagnetism

Ferrimagnetic materials have spin structure of both spin-up and spin-down components but have a net non-zero magnetic moment in one of these directions [49]. In antiferromagnetism, the magnetic moments of atoms on neighboring sub lattices are opposite each other; nevertheless, in ferrimagnetic materials, the opposing values are uneven (Fig. 2.7). This magnetic moment might potentially be attributable to more than two sub lattices, as well as triangular or spiral sub lattice structures [50]. Only compounds with more complicated crystal structures than pure elements exhibit ferrimagnetism. Ferrimagnetism is only found in compounds with more complex crystal structures than pure elements. Magnetic susceptibility is identical in magnitude for ferromagnetic and ferrimagnetic materials, but the alignment of magnetic dipole moments is vastly different.

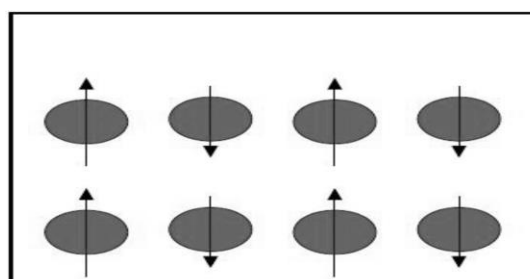


Figure (2.7): Ferrimagnetism [51].

## (2.5) Titanium Dioxide

Titanium dioxide is one of the most common minerals on the Earth's crust and ranks ninth in the list of abundant minerals. It is a lustrous, silver-colored transition metal, obtained primarily from the ore of limonite which constitutes the world's most widely distributed.

Titanium dioxide is an inorganic chemical compound with the formula  $\text{TiO}_2$ , composed of titanium cation and the sulfate anion. Titanium dioxide is a sulphate salt of titanium and is found abundantly as mineral rutile; here the titanium is attached to four oxygen atoms. It is an alkaline, divalent metal, which is used in a wide range of medical use due to its non-toxic nature [52].

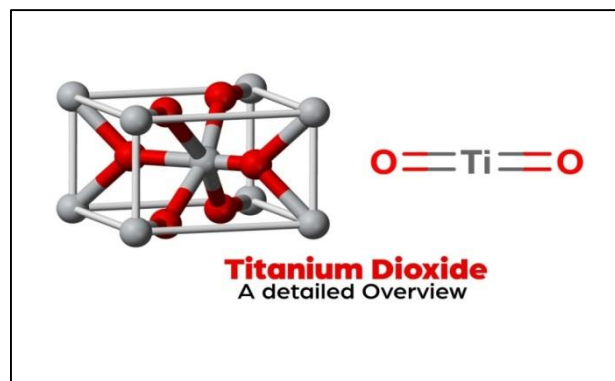


Figure (2.8): The structure of titanium dioxide [52].

## (2.6) Ferrite Materials

Ferrites are a wide family of metal oxides with exceptional magnetic characteristics. It is a common type of ceramic ferrimagnetic material with a modified iron structure, which has been investigated and applied in various fields during the last 50 years [53,54]. Ferrites are dark brown or grey in appearance and very hard and brittle in physical character. The super-exchange interaction between metal ions and oxygen ions causes ferrimagnetism in ferrite. The opposite electron spins in ferrite cause a decrease in magnetism when compared to ferromagnetic metals with parallel spins. Ferrites have moderate resistivity, good electrical qualities with low eddy current losses and low dielectric and magnetic losses [55,56]. Ferrites have three different structures: spinel, garnet and hexagonal ferrite are determined by the size and charge of the metal ions that balance the charge of the oxygen ions, and their relative amounts [57].

### (2.6.1) Spinel Ferrite

The spinel ferrite structure was found separately by Bragg [60] and Nishikawa [58] in 1915. Spinel ferrites have the formula  $M\text{-Fe}_2\text{O}_3$ , where M is a divalent metal ion like  $\text{Mn}^{2+}$ ,  $\text{Ni}^{2+}$ ,  $\text{Fe}^{2+}$ ,  $\text{Co}^{2+}$ ,  $\text{Zn}^{2+}$ ,  $\text{Cu}^{2+}$ . The spinel lattice is made up of a tightly packed oxygen arrangement in which the unit cell is made up of 32 oxygen ions. Face-centered cubic (FCC) configuration is used to pack these anions. There are two sorts of gaps between anions: tetrahedral coordinated sites (A), which are surrounded by four oxygen atoms, and octahedral coordinated sites (B), which are surrounded by eight oxygen atoms (B), which are encircled by six oxygen atoms from their nearest neighbors. There are 32 oxygen ions in the unit cell, 64 tetrahedral sites, and 32 octahedral sites. Metal ions occupy just 8 tetrahedral and 16 octahedral sites, resulting in a structure that is electrically unbiased. Spinel ferrites have a ferrimagnetic ordering magnetically. The magnetic moments of the cations at the A and B-sites are aligned parallel to one another. Because there are twice as many B-sites as A-sites, the crystal has a net moment of spins yielding, resulting in the ferrimagnetic order. The metal cation utilized, as well as the ion distribution between sites A and B, exhibit a magnetic system that can be adjusted [59]. Normal, inverse, and random spinel ferrites are the three types of spinel ferrites based on their cation distribution. The structure of spinel ferrite (Figure 2-9) may be described as a cubic arrangement of densely packed oxygen atoms.

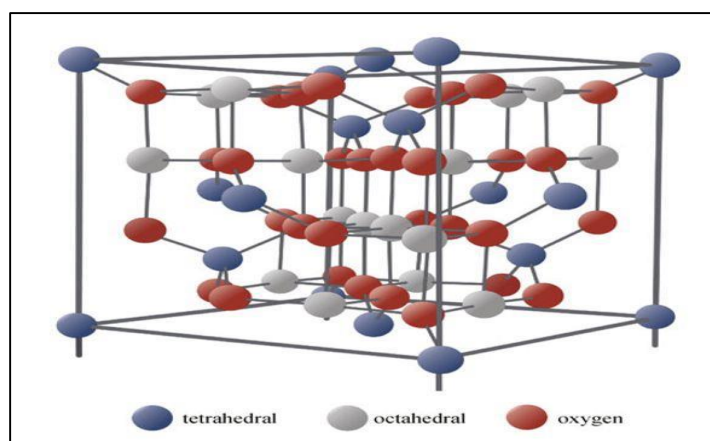


Figure (2.9): Schematic representation of spinel structure [60].

### (2.6.1.1) Normal spinel

The divalent ions are all on A sites in typical spinel, whereas the trivalent ions are on B sites. Metal ions occupy eight tetrahedral and sixteen octahedral positions in the spinel structure's fundamental unit cell. [61].

### (2.6.1.2) Inverse spinel

All  $\text{Me}^{2+}$  ions reside in B-sites in inversed spinel structure, and  $\text{Fe}^{3+}$  ions are evenly distributed across A and B-sites: structural formula of these ferrites is  $\text{Me}^{2+}[\text{Fe}_2^{3+}]\text{O}_4^{2-}$ . The spinel structure of magnetite  $\text{Fe}_3\text{O}_4$  and  $\text{NiFe}_2\text{O}_4$  ferrites is inversed [62, 63].

### (2.6.1.3) Random (mixed) spinel

The cations  $\text{Me}^{2+}$  and  $\text{Fe}^{3+}$  occupy both A and B-sites in mixed spinel structure; the structural formula of this ferrite is  $\text{Me}_{1-\delta}^{2+}\text{Fe}_\delta^{3+}[\text{Me}_\delta^{2+}\text{Fe}_{2-\delta}^{3+}]\text{O}_4^{2-}$ , where  $\delta$  is the degree of inversion. This sort of structure is represented by  $\text{MnFe}_2\text{O}_4$ , which has an inversion degree of  $\delta=0.2$  and a structural formula of  $\text{Mn}_{0.8}^{2+}\text{Fe}_{0.2}^{3+}[\text{Mn}_{0.2}^{2+}\text{Fe}_{1.8}^{3+}]\text{O}_4^{2-}$ . Mn–Zn ferrites also exhibit a mixed spinel structure ( $\text{Zn}^{2+}$  favours A-sites)  $\text{Zn}_x^{2+}\text{Mn}_y^{2+}\text{Fe}_{1-x-y}^{3+}[\text{Mn}_{1-x-y}^{2+}\text{Fe}_{1+x+y}^{3+}]\text{O}_4^{2-}$ , where  $\delta=1-x-y$  [64, 65].

### (2.6.2) Garnet Ferrite

Garnets are a form of ferrimagnetic material utilized in a variety of high-frequency applications. Whereas, yttrium iron garnet ( $\text{Y}_3\text{Fe}_5\text{O}_{12}$ ) is an iron garnet known for its technical value in a variety of applications, including phase shifters and lasers. The electromagnetic, mechanical, thermal, and magneto-optical characteristics of garnet ferrites ( $\text{A}_3\text{B}_5\text{O}_{12}$ ) are fascinating and unusual [66]. There are three sorts of sites in this structure: (a), (b), and (c) It was discovered that  $24\text{Fe}^{3+}$  ions occupy tetrahedral sites,  $16\text{Fe}^{3+}$  ions occupy octahedral sites, and  $24\text{R}^{3+}$  ions occupy dodecahedral sites, whilst oxygen ions are distributed to interstitial sites [67].

### (2.6.3) Hexagonal Ferrite

Hexagonal ferrites are commonly employed as permanent magnets and are known for their strong coercivity [68]. Based on the chemical formula and crystal structure, hexagonal ferrites are divided into six categories.  $MO \cdot 6Fe_2O_3$  is their general formula, where M might be Ba, Sr, or Pb. Barium ferrite,  $BaO6Fe_2O_3$ , is the most significant hexagonal ferrite. The hexagonal magneto-plumbite structure of barium ferrite has ten oxygen layers in its fundamental unit cell and is made up of four building blocks. Permanent magnets made on hexagonal ferrites are frequently employed. The hexagonal ferrite lattice is comparable to the spinel structure and is magnetically hard because to the tight packing of oxygen ions (unlike the cubic ferrites which are magnetically soft), They, like cubic ferrites, are inexpensive to make using ceramic manufacturing processes and may be powdered and shaped into any shape necessary.

### (2.7) Characterization of Mn-Zn-Ferrite

The current state of biophysics verifies the necessity for magnetic nanoparticles to treat malignant tumors so that thermal ablation may be performed without causing harm to normal cells.  $MnZnFe_2O_4$ 's Curie temperature may be regulated by modifying the zinc concentration in the structure, making it ideal for thermal treatments [69]. The Curie temperature in  $Mn_{1-x}Zn_x Fe_2O_4$  nanoparticles is controlled by changes in zinc concentration. It was discovered that increasing the zinc concentration for  $x = 0.5, 0.6, 0.8,$  and  $1$  decreased the Curie temperature from  $320K$  to  $240K$  for  $x=1$  [70]. As a result, heat dispersion in hyperthermia therapy may be controlled [71].

### (2.8) Magnetic materials types.

Soft and hard magnetic materials are the two types of magnetic materials. Hard magnetic materials are those that are difficult to magnetize and demagnetize, whereas soft magnetic materials are those that are readily magnetized and demagnetized. Because high coercivity resists the magnetization action, hard magnetic materials have a high coercivity. The hysteresis loop was used to describe the fundamental difference between two types of permanent magnets. The hysteresis loop in soft magnetic materials is small, but the hysteresis loop in hard

magnetic materials is large. Magnetization follows the fluctuation of the applied field without considerable loss in the tiny hysteresis loop. The magnetic energy that may be stored in materials is shown by the large hysteresis loop [72].

### **(2.8.1) Soft magnetic materials**

Magnetization and demagnetization of soft magnetic materials is simple. Soft magnetic materials have a low coercive field and a high magnetization, making them useful in a variety of applications. The magnetization virtually follows the applied field disparition without hysteresis loss because they have a tight hysteresis loop (Figure 2.9-b). Inductors, transformer cores, microwave devices, recording heads, and medical equipment, for example, employ Ni, Fe, Mn, Co, and other metals [73]. Soft ferrites have a cubic structure and magnetic features such as saturation, megahertz resonance frequency, superior oxidation resistance, low coercivity, and high magnetic permeability. Soft ferrites are superior to all other magnetic materials because of these benefits [74].

### **(2.8.2) Hard magnetic materials**

Permanent magnets, often known as hard magnetic materials, are used to generate a strong field without using a coil. Permanent magnets must have a high coercivity, which means they must have a strong net magnetization and be stable in the presence of external fields. Uniaxial magnetic anisotropy is essential in hard magnetic materials, as are the following magnetic characteristics [75]. Figure (2-10) depicts the hysteresis loop of a hard magnetic material. The following are some of the most important features of hard magnetic materials:

**High coercivity:** A ferromagnetic material's coercivity, also known as the coercive field, is the strength of the applied magnetic field necessary to reduce the magnetization of that material to zero once it has been driven to saturation. Hc is the abbreviation for coercivity, which is commonly measured in Oersted or ampere/meter units. Hard ferromagnetic materials, which have a high coercivity, are utilized to manufacture permanent magnets [76].

**Large magnetization:** is the process of temporarily or permanently making a substance magnetic, such as by putting it in a magnetic field.

Rectangular hysteresis loop: A hysteresis loop depicts the connection between the magnetizing force (M) and the induced magnetic flux density (B) (H). The hysteresis loop in hard magnetic materials is rectangular [77].

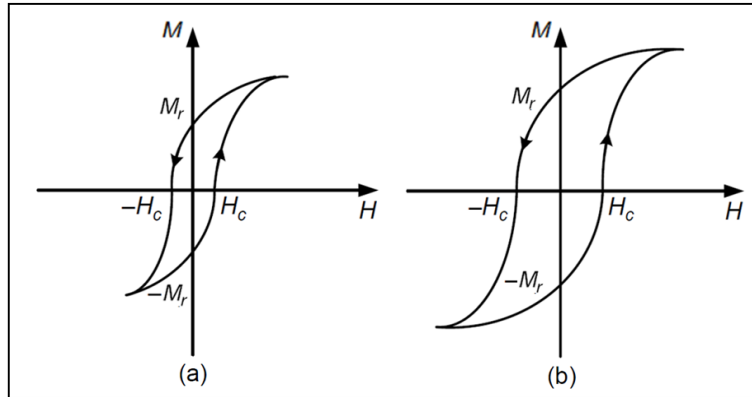


**Figure (2.10): Comparison of hysteresis loops for: (a) soft ferrites; (b) hard ferrites [78].**

**(2.9) Dielectric properties**

If a substance has the potential to retain energy when an external electric field is applied, it is classed as "dielectric. These qualities alter with frequency, temperature, orientation, mixing, and pressure, as well as the material's molecular structure. There is no net dipole moment in most solids because there is no net separation of positive and negative charges. Solids' molecules are organized in such a way that the crystal's unit cell has no net dipole moment. The molecules of solids are structured in such a way that the unit cell of the crystal has no net dipole moment. A distortion of the electron cloud of the atoms or molecules, as well as a tiny movement of the atoms themselves, produce this field. The electrical polarization is the average dipole moment per unit volume induced in the material and is proportional to the applied electric field. [79] defines the dielectric's polarizability as follows:

$$P = \alpha E \dots\dots\dots (2-2)$$

where p is the dipole moment caused by the local electric field, and E is the electric field. [80].

Polarizability is classified into four types, each with its own process based on the sort of dipole moment that is created[81]:



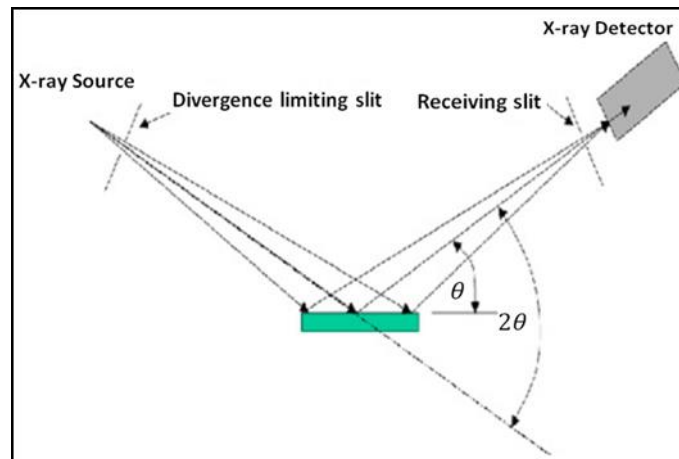


Figure (2.11): Schematic representation of x-ray diffraction [84].

**(2.10.1) Lattice Constant (a)**

1. The lattice constant The constant of the cubic crystal structure can be calculated using the following formula: [85].

$$\frac{1}{d^2} = \frac{h^2+k^2+l^2}{a^2} \dots\dots\dots (2-4)$$

a: The crystalline cube structure's lattice constant(hkl): Miller indices.

d: The distance between crystalline surface levels.

2. Lattice constant The following relationship may be used to derive the constant for the tetrahedral crystalline structure: [85].

$$\frac{1}{d^2} = \frac{h^2+k^2}{a^2} + \frac{l^2}{c^2} \dots\dots\dots (2-5)$$

c: constant in the crystalline tetrahedral structure

**(2.10.2) Spacing of Lattice Planes**

The symbol d stands for the perpendicular distance between each lattice plane in a stack. The connection between d spacing and the specific lattice plane is dhkl (i.e., d001, d101, d103), with the Miller indices for that plane provided in the subscript. In crystallography and X-ray diffraction, this is the most frequent nomenclature. The values of d spacing in terms of hexagonal systems are shown in equations (2-3), monoclinic systems in equations(2-4), and cubic systems in equations (2-4). (2-5) [86].

$$\mathbf{d} = \left[ \frac{4}{3a^2}(\mathbf{h}^2 + \mathbf{hk} + \mathbf{k}^2) + \frac{l^2}{c^2} \right] \dots\dots\dots(2-6)$$

The following equation shows the values of d spacing for monoclinic: [86].

$$\mathbf{d} = \left[ \frac{\frac{\mathbf{h}^2}{\mathbf{a}^2} + \frac{l^2}{\mathbf{c}^2} - \frac{2\mathbf{hl} \cos \beta}{\mathbf{ac}}}{\sin^2 \beta} + \frac{\mathbf{k}^2}{\mathbf{b}^2} \right] \dots\dots\dots(2-7)$$

In the equation, the value of d spacing for cubic is shown: [86].

$$\mathbf{d} = \frac{\mathbf{a}}{\sqrt{\mathbf{h}^2 + \mathbf{k}^2 + \mathbf{l}^2}} \dots\dots\dots(2-8)$$

### (2.10.3) Average crystallite Size

Using Debye-Scherrer equation

The Scherrerr equation [87] can be used to compute the crystal size.

$$D = \frac{K\lambda}{\beta_{hkl} \cos \theta} \dots\dots\dots(2-9)$$

D: average crystallite Size (nm)

K: A constant with a value that is roughly equivalent to (0.9).

$\lambda$ : wave length (nm).

( $\beta_{hkl}$ ): the highest width at the mid-thigh (rod).

$\theta$ : angle of X-ray fall.

### (2.11) Applications of the hard ferrites

Ferrite magnets are employed in a variety of applications, from magnetic holding tools to motors and generators, due to their inexpensive cost. In existing systems, ferrites have replaced other magnet materials, either with or without system change. This is particularly true in static situations with tiny demagnetizing forces. In loudspeaker systems, for example, flat ring magnets are used instead of high metallic center core magnets. The high  $H_c$  has aided the development of the new system, particularly in dynamic applications where significant demagnetizing forces are present on a regular basis. The electric motor, with its high armature electric field, is a good example.

Other than permanent magnets, hard ferrite has applications in microwave, magnetic bubble memory, magnetic tape recording, and magneto-optics. M-type ferrites are of interest in microwave resonance devices such as isolators, filters, and circulators. Such devices often use a garnet or spinel ferrite in conjunction with the bias magnets below 20 GHz. The needed bias field ( $>570$  kA/m) gets impractically high at high frequencies. M-type ferrites are favored because they have a significant anisotropic field that functions as a built-in bias field and provides a resonance frequency of around 50 GHz in a tiny tuning field.

Various substitutes can be used by the alter of HA for larger frequency coverage. Other applications of magnets include magnetotherapy, purification, magnetic bearings, and automated cameras, to name a few [88].

### (2.12) Fourier Transform Infrared (FTIR) Spectroscopy

By providing an infrared absorption spectrum as a molecular "fingerprint," Fourier transform infrared spectroscopy (FTIR) is a strong method for recognizing different types of chemical bonds present in a molecule. The chemical bond's absorbed wavelength is one of its characteristics. The frequency of molecular bonding varies depending on the kind of bond and the components present [89,90]. The cation masses, cation oxygen bonding, and lattice parameter all affect vibration frequencies in IR spectra. The absorption bands  $\nu_1$  and 2 in the IR spectra of spinel ferrites correspond to tetrahedral (A-O) and octahedral (B-O) sites, respectively [91]. The equation[90] was used to calculate the force constants at tetrahedral and octahedral sites. FTIR spectra of zinc-manganese ferrite samples were obtained by FTIR spectrophotometer (Japan) [92].

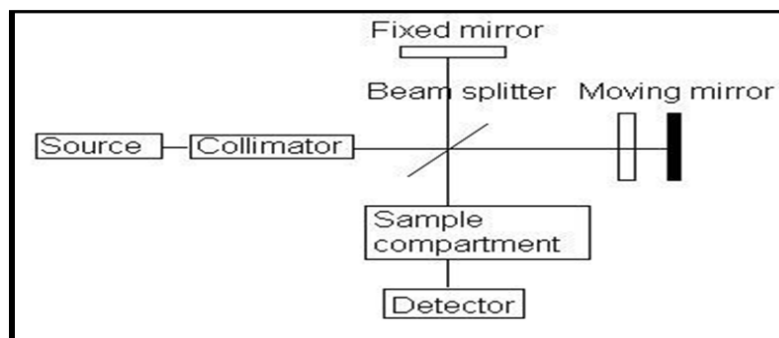


Figure (2.12): Block diagram of FTIR[92].

### (2.13) Vibrating sample magnetometer

Simon Foner designed the vibrating sample magnetometer (VSM), which is a device for measuring the magnetic behavior of materials. The (VSM) is based on Faraday's Law of Induction, which states that a change in the magnetic field causes an electric field to be generated. His electric field may be monitored, and this information can be used to deduce specifics about the changing magnetic field [93]. The instrument system is based on the idea that vibrating a magnetic sample can cause a magnetic field to oscillate. The sample is subjected to a homogeneous magnetic field. A search coil detects the generated variations in the magnetic field, which are caused by magnetization. The schematic diagram of a typical VSM is shown in Figure 2.13. A powerful electromagnet with a field of 0 to 2.5 T is employed in most conventional configurations [94].

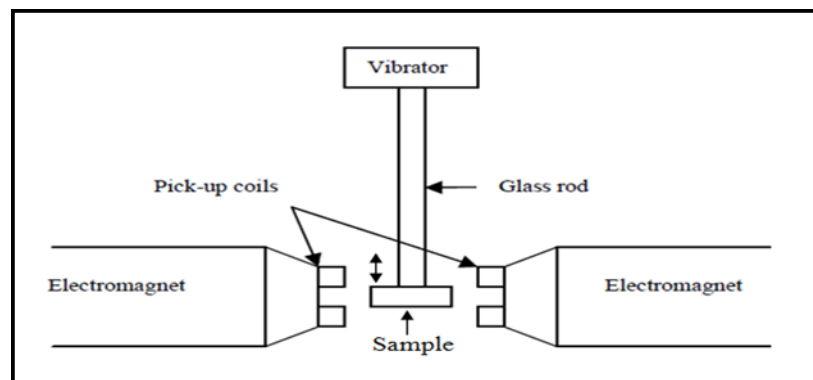


Figure (2.13): Schematic diagram of vibrating sample magnetometer system [95].

### (2.14) Hysteresis loop and magnetic parameters

It is possible to learn a lot about magnetic materials by evaluating the hysteresis loop. The strength and direction of the magnetizing field determine the magnetization state of a material. If we take a material with numerous tiny magnetic domains but no net magnetization, we may investigate what happens to the domains when the field strength is raised [96]. A hysteresis loop is seen graphically in Figure 2.16. (magnetization  $M$  as a function of an applied magnetic field  $H$ ). As a result, a hysteresis loop is created by measuring a sample's magnetic moment while cycling the applied field between the vast range of positive and negative values [98].

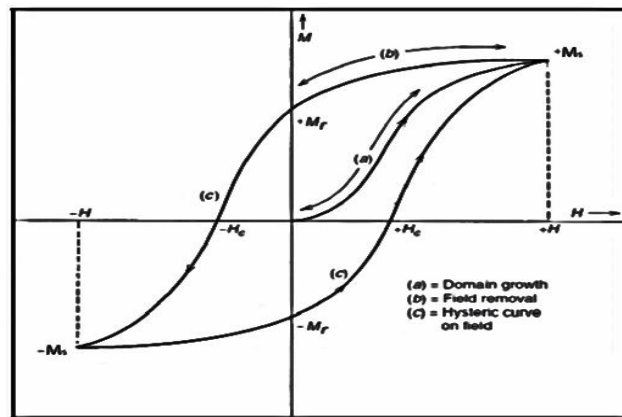


Figure (2.14): Hysteresis loop for ferromagnetic materials [97].

As a result, a hysteresis loop is created by measuring a sample's magnetic moment while cycling the applied field between the vast range of positive and negative values [98]. The domain growth region is the name given to this area. The magnetization approaches saturation point with sufficiently high applied fields, when all magnetic dipoles are aligned with the external field. The saturation magnetization ( $M_S$ ) is the greatest value of magnetization reached in this condition; at this point, the magnetization becomes constant [97,99]. Spins cease to be aligned with the magnetic field when the magnetic field is reduced to zero, resulting in a drop in total magnetization. Curve (b) shows how the magnetization does not follow the direction of the original curve but instead lags behind, resulting in a permanent induction. Even when the applied field is zero, the material is magnetized, which is known as remnant induction (remanent magnetization  $M_r$ ) [96,100].

The spin orientations inside domains have readily rotated back to their advantageous crystallographic locations at this time, but the original random domain layout is not attained because domain wall motion is constrained and the domain development process is not totally reversible [97].

To return the magnetic induction to zero, an antiparallel field of magnitude ( $H_c$ ), known as the coercivity, must be supplied to the initial magnetic field, as illustrated in curve (c). Magnetic saturation ( $M_S$ ) in the reverse direction is caused by a rise in magnetic field intensity in the opposite direction, resulting in saturation and remanence values ( $M_r$ ). The field can be reversed once again, and the loop's field induction closed. The energy loss per unit volume of material for one cycle is represented

by the area within the hysteresis loop [97]. The hysteresis loop is followed when the applied field is cycled from one direction to the other. The work or energy required to cause changes in the magnetic domain structure is represented by the hysteresis loop area, while the product  $M-H$ , also known as the energy product, indicates the net loss in the system, which is normally in the form of heat [96].

Anisotropy constant may be calculated using the law of approach to saturation (LAS) (K). It is obtained by the relation for isotropic cubic: [101]

$$K = M_s \sqrt{\frac{105 b}{8}} \dots\dots\dots (2.18)$$

The  $M-H$  curve at high magnetic field strength ( $H \gg H_c$ ) is used to calculate it. The magnetization near the saturation ( $M_s$ ) may be represented as [101, 102]:

$$M = M_s \left( 1 - \frac{b}{H^2} \right) \dots\dots\dots (2-19)$$

The magneto-crystalline anisotropy gives rise to the parameter  $b$ . The intercept of the straight line indicates the value of  $M_s$ , and the slope  $= M_s b$ , as obtained by plotting  $M$  vs  $1/H^2$  at a high field range.

$$\text{Remnance ratio} = \left( \frac{M_r}{M_s} \right) \dots\dots\dots (2-20)$$

The magnetic moment ( $n_B$ ) per unit at the magnetic moment can calculated with the assistance of the saturation magnetization value from the following relationship [101].

$$n_B = \frac{M_{wt} \times M_s}{5585} \dots\dots\dots (2-21)$$

Where,  $M_{wt}$  is the molecular weight.

Further, the anisotropy constant is evaluated using following relation [102].

$$H_c = \frac{0.96 \times K}{M_s} \dots\dots\dots (2-22)$$

Where,  $K$  is magnetic anisotropy,  $H_c$  is the coercively.

### (2.15) Dielectric Parameters

LCR Meter Bridge was used to calculate the dielectric constant. Silver paint was sprayed on both sides of the pellets for this purpose in order to produce effective ohmic contacts with the conducting wires. It is defined as the ratio of the charge that would be stored in empty space to the charge that would be stored in the dielectric substance in question. The LCR meter was used to determine the pellets' capacitance, and the dielectric constant was computed using the formula [95]:

$$\epsilon' = C / C_0 \quad \dots\dots\dots (2-12)$$

C the material's capacitance,  $C_0$  is the capacitance of empty space, and

$$C_0 = \epsilon_0 A / d \quad \dots\dots\dots (2-13)$$

Where  $\epsilon_0$  is the free space permittivity, which has a value of (8.85410-12 Fm-1).

The equation (2-5) becomes.

$$\epsilon' = C d / \epsilon_0 A \quad \dots\dots\dots (2-14)$$

Where d is the pellet thickness in meters and A is the cross-sectional area of the particle's flat surface [95].

$$\tan \delta = \epsilon'' / \epsilon' \quad \dots\dots\dots (2-15)$$

where,  $\epsilon'$  and  $\epsilon''$  are real and imaginary part of relative permittivity

Where d is the pellet thickness in meters and A is the cross-sectional area of the particle's flat surface [95].

When an ac voltage is applied to a dielectric, the electrical energy is absorbed by the substance and released as heat. Dielectric loss is the term for the dissipation. Resonance happens when the applied frequency is in the same range as the relaxation duration. The phase connection between current and voltage is seen in Figure (2-15). As a result, the current is (90-  $\delta$ ) ahead of the voltage. where  $\delta$  is the loss angle and tan is the electrical loss due to resonance, which is referred to as tangent loss, and the loss tangent can be written as [96]:

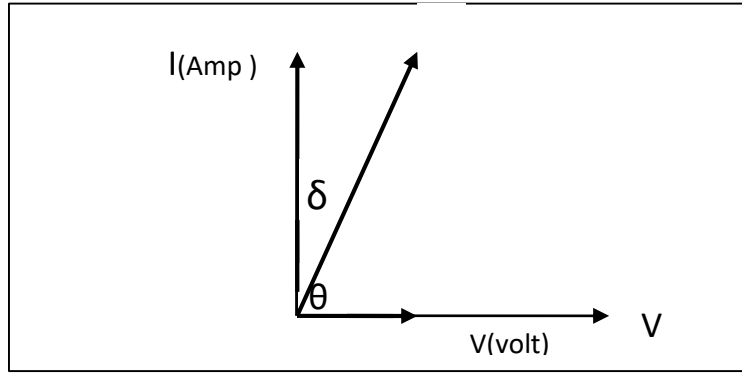


**Figure (2.15): Phase diagram between voltage and current [96].**

Using the relation, the ac conductivity was derived from the dielectric constant and dielectric loss factor measurements. [97] :

$$\sigma_{ac} = \omega \epsilon_0 \epsilon' \tan \delta \dots\dots\dots (2-16)$$

$\sigma_{ac}$  is the ac conductivity,  $\omega$  is the angular frequency.

$$\epsilon'' = Gd / \epsilon_0 A \omega \dots\dots\dots (4-2)$$

Where ( $\omega = 2\pi f$ ) is the angular frequency and G is conductance, which is the reciprocal of resistance R. The standard unit of G is Siemens (S) [95].

### (2.16) Electrical Conductivity

Ferrites are valuable in a range of technological applications due to their high electrical resistance. Spinel ferrites' electrical conductivity is significant because it offers essential information about the conduction process. The nearest-neighbor hopping process is thought to be responsible for electrical conductivity. Due to the existence of iron with a different valence state at crystallographically equivalent lattice sites, these systems have a lot of conductivity. The distribution of cations in sites via magnetic and non-magnetic replacements, chemical composition, particle size, sintering conditions, technique of manufacture in general, and their structure in particular, all have an influence on ferrites' electrical properties. According to Phillips et al. [98], the establishment of a Coulomb gap is generated by electron interactions caused by the huge number of excess charges in Fe<sup>2+</sup> ions at the B site. Electrical conductivity has been explained as being dependent on nearest-neighbor hopping at high temperatures and variable range hopping at low temperatures when Fe<sup>2+</sup> concentrations are low. Due to their lower electrical conductivity than metals, ferrites are well-known as ideal basis materials for magnetic devices that run at high frequencies, such as



achieved in a variety of ways. Allowing time for sedimentation and then pouring out the leftover liquid is the easiest way. Centrifugation can also be utilized to speed up the phase separation process. Drying is required to remove the residual liquid (solvent) phase, which is usually accompanied by substantial shrinkage and densification [105].

The distribution of porosity in the gel ultimately determines the pace at which the solvent may be extracted. Changes placed on the structural template during this processing phase will have a significant impact on the final component's microstructure. Then by final sintering, densification, and grain formation, a thermal treatment, or fire procedure, is required to favor additional poly- condensation and to improve mechanical characteristics and structural stability. One of the major advantages of this procedure over more typical processing methods is that densification can frequently be accomplished at considerably lower temperatures.

The sol-gel method is a low-cost, low-temperature method for carefully controlling the chemical composition of a product. Even tiny amounts of dopants, such as organic dyes and rare earth elements, can be incorporated into the sol and spread evenly in the final product. It can be utilized as an investment casting material in ceramics processing and manufacturing, or as a method of generating very thin metal oxide films for different uses. Materials generated from sol-gel offer a wide range of applications in optics, electronics, energy bio-sensors, and medicine [105].

### **(2.18) Polarization**

In normal electrical conductivity, electrical insulators have extremely few free electrons. Because an electric field may polarize a material to generate an electrical dipole, it has intriguing electrical characteristics [106,107]. Insulating material molecules are termed (Non polar molecules). Dipoles can appear dipole in a material when a field is present, but they can also be present as a permanent part of the molecular structure. Such dipoles are known as (permanent dipoles) because the

positive charge's center does not correspond with the negative charge's center. Insulating materials molecular are known as (polar molecules). Electric polarization [108] is the induction of dipoles.

The polarization phenomenon (P) is described as the change in the arrangement of electrically charged particles of a dielectric in space, or the surface charge density in a dielectric, equal to the dipole moment per unit volume of material as follows:

$$P = Nm \quad \dots(2-20)$$

where:

The number of dipoles per unit volume is denoted by N.

The average dipole moment is denoted by the letter m.

The electric dipole moment is defined as the separation of two electric charges of opposing polarity q by a distance (d) [109]:

$$m = qd \quad \dots(2-21)$$

## **(2.19) Types of Polarization:**

### **( 2.19.1) Electronic or Induced Polarization**

The polarization created by the displacement of electrons is known as electronic polarization. A dielectric is made up of a lot of atoms. When a dielectric substance is made up of only one atom, the nucleus is in the center, and the electrons revolve around it. When an external electric field is applied, the nucleus travels away from the field, while the electrons move towards it. As a result, a distance between the nucleus and the electrons is created. Induced dipole moment and polarization result from this displacement [110]. Electrons and positively charged nuclei will be displaced in such a way that electrons move in the positive field direction and nuclei in the opposite direction, as shown in figure 2.16-a. [111].

### **(2.19.2) Atomic or Ionic Polarization**

When an electric field is applied to an ionic crystal, the negative ions are displaced towards the field, while the positive ions are displaced away from the field, resulting in polarization. Atomic or ionic polarization is the name for this type of polarization [112]. Figure 2.16-b depicts the situation [111].

**(2.19.3) Dipolar or Orientation Polarization**

Polar substances such as H<sub>2</sub>O, HCl, nitrobenzene, and others cause dipolar polarization. When an electric field is supplied to a polar molecule, the dipoles experience torque and attempt to align parallel to the applied field, resulting in dipole rotation and polarization [112]. The total result, as shown in figure 2.16-c, will be to produce a dipole moment within the solid [111].

**(2.19.4) Interfacial or Space Charge Polarization**

If two electrodes are separated by a dielectric medium. The positive and negative charges are not separated in the absence of an electric field, and there is a constant number of charges. The charges are separated when an external electric field is applied. As a result, positive charges condense towards the negative electrode. As a result of the ions' displacement, a dipole moment is generated. Interfacial polarization [112] describes the induced dipole moment per unit volume. Charge builds at the electrodes at the interface in a multiphase material, resulting in space charge, as seen in figure 2.16-d. [111].

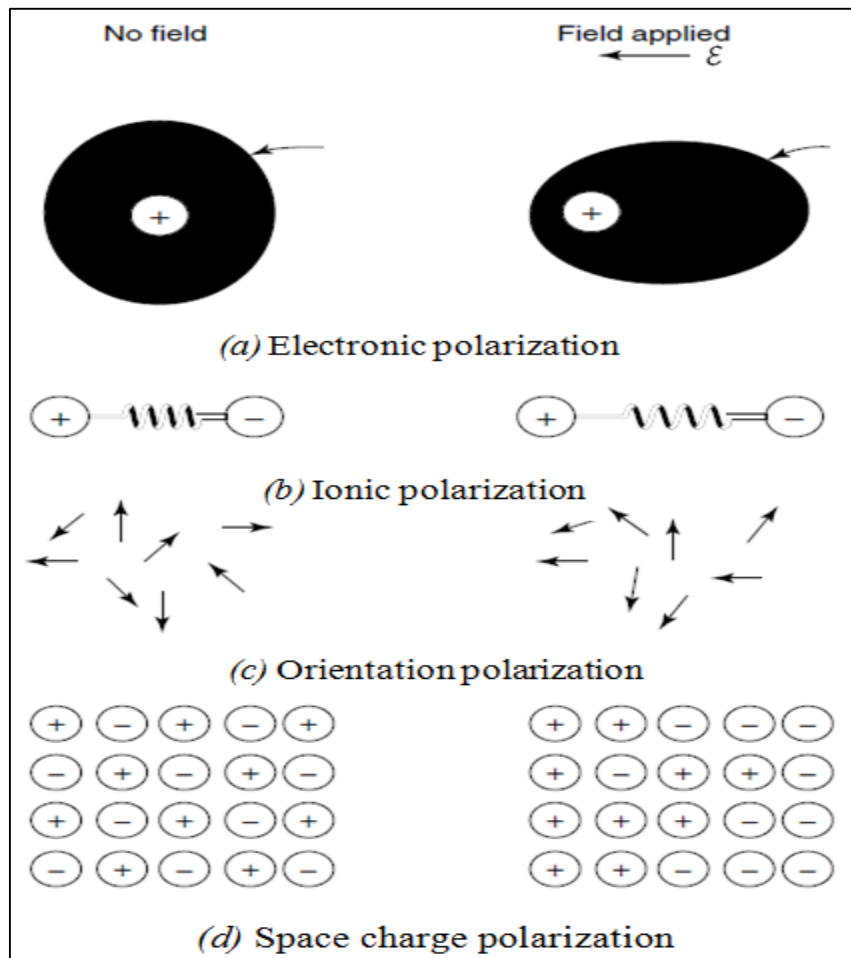


**Figure (2.16): Schematic diagram of (a) Electronic polarization, (b) Ionic polarization, (c) Orientation polarization, (d) Space-charge polarization [111].**



---

# Chapter Three

---

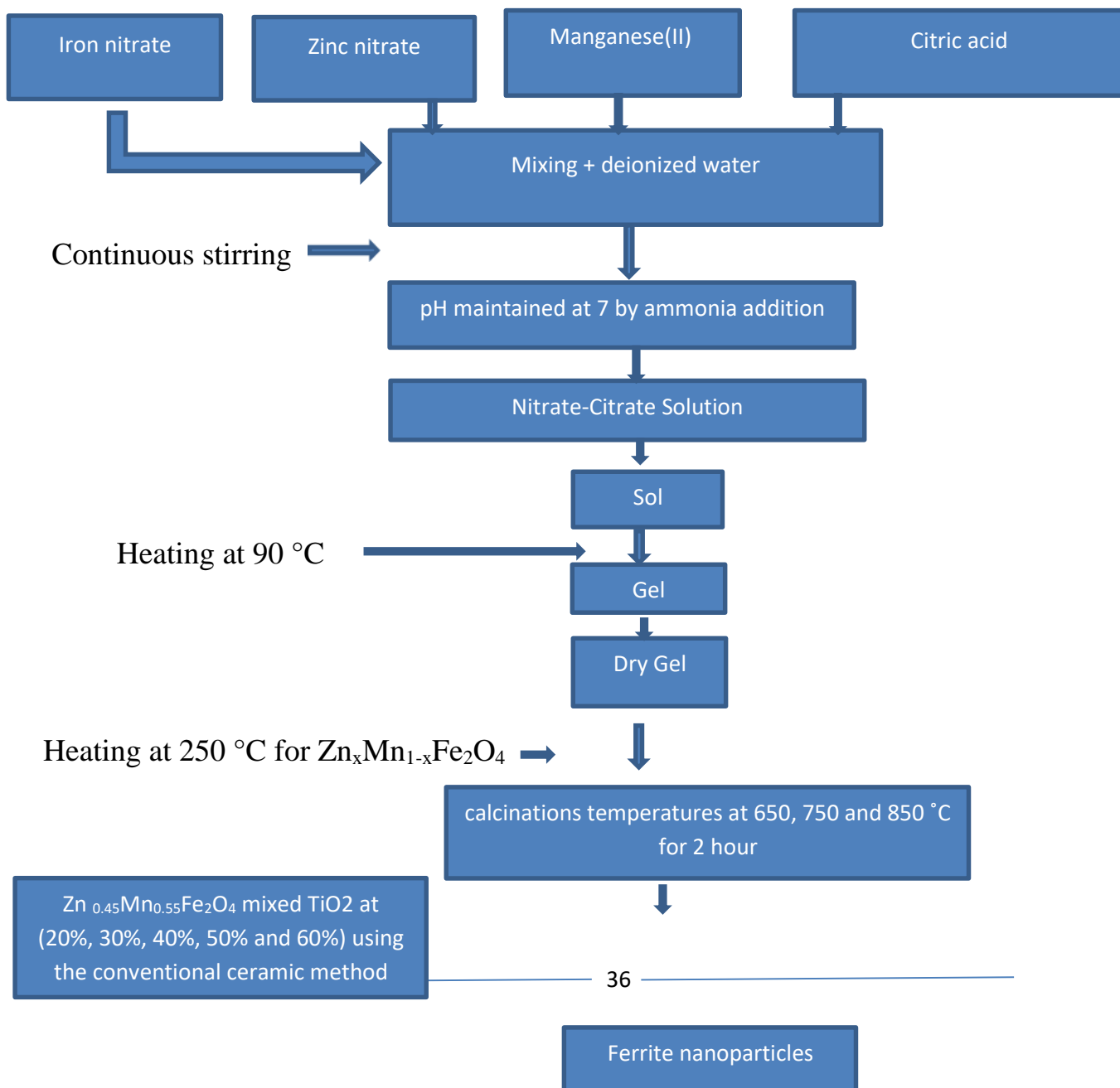
Experimental work





### (3.1) Introduction

This chapter describes synthesis pathways using the Sol-gel auto combustion process, as well as numerous approaches for characterisation and analysis of nano materials. Techniques for characterisation of nano materials include X-ray diffraction (XRD), Fourier transforms infrared (FTIR) spectroscopy, field emission scanning electron microscopy (FE-SEM), LCR meter, and vibrating sample magnetometer (VSM). This chapter discusses the practical steps involved in preparing the ferrite models  $Zn_xMn_{1-x}Fe_2O_4$  ( $x=0, 0.15, 0.25, 0.35, \text{ and } 0.45$ ) and (20%, 30%, 40%, 50% and 60% ) of  $Zn_{0.45}Mn_{0.55}Fe_2O_4/TiO_2$  as well as the materials used in specimens the preparation methods, Calcination and compression, sintering, and electrical and magnetic tests and the devices are also presented here. Experimental work shows in figure (3.1).



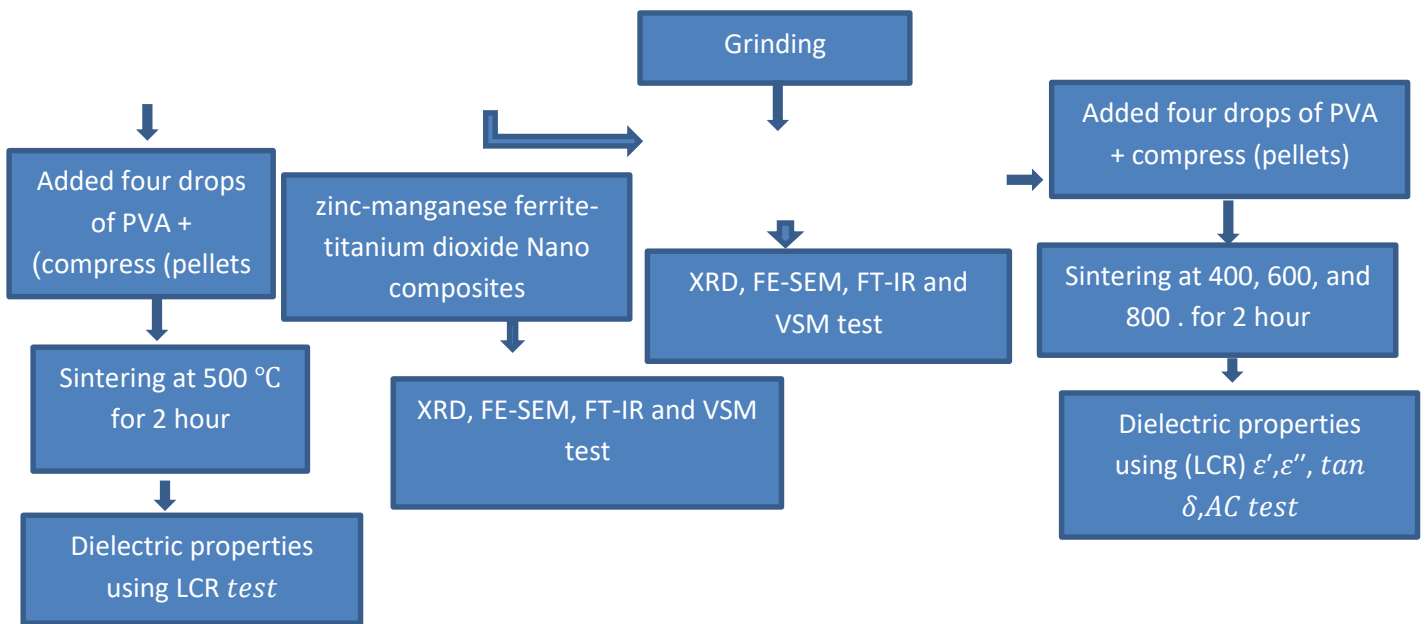


**Figure (3.1):** The diagram of sol-gel auto combustion synthesis of  $Zn_xMn_{1-x}Fe_2O_4$  Nano ferrites and  $Zn_{0.45}Mn_{0.55}Fe_2O_4/TiO_2$  nanocomposites.

We have used a set of devices for the purpose of testing the prepared samples.

### (3.2.1) Mass Measurement Instrument

In this investigation, it was utilized. The balance of four decimal points with a high degree of sensitivity. Is illustrated in with type DENVER instrument is of American origin. as shown in figure (3.2).

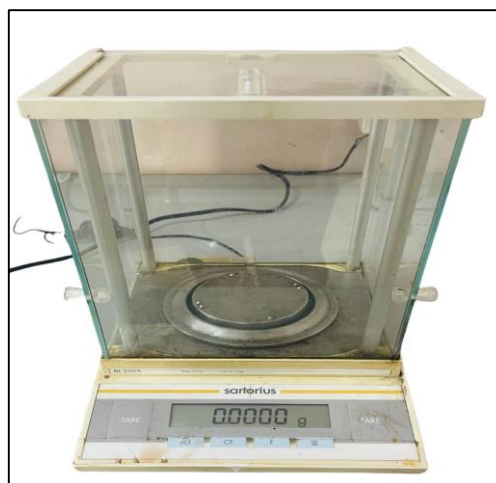


**Figure (3.2):** Electric Balance used

### (3.2.2) Magnetic Stirrer

It's a laboratory apparatus that uses a rotating magnetic field to make a stir bar immersed in a liquid to spin rapidly, churning it. A rotating magnet or a group of fixed electromagnets positioned beneath the liquid-filled vessel can produce the spinning field. For obtaining a homogeneous mixture between atoms and liquid particles, magnetic stirrers sometimes contain a heated plate or some other method of heating the liquid, Type "DAIHAN" Korea origin. as shown in figure (3.3).

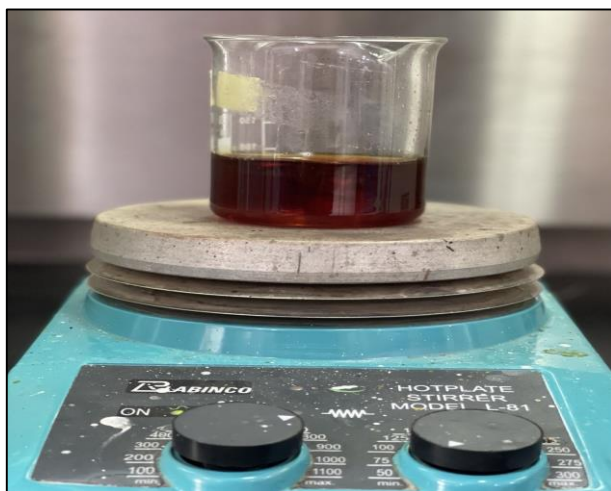


Figure (3.3): Magnetic stirrer

### (3.2.3) Electrical furnace

The prepared Zn-Mn ferrite nano powders were calcined in an electric oven (Korean from Labtech) at 1200°C As show in figure (3.3). The room size is 40x20x20 cm. The thermal system of the furnace was controlled by a programmed control unit "Eurotherm". Zn-Mn ferrite nanopowders were calcined at temperatures (650, 750 and 850 °C) for 2 h, and then the powders were cooled to room temperature. As show in figure (3.4).

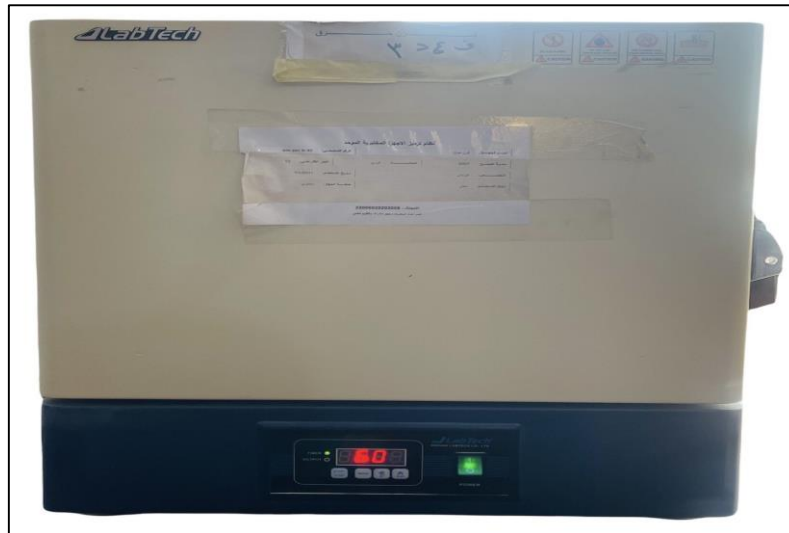


Figure (3.4): Electrical furnace

### (3.2.4) Hydraulic press

Hydraulic piston (8000 Pascale, Italy), mold in 1cm diameter. is shown in figure (3.5).



Figure (3.5): Hydraulic press.

### (3.3) The materials used

The materials used in the preparation of the ferrite compound by sol-gel auto combustion method are listed in table (3.1) with their full descriptions.

Table (3.1): The chemical materials and their properties

Materials	Compounds	Chemical formula	Mol. mass (g mol <sup>-1</sup> )	Purity%	Origin
	Titanium tin oxide	TiO <sub>2</sub>	79.87	99.00	USA
	Iron (III) nitrate	Fe(NO <sub>3</sub> ) <sub>3</sub> .9H <sub>2</sub> O	404.00	97.00	India
	Citric acid	C <sub>6</sub> H <sub>8</sub> O <sub>7</sub> .H <sub>2</sub> O	210.14	99.00	USA
	Ammonia solution	NH <sub>4</sub> OH	35.05	25	India
	Zinc nitrate	Zn(NO <sub>3</sub> ) <sub>2</sub> .6H <sub>2</sub> O	297.37	98.0	India
	Manganese(II) nitrate	Mn(NO <sub>3</sub> ) <sub>2</sub> .4H <sub>2</sub> O	250.93	98.0	USA

### (3.4) Preparation of ferrite materials

1- All metal nitrate and citric acid were dissolved in 15 ml of distilled water.

2- All of them are combined in a glass beaker to form a complete solution, which is thoroughly mixed at room temperature with a magnetic stirrer at high speeds for a short time (30 minutes), until the solution becomes smooth and slimy red-colored, as shown in figure (3.6 a). Ammonia solution was steadily added into the mixed solution in the form of drops with continual stirring to regulate its pH until it reached the value of (7), resulting in a dark brown as seen in the figure (3.6 b). To achieve

homogeneity, stir the components together for half an hour at room temperature. Gradually raise the temperature until it reaches 90 °C, stirring constantly until the gel form.

3- The size of the solution in the glass beaker is reduced and viscosity increased, and after (30 minutes), the solution viscosity is very high, resulting in the beginning of gel formation on the surface of the solution, particularly in the middle, and then all of the solution turns to gel, and even at this point, the solution is still on the magnetic stirrer and temperature (90°C), as shown in figure (3.6 c).

4- The temperature decreases to room temperature after the solution turns to dark brown gel, where the gel is placed in a glass beaker using a sensitive balance, and then placed in the oven at 150°C for three hours to dry as shown in figure (3.6 d). After evaporating the material and raising the temperature of the dried gel to (250°C), the dry gel began to change shape and become convex in the middle of the glass beaker after 15 minutes, as illustrated in figure (3.6 e).

5- After combustion, the dried gel turns into a fine powder with a dark gray hue, signaling the start of the creation of high purity ferrite, as illustrated in the figure (3.6 f).

6- The ferrite powder was then calcined for two hours at temperatures of (650,750, and 850°C) to improve crystallization and homogenous action distribution, and then ground to produce  $Zn_xMn_{1-x}Fe_2O_4$  ferrite Nano powders.

### **(3.4.2) Preparation of (Zn Mn Fe<sub>2</sub>O<sub>4</sub>/TiO<sub>2</sub>) nano composites**

Using the traditional ceramic method, titanium dioxide (TiO<sub>2</sub>) is mixed with zinc-manganese ferrite in (20%,30%,40%, 50%, and 60%) and sintered at 500°C.

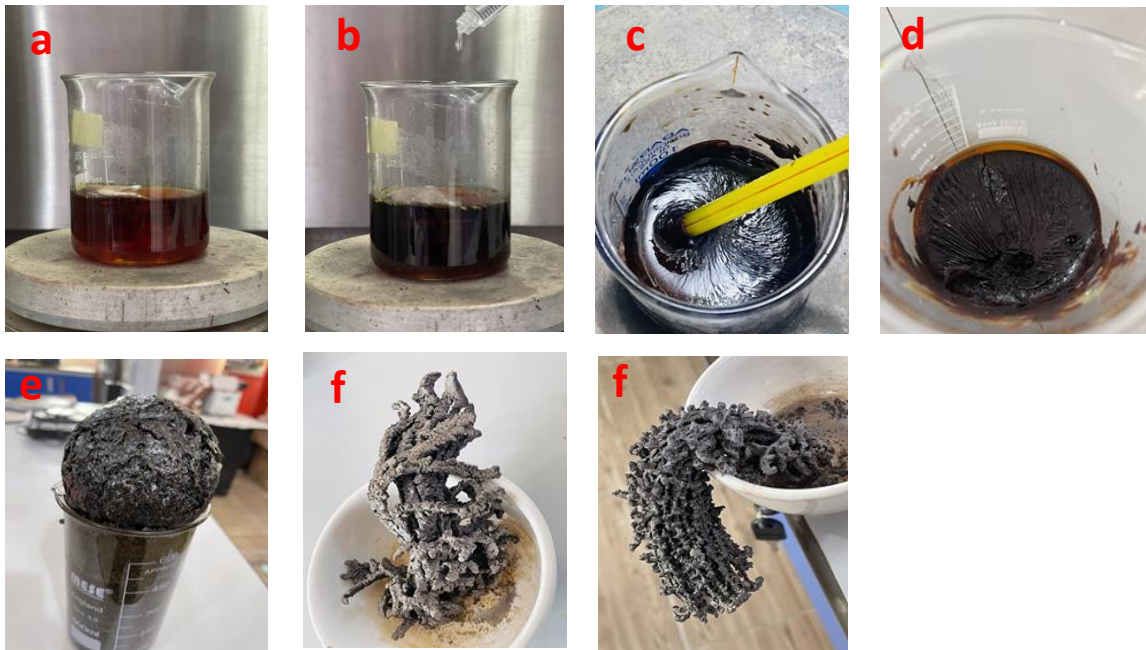


**Figure (3.6):** Photograph of (a) nitrate-citrate solution, (b) The solution after the Adding of ammonia, (c) dry gel, (d) Dry bulk temperature of 150°C, (e) Dry bulk temperature of 250°C and (f) auto combustion and become Nano powder ferrite.

### (3.5) Calcinations and Pellet Formation

The resulting powder is placed in a ceramic pot and then calcined at 650, 750, 850 °C for two hours to remove reaction residues such as water or carbon dioxide molecules form in combustion, resulting necessary ferrite powder. Then 0.5 g of burnt powder were taken and five drops of PVA were added as a binder to be pressed into round pellets 1 cm in diameter and 3mm thick. This is achieved by pressing 2000 Pa for five minutes with a hydraulic press, then sintering at 400, 600 and 800°C for two hours and allow them to cool slowly naturally to study their electrical properties, as shown in figure (3.7).

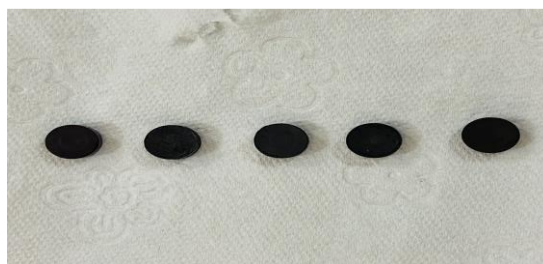


**Figure (3.7):** Transformation of powder to compact sample

### (3.6) Structural characterization and testing

#### (3.6.1) X-ray Diffraction (XRD)

The phase composition and crystal structure of the samples are examined using an X-ray diffractometer. Model XRD 6000 (Shimadzu-Japan) shown in figure (3.8). with high-intensity Cu K radiation (1.540nm), scan range: (10- 90 deg), and scan speed 6 (deg/min) was used for the measurement. By comparing the X-ray diffraction patterns of samples to (JCPDS) standard data, crystalline substances and phases may be identified. the crystal structure test was carried out of the synthesized  $Zn_xMn_{1-x}Fe_2O_4$  ferrite nanoparticle specimens ( $x= 0, 0.15, 0.25, 0.35,$  and  $0.45$ ) and calcined powders at various temperatures 650,750, and 850 °C and  $ZnMnFe_2O_4/TiO_2$  nano composites (20%, 30%, 40%,50% and 60%) at 500 °C.



Figure (3.8): X-ray diffraction instrument.

#### (3.6.2). Fourier Transform Infrared (FTIR)

Fourier transform infrared analysis aids in the comprehension of materials and products by providing quantitative and qualitative analysis for both organic and inorganic samples. Fourier Transform Infrared (FT-IR) is the preferred method of infrared spectroscopy. Infrared spectroscopy involves passing IR photons through a sample. The sample absorbs part of the infrared light and passes some of it through transmitted. No two distinct molecule configurations create the same infrared spectrum, much like

fingerprints. FTIR may also help with things like: identifying unknown materials determining the quality or uniformity of a sample determining the number of components in a combination The SHIMADZU-8400S FTIR spectrophotometer was used to obtain FTIR spectra of zinc manganese nitrate ferrite samples (Japan). Figure (3.9) displays an FTIR spectrophotometer. As test was carried out in research Lab., physics department, college of science at diyala University.



Figure (3.9): FTIR spectrophotometer.

### (3.6.3) Field emission scanning electron microscopy (FE-SEM)

We get a three-dimensional image of the model's surface using this technology, which works on the idea of electronic scanning of electrons that bounce off the model's surface. This implies the device doesn't just take a single image of the model's surface. Rather, it captures photos of each point in a cascade and then compiles them into a single black and white image of the model's surface. an picture of as-burnt and calcined specimens of  $Zn_xMn_{1-x}Fe_2O_4$  nanoferrites and  $Zn_xMn_{1-x}Fe_2O_4/TiO_2$  was taken at the center of Day Petronic Co., Tehran, Iran, using a FE-SEM model (Mira3-XMU, TESCAN, Japan). Shown in Figure 3.10.



**Figure (3.10): Photograph of field emission scanning electron microscopy instrument.**

### **(3.6.4) Energy - Dispersive X - ray Spectroscopy (EDS)**

The X-ray principle, which is based on the mutual impact of charged particles, is also used. The model's substance, such as a bundle of electrons, is bombarded with X-rays that are characteristic of the model's constituent elements, allowing the chemical composition of the model to be determined. Each chemical element has a peak in its X-ray spectrum, and the atoms must first be stimulated to produce the model's unique X-ray. This is accomplished by blasting the model with a bundle of electrons, causing an electron to be liberated from the atom's inner orbits. In order to fill the emptiness caused by the released electron, another electron made the move from a higher orbit to inhabit this vacuum. This team is unique for each element, emitting X-rays with an energy equal to the energy differential between the planes of the orbits.

### **(3.7) Magnetic properties measurement**

One of the magnetic properties is the assessment of the magnetization curve (Hysteresis loops) of the manufactured materials using a vibrating sample magnetometer measuring (VSM) equipment.

#### **(3.7.1) Vibrating Sample Magnetometer (VSM)**

The vibrating sample magnetometer is a simple but effective method for determining magnetic material properties. The VSM is a method for estimating the magnetic moment in magnetic specimens, which is the most

fundamental quantity of magnetism. When a specimen is placed in a uniform magnetic field, it creates a dipole moment proportional to the product of the specimen susceptibility and the applied field. Using a Vibration Sample Magnetometer (VSM), the magnetic characteristics of burnt and calcined  $Zn_xMn_{1-x}Fe_2O_4/TiO_2$  nano composites samples, are computed (LBKFB model Meghnatis Daghigh Kavirhigh Company). In the center of Day Patronal Co. Tehran, Iran, testing were carried out in the applied field at room temperature in the range of 15 kOe. The vibrating sample magnetometer setup used in this work is shown in Figure 3.11. In the present studied. Hysteresis loops are used for the measurement of saturation magnetization ( $M_s$ ), coercivity ( $H_c$ ) and remanent magnetization ( $M_r$ ). To obtain the squareness, magnetic moment  $(n_B)$  and the magnetic anisotropy ( $K$ ).



Figure (3.11): Vibrating sample magnetometer (VSM) instrument.

### (3.8) The Electrical Properties Measurement

The study of the dielectric characteristics of ferrite nanoparticles provides information on the electrical conduction mechanism in terms of dielectric response in an applied AC electric field. In the research lab., physics department, college of science at diyala University, the electrical properties of synthesized samples were measured using a home-made cell and an LCR meter (GW Instek LCR-8105G) on a frequency range of (200 Hz-1MHz). In the present study, the dielectric parameters such as capacitance of the pellet, dielectric loss angle ( $\tan \delta$ ) and capacitance of air with the same thickness as the pellet were measured by computerized LCR meter which is shown in figure( 3.12). Before beginning the test, the

surface of the samples in this study was smoothed, and they were placed between the poles after ensuring that the poles touched the sample surface. The data was recorded on a computer screen after the dielectric constant( $\epsilon'$ ), dielectric loss factor( $\epsilon''$ ), and a.c. conductivity ( $\sigma_{ac}$ ).

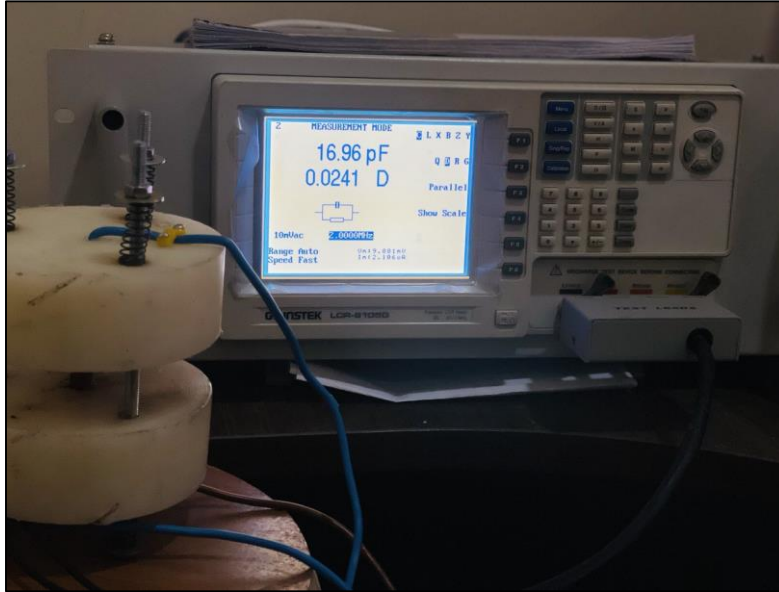


Figure (3.12): LCR meter instrument.



---

# Chapter Four

---

## Results and Discussions





## 4.1 Introduction

This chapter shows the results and discussions of structural, magnetic and electrical measurements of  $\text{MnFe}_2\text{O}_4$ ,  $\text{Zn}_x\text{Mn}_{1-x}\text{Fe}_2\text{O}_4$ , and  $\text{Zn}_x\text{Mn}_{1-x}\text{Fe}_2\text{O}_4/\text{TiO}_2$  prepared by Sol-Gel method at different temperatures (650, 750, and 850 °C). Also, this chapter discusses the characterization of the  $\text{MnFe}_2\text{O}_4$ ,  $\text{Zn}_x\text{Mn}_{1-x}\text{Fe}_2\text{O}_4$ , and  $\text{Zn}_x\text{Mn}_{1-x}\text{Fe}_2\text{O}_4/\text{TiO}_2$  nanocomposite by XRD patterns, FE-SEM analysis, EDX analysis, VSM analysis, and electrical properties.

## 4.2 Structural Characterization

### 4.2.1 X-ray Diffraction (XRD) of $\text{MnFe}_2\text{O}_4$ , $\text{Zn}_x\text{Mn}_{1-x}\text{Fe}_2\text{O}_4$ , and $\text{Zn}_x\text{Mn}_{1-x}\text{Fe}_2\text{O}_4/\text{TiO}_2$ prepared by Sol-Gel method:

The x-ray diffraction (XRD) exam carried out to investigate the crystal structure type and the crystalline size of prepared  $\text{Zn}_x\text{Mn}_{1-x}\text{Fe}_2\text{O}_4$  ferrite ( $x = 0, 0.15, 0.25, 0.35$  and  $0.45$ ) at different calcination temperatures (650, 750 and 850 °C). Figures (4-1, 4-2, 4-3, 4-4 and 4-5) present the XRD patterns of pure  $\text{MnFe}_2\text{O}_4$  ferrite those doped with different concentrations of zinc metal  $\text{Zn}_x\text{Mn}_{1-x}\text{Fe}_2\text{O}_4$  ( $x = 0.15, 0.25, 0.35$  and  $0.45$ ) respectively, synthesized by sol-gel method. Figure 4-1 the result show that pure cubic  $\text{MnFe}_2\text{O}_4$  crystal structure with space group (Ia-3 no. 206), crystal dimensions ( $a = b = c = 9.4$  Å) and crystal angles ( $\alpha = \beta = \gamma = 90^\circ$ ), corresponding with the cubic structure (JCPDS 98-003-0237). The XRD results revealed that the cubic phase of  $\text{MnFe}_2\text{O}_4$  formed at calcination temperature 650°C, and then the peaks became more sharp and intense with increasing the calcination temperature at 750 and 850 °C, this is a common behavior for all synthesized samples by sol-gel method with the calcination temperature. The XRD patterns referred that the crystalline growth of  $\text{MnFe}_2\text{O}_4$  ferrite was in the same cubic crystal structure at the different temperatures.

From figure 4-5 on can observed that at the concentration of zinc metal ( $x=0.45$ ), a pure single-phase cubic spinel  $Zn_xMn_{1-x}Fe_2O_4$  structure was obtained with space group (Fd-3m no. 277), crystal dimensions ( $a = b = c = 8.438 \text{ \AA}$ ) and crystal angles ( $\alpha = \beta = \gamma = 90^\circ$ ), agreed with the standard data (JCPDS 98-017-0912) as shown in figure 4-5. The XRD patterns at high calcination temperatures 750 and 850 °C demonstrated that the distinct structural stability of obtained  $Zn_xMn_{1-x}Fe_2O_4$  during the calcination process leads to crystalline growth in the same cubic  $Zn_xMn_{1-x}Fe_2O_4$  structure with a high purity phase, no other impurities peaks were detected, this is an indication that all the reactant metal ions entered into the cubic  $Zn_xMn_{1-x}Fe_2O_4$  structure at the concentration of zinc metal ( $x=0.45$ ) [113]. The lattice constant value as of pure cubic  $Zn_xMn_{1-x}Fe_2O_4$  ferrite nanocomposite is reduced when Zn metal added which can be explained on the basis of cations distribution, as a result of replacing larger ionic radii of  $Mn^{+2}$  cations (0.082 nm) by smaller ionic radii of  $Zn^{+2}$  cations (0.074 nm) [114,151].

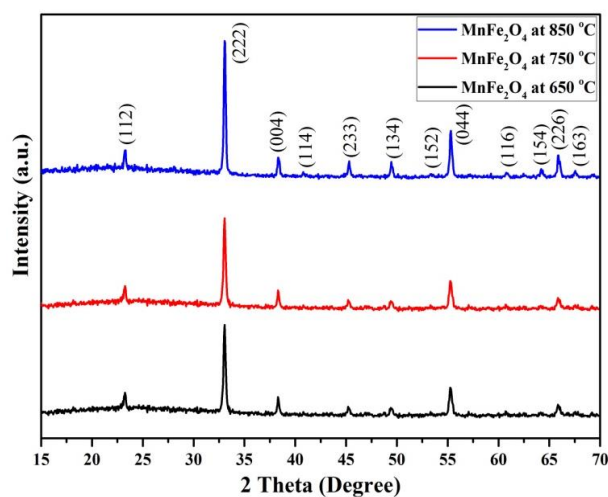


Figure (4.1): XRD patterns of  $MnFe_2O_4$  ferrites calcined at different temperatures (650, 750, 850 °C).

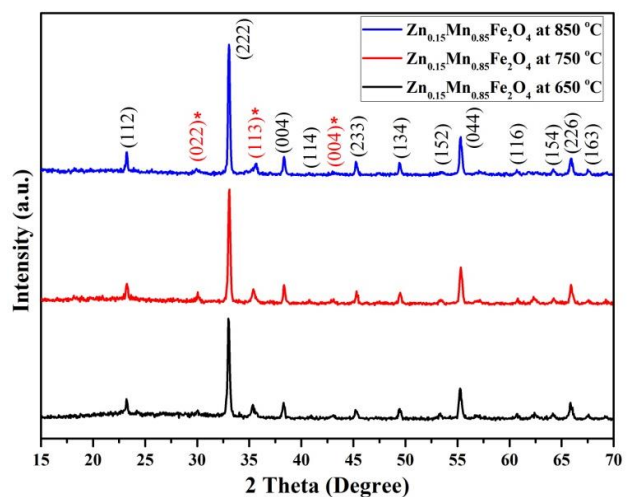


Figure (4.2): XRD patterns of  $Zn_{0.15}Mn_{0.85}Fe_2O_4$  ferrites prepared at different calcination temperatures (650, 750, 850 °C).

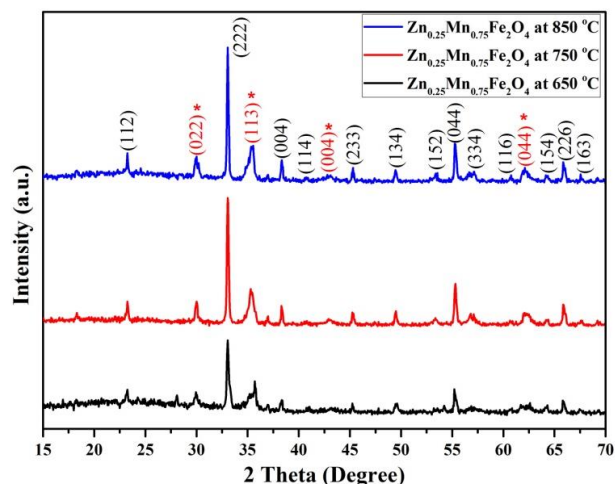


Figure (4.3): XRD patterns of  $\text{Zn}_{0.25}\text{Mn}_{0.75}\text{Fe}_2\text{O}_4$  ferrites calcined at different temperatures (650, 750, 850 °C).

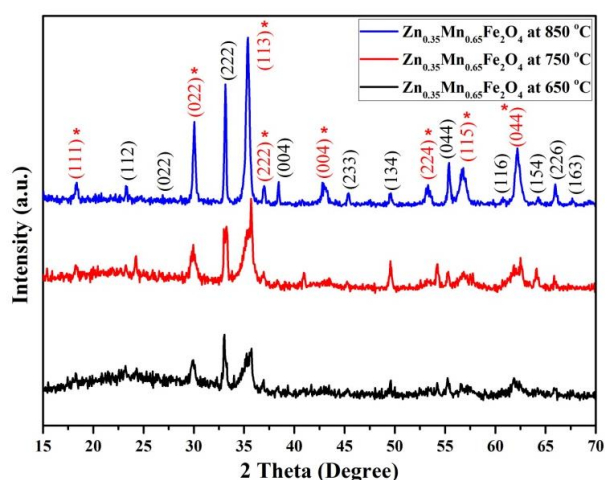


Figure (4.4): XRD patterns of  $\text{Zn}_{0.35}\text{Mn}_{0.65}\text{Fe}_2\text{O}_4$  ferrites prepared at different calcination temperatures (650, 750, 850 °C).

In order to investigate the synthesized  $\text{Zn}_{0.45}\text{Mn}_{0.55}\text{Fe}_2\text{O}_4$  ferrite mixed with different content of  $\text{TiO}_2$  nanoparticles and calcined at 500 °C, figure 4-6 presents the XRD patterns of pure  $\text{TiO}_2$  nanoparticles and  $\text{Zn}_{0.45}\text{Mn}_{0.55}\text{Fe}_2\text{O}_4$  mixed with different ratios (20%, 30%, 40%, 50% and 60%) of  $\text{TiO}_2$  nanoparticles. All the obtained peaks of  $\text{Zn}_{0.45}\text{Mn}_{0.55}\text{Fe}_2\text{O}_4/\text{TiO}_2$  (40:60%) nano composite are assigned to the characteristic peaks of two main phases which are cubic spinel  $\text{Zn}_{0.45}\text{Mn}_{0.55}\text{Fe}_2\text{O}_4$  phase (marked with red stars) (98-017-0912) and tetragonal  $\text{TiO}_2$  phase (Anatase) (marked with blue stars) with space group (I41/amd no.141) (98-015-4609), in addition to little cubic  $\text{MnFe}_2\text{O}_4$  phase (marked with black stars) (98-003-0237). The peak intensity proportion of tetragonal  $\text{TiO}_2$  (011) to  $\text{Zn}_{0.45}\text{Mn}_{0.55}\text{Fe}_2\text{O}_4$  (113) obviously increased with increase the mixed  $\text{TiO}_2$  content in the structure of  $\text{Zn}_{0.45}\text{Mn}_{0.55}\text{Fe}_2\text{O}_4/\text{TiO}_2$  nano composites.

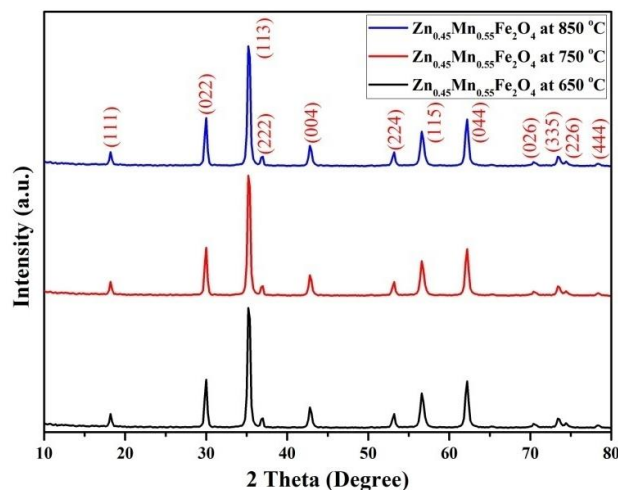


Figure (4.5): XRD patterns of  $\text{Zn}_{0.45}\text{Mn}_{0.55}\text{Fe}_2\text{O}_4$  ferrites calcined at different calcination temperatures (650, 750, and 850 °C).

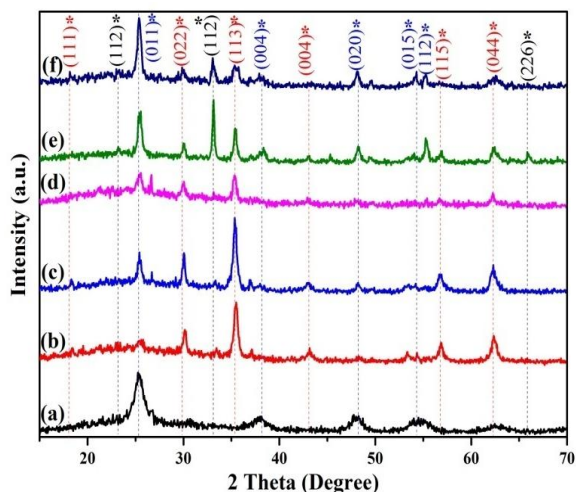


Figure (4.6): XRD patterns of (a) pure  $\text{TiO}_2$ , (b), (c), (d), (e) and (f) are  $\text{Zn}_{0.45}\text{Mn}_{0.55}\text{Fe}_2\text{O}_4$  mixed with different ratios of  $\text{TiO}_2$  (20, 30, 40, 50 and 60%) respectively.

The crystalline size of synthesized  $\text{Zn}_{0.45}\text{Mn}_{0.55}\text{Fe}_2\text{O}_4$  at different calcination temperature was calculated using the Debye–Scherrer’s equation, to be (27.99, 29.07 and 30.77 nm) at the temperature (650, 750 and 850 °C) respectively, as shown in table (4-1) and (4-2), which presents the XRD calculations of synthesized  $\text{Zn}_x\text{Mn}_{1-x}\text{Fe}_2\text{O}_4$ . the crystalline size slightly increased with raising the calcination temperature and the zinc content which is the common behavior of all synthesized material, attributed to the crystal growth with increase the calcination temperature and the zinc content, and this is corresponded with the measured XRD patterns where the intensity of the most intense peak (113) of pure  $\text{Zn}_{0.45}\text{Mn}_{0.55}\text{Fe}_2\text{O}_4$  is significantly increases and the pattern appears narrower with the increasing of Zn content [116]. On other side, the crystalline size of  $\text{TiO}_2$  nanoparticles is (10.76 nm).

**Table (4.1): XRD calculations of  $Zn_xMn_{1-x}Fe_2O_4$  with different content of zinc metal ( $x=0, 0.15, 0.25, 0.35$  and  $0.45$ ) at different calcination temperatures.**

Material	Temp. °C	2 $\theta$ (deg) Practical	2 $\theta$ (deg) Standard	FWHM (deg)	Crystalline size (nm)	d <sub>hkl</sub> (°A) Practical	d <sub>hkl</sub> (°A) Standard	(hkl)
<b>MnFe<sub>2</sub>O<sub>4</sub></b>	650	33.05	32.98	0.1968	38.69	2.7101	2.7135	(222)
	750	33.04	32.98	0.1968	38.71	2.7091	2.7135	(222)
	850	33.07	32.98	0.1968	38.69	2.7083	2.7135	(222)
<b>Zn<sub>0.15</sub>Mn<sub>0.85</sub>Fe<sub>2</sub>O<sub>4</sub></b>	650	35.40	35.24	0.4904	15.43	2.5354	2.5441	(113)
	750	35.40	35.24	0.4436	17.06	2.5352	2.5441	(113)
	850	35.29	35.24	0.4152	18.23	2.5387	2.5441	(113)
<b>Zn<sub>0.25</sub>Mn<sub>0.75</sub>Fe<sub>2</sub>O<sub>4</sub></b>	650	35.28	35.24	0.3992	18.96	2.5276	2.5441	(113)
	750	35.27	35.24	0.39804	19.02	2.5372	2.5441	(113)
	850	35.25	35.24	0.3936	19.23	2.5313	2.5441	(113)
<b>Zn<sub>0.35</sub>Mn<sub>0.65</sub>Fe<sub>2</sub>O<sub>4</sub></b>	650	35.33	35.24	0.3936	19.23	2.5151	2.5441	(113)
	750	35.31	35.24	0.3741	20.24	2.5283	2.5441	(113)
	850	35.35	35.24	0.3444	21.97	2.5386	2.5441	(113)
<b>Zn<sub>0.45</sub>Mn<sub>0.55</sub>Fe<sub>2</sub>O<sub>4</sub></b>	650	35.27	35.24	0.2704	27.99	2.5443	2.5441	(113)
	750	35.27	35.24	0.2604	29.07	2.5443	2.5441	(113)
	850	35.27	35.24	0.2462	30.77	2.5376	2.5441	(113)

**Table (4.2): XRD calculations of  $Zn_{0.45}Mn_{0.55}Fe_2O_4$  mixed with different content of  $TiO_2$ .**

Material	TiO <sub>2</sub> content %	2 $\theta$ (deg) Practical	2 $\theta$ (deg) Standard	FWHM (deg)	Crystalline size (nm)	d <sub>hkl</sub> (°A) Practical	d <sub>hkl</sub> (°A) Standard	(hkl)
<b>Zn<sub>0.45</sub>Mn<sub>0.55</sub>Fe<sub>2</sub>O<sub>4</sub>/TiO<sub>2</sub></b>	20	35.27	35.24	0.2462	30.93	2.5376	2.5441	(113)
<b>Zn<sub>0.45</sub>Mn<sub>0.55</sub>Fe<sub>2</sub>O<sub>4</sub>/TiO<sub>2</sub></b>	30	35.26	35.24	0.2954	28.87	2.5347	2.5441	(113)
<b>Zn<sub>0.45</sub>Mn<sub>0.55</sub>Fe<sub>2</sub>O<sub>4</sub>/TiO<sub>2</sub></b>	40	35.28	35.24	0.2952	30.07	2.5401	2.5441	(113)
<b>Zn<sub>0.45</sub>Mn<sub>0.55</sub>Fe<sub>2</sub>O<sub>4</sub>/TiO<sub>2</sub></b>	50	25.45	25.42	0.3936	20.75	3.4992	3.5001	(011)
<b>Zn<sub>0.45</sub>Mn<sub>0.55</sub>Fe<sub>2</sub>O<sub>4</sub>/TiO<sub>2</sub></b>	60	25.35	25.42	0.2952	27.66	3.5129	3.5001	(011)
<b>TiO<sub>2</sub></b>	100	25.39	25.42	0.7200	10.76	3.5107	3.5001	(011)

### 4.2.2 Field Emission Scanning Electron Microscopy (FE-SEM) of ( $Zn_xMn_{1-x}Fe_2O_4$ )

The results of FE-SEM tests on the combination  $Zn_xMn_{1-x}Fe_2O_4$  revealed that the particles had a spherical shape with a limited distribution of nanoparticle sizes, suggesting that the particles were created and have porosity. We also see the fine spherical particles forming a homogenous agglomeration, since particles of smaller size have persistent magnetism, hence each particle has permanent magnetization as a result of particle agglomeration and grouping. Figures (4-7, 4-8, 4-9, 4-10, and 4-11) show the results of FE-SEM tests for values ( $x=0, 0.15, 0.25, 0.35, \text{ and } 0.45$ ) at temperatures (650, 750, and 850 °C), respectively, and show that particle size increases with increasing temperature across the forms. Table 4.3 shows the estimated diameters of  $Zn_xMn_{1-x}Fe_2O_4$  nanoparticles ( $x=0, 0.15, 0.25, 0.35, \text{ and } 0.45$ ) for calcined specimens at 650, 750, and 850 °C with relatively well-crystallized grains and a mean particle size lower than range from 25 to 66 nm respectively, measured by Image J Software (version 1.51j8; National Institutes of Health, Bethesda, USA).

The particle size determined by FE-SEM micrographs is found to be bigger than that determined using XRD data. The molecule structural disruption and lattice strain caused by variable ionic radii and/or nanoparticle collection might be attributed to the XRD technique. As a result, the requirements are more severe, resulting in smaller sizes [117].

The particle size got larger when the calcination temperature was raised, as shown in the FE-SEM image. FE-SEM images of manganese ferrite nanoparticles after calcination at 650, 750, and 850 °C, are shown in figures (4-7, 4-8, 4-9, 4-10, and 4-11). At 650 °C, spherical ferrite particles agglomerated and separated

significantly. At greater calcination temperatures, larger spherical and elongated particles were observed.

The particle size of calcined specimens rises as the concentration of (x) increases at 650, 750 °C, and 850 °C as shown in table (4-3). Each particle is magnetized all of the time due to its permanent magnetic moment and wants to cluster together. The magnetic moment of co-substituted nanoparticles is higher, resulting in increased clustering, the coalescence of adjacent grains is also observed due to its influence on temperature [118, 119].

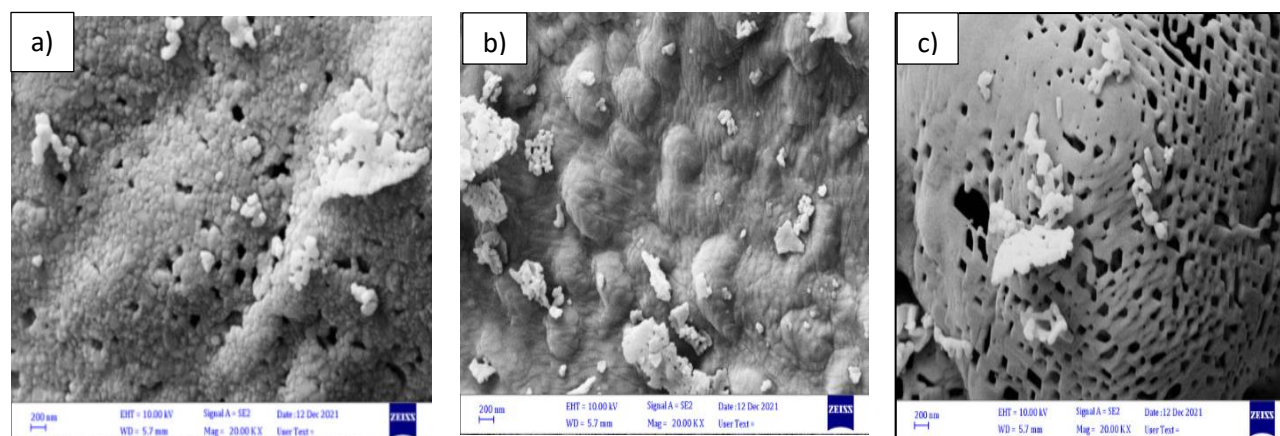


Figure (4.7): FE-SEM micrographs of MnFe<sub>2</sub>O<sub>4</sub> nano ferrites calcined (a) at 650 °C (b) at 750 °C and (c) at 850 °C.

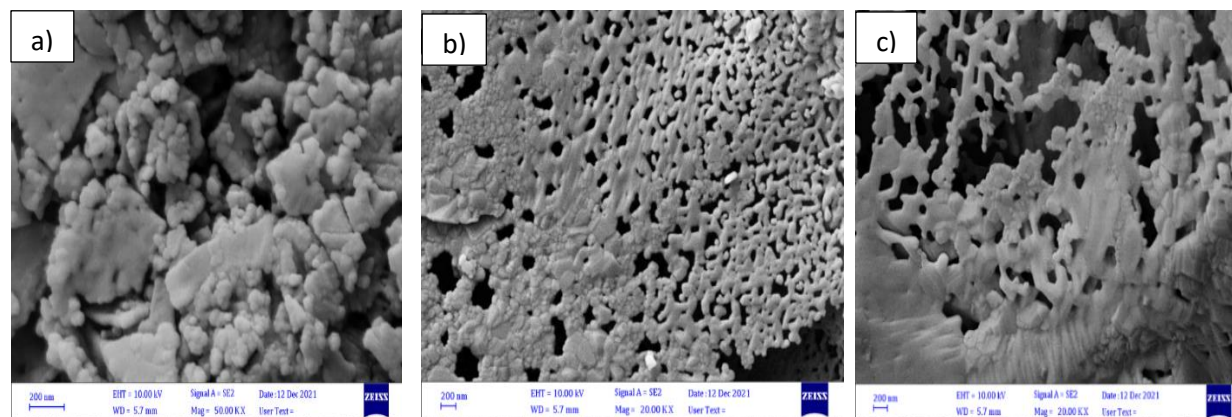


Figure (4.8): FE-SEM micrographs of Zn<sub>0.15</sub>Mn<sub>0.85</sub>Fe<sub>2</sub>O<sub>4</sub> nanoferrites calcined (a) at 650 °C (b) at 750 °C and (c) at 850 °C.

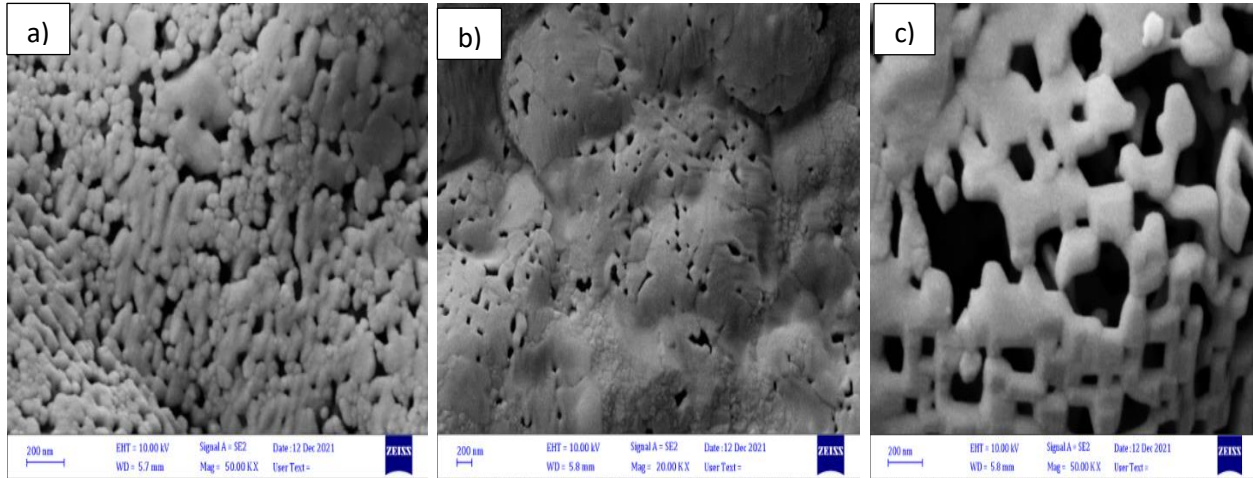


Figure (4.9): FE-SEM micrographs of  $\text{Zn}_{0.25}\text{Mn}_{0.75}\text{Fe}_2\text{O}_4$  nanoferrites calcined (a) at 650 °C (b) at 750 °C and (c) at 850 °C.

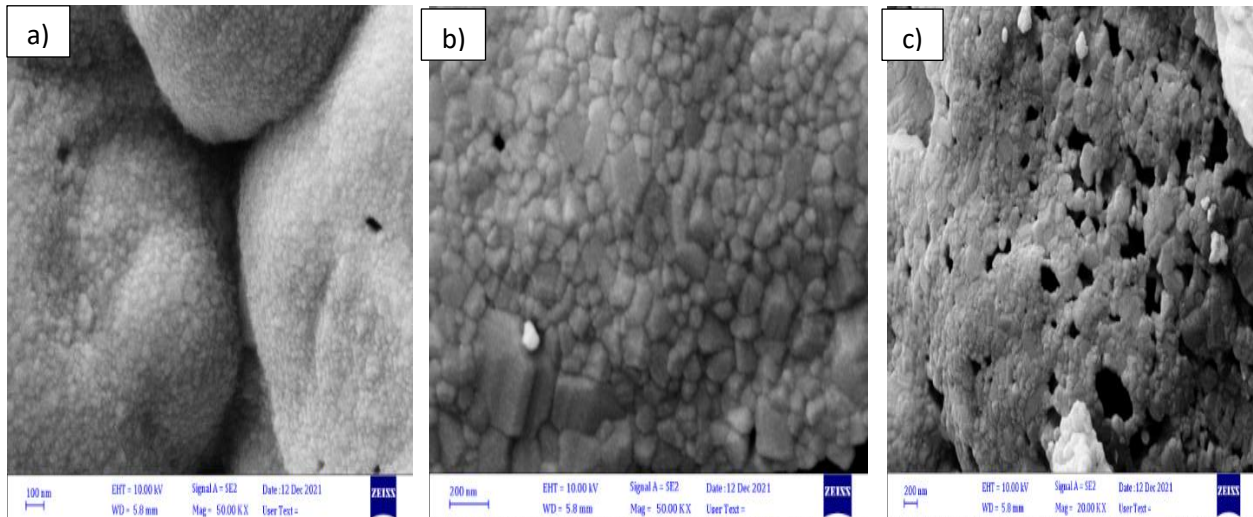


Figure (4.10): FE-SEM micrographs of  $\text{Zn}_{0.35}\text{Mn}_{0.65}\text{Fe}_2\text{O}_4$  nanoferrites calcined (a) at 650 °C (b) at 750 °C and (c) at 850 °C.

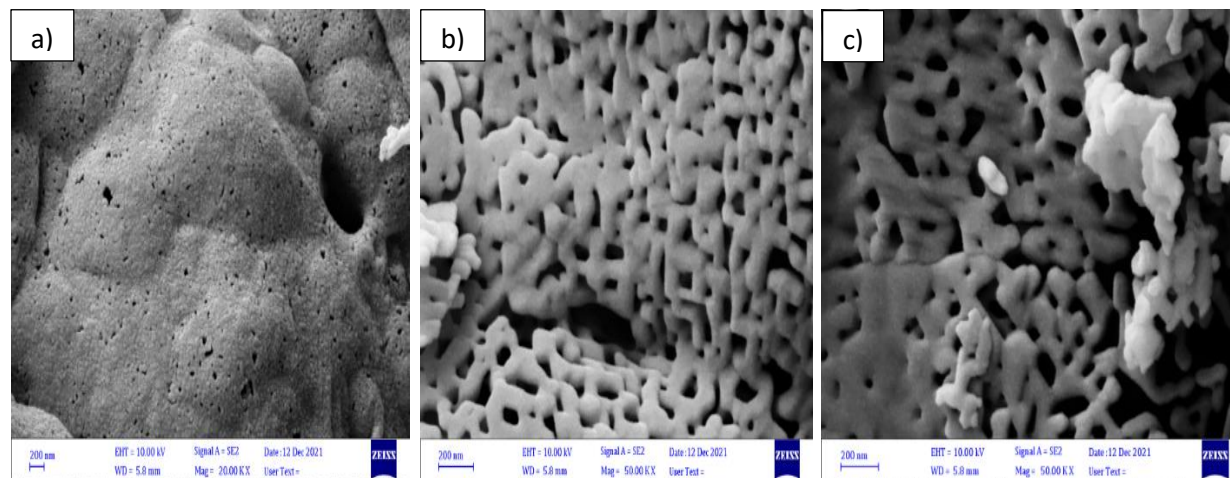


Figure (4.11): FE-SEM micrographs of  $\text{Zn}_{0.45}\text{Mn}_{0.55}\text{Fe}_2\text{O}_4$  nanoferrites calcined (a) at 650 °C (b) at 750 °C and (c) at 850 °C.

**Table (4.3):** Average crystallite size and particle size of  $\text{Zn}_x\text{Mn}_{1-x}\text{Fe}_2\text{O}_4$  nanoferrites ( $x = 0, 0.15, 0.25, 0.35,$  and  $0.45$ ) at different calcined temperatures which determined from XRD and FE-SEM data.

$x$	Composition	Temp. °C	Crystallite size	Particle size
			(nm) XRD	(nm) FE-SEM
0	$\text{MnFe}_2\text{O}_4$	650	38.69	<b>48.22</b>
		750	38.71	<b>52.21</b>
		850	38.69	<b>44.11</b>
0.15	$\text{Zn}_{0.15}\text{Mn}_{0.85}\text{Fe}_2\text{O}_4$	650	15.43	<b>63.86</b>
		750	17.06	<b>59.22</b>
		850	18.23	<b>66.54</b>
0.25	$\text{Zn}_{0.25}\text{Mn}_{0.75}\text{Fe}_2\text{O}_4$	650	18.96	<b>30.89</b>
		750	19.02	<b>33.65</b>
		850	19.23	<b>45.92</b>
		650	19.23	<b>25.31</b>

0.35	$Zn_{0.35}Mn_{0.65}Fe_2O_4$	750	20.24	<b>34.83</b>
		850	21.97	<b>27.76</b>
0.45	$Zn_{0.45}Mn_{0.55}Fe_2O_4$	650	27.99	<b>35.00</b>
		750	29.07	<b>36.01</b>
		850	30.77	<b>51.21</b>

### 4.2.3 Field Emission Scanning Electron Microscopy (FE-SEM) of $Zn_{0.45}Mn_{0.55}Fe_2O_4/TiO_2$

As shown in figures 4-12 (a-e), FE-SEM images were utilized to examine the surface morphology and the particle size of  $Zn_{0.45}Mn_{0.55}Fe_2O_4/TiO_2$  nanocomposites calcined at 500 °C. All of the specimens contain a compact order of homogenous nanoparticles with a spherical form and polyhedral particles. The estimated diameters of  $Zn_{0.45}Mn_{0.55}Fe_2O_4/TiO_2$  nanocomposites for calcined samples at 500 with relatively well-crystallized grains and average particle size less than (37.77, 43.60, 61.51, 47.29 and 72.04) nm, respectively calculated by Image J Software. It's also note the coalescence of adjacent grains with each other due to the increase in the concentration of  $TiO_2$ . The particle size measured using FE-SEM micrographs is larger than the XRD data estimates. The XRD method is responsible for the molecular structural disruption and lattice strain generated by differing ionic radii and/or nanoparticle collection. As a result, it has a more stringent requirement, which leads to lower sizes [120-121].

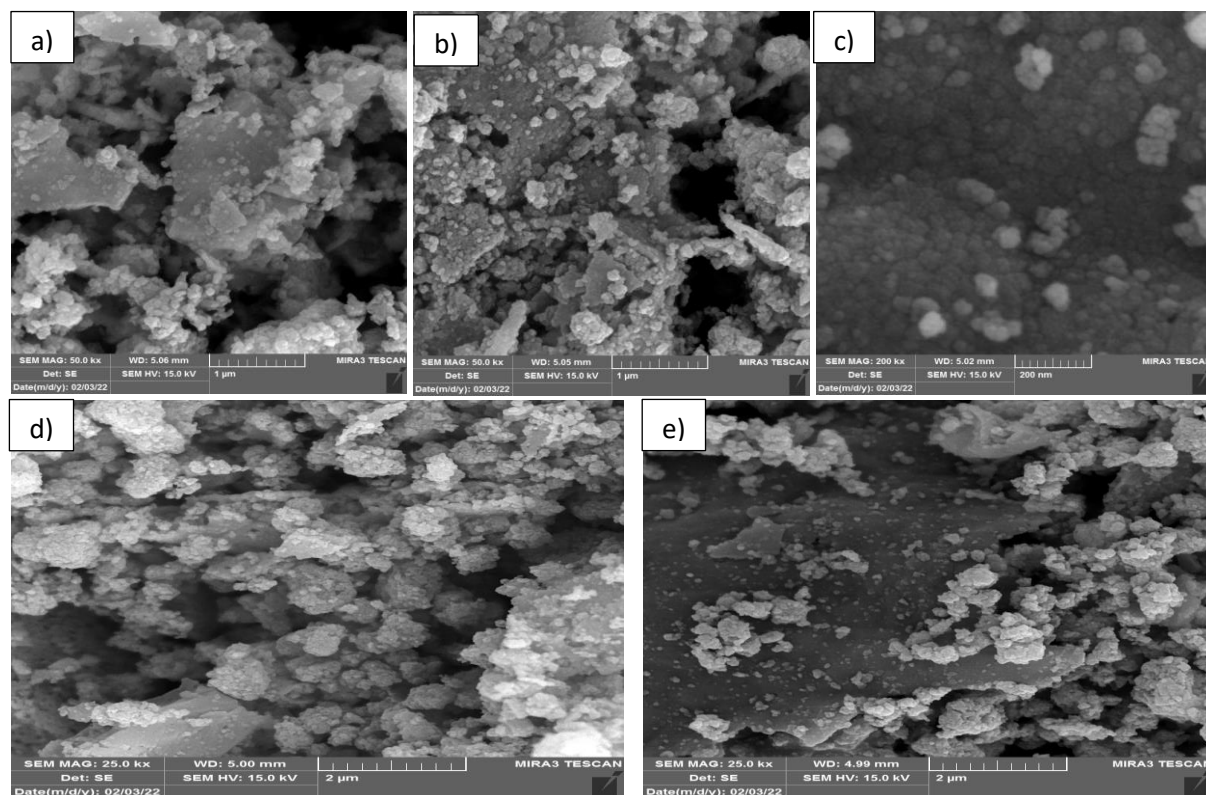
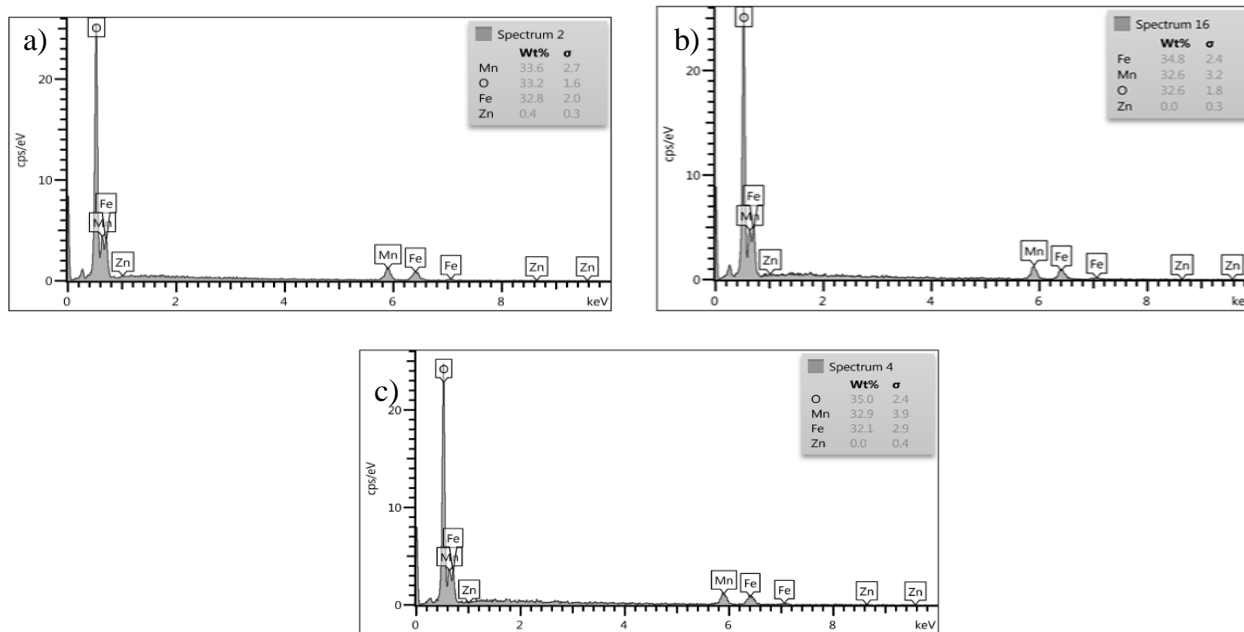


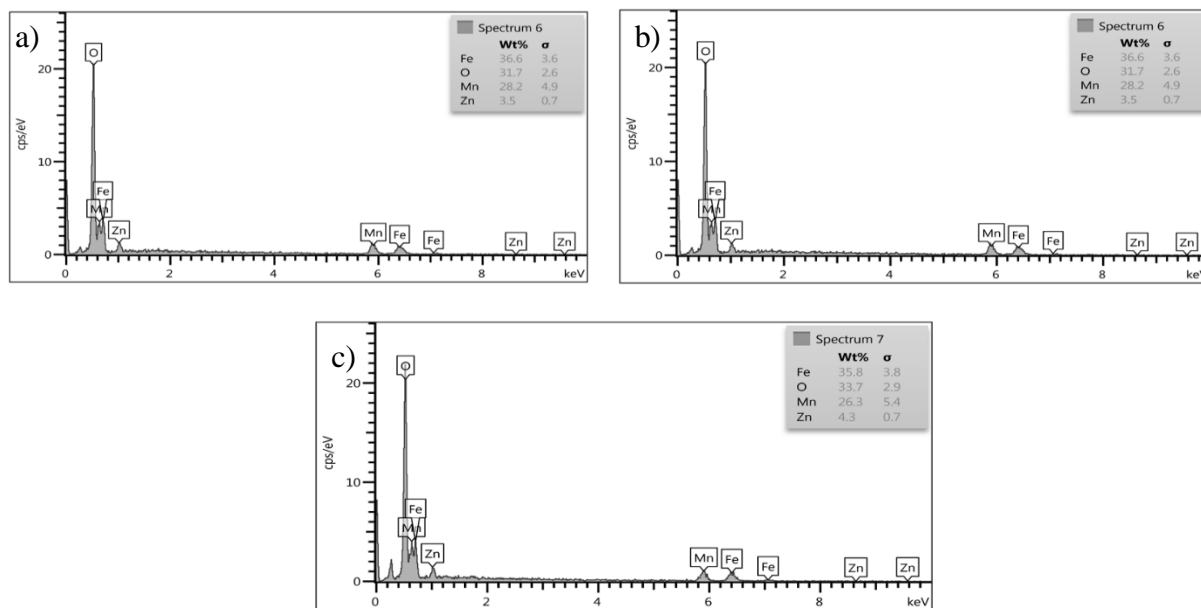
Figure (4.12): FE-SEM of (a), (b), (c), (d), and (e) for  $\text{Zn}_{0.45}\text{Mn}_{0.55}\text{Fe}_2\text{O}_4$  mixed with different ratios of  $\text{TiO}_2$  (20%, 30%, 40%, 50% and 60%) respectively.

#### 4.2.4 Energy Dispersive Spectroscopy (EDS) of ( $\text{Zn}_x\text{Mn}_{1-x}\text{Fe}_2\text{O}_4$ )

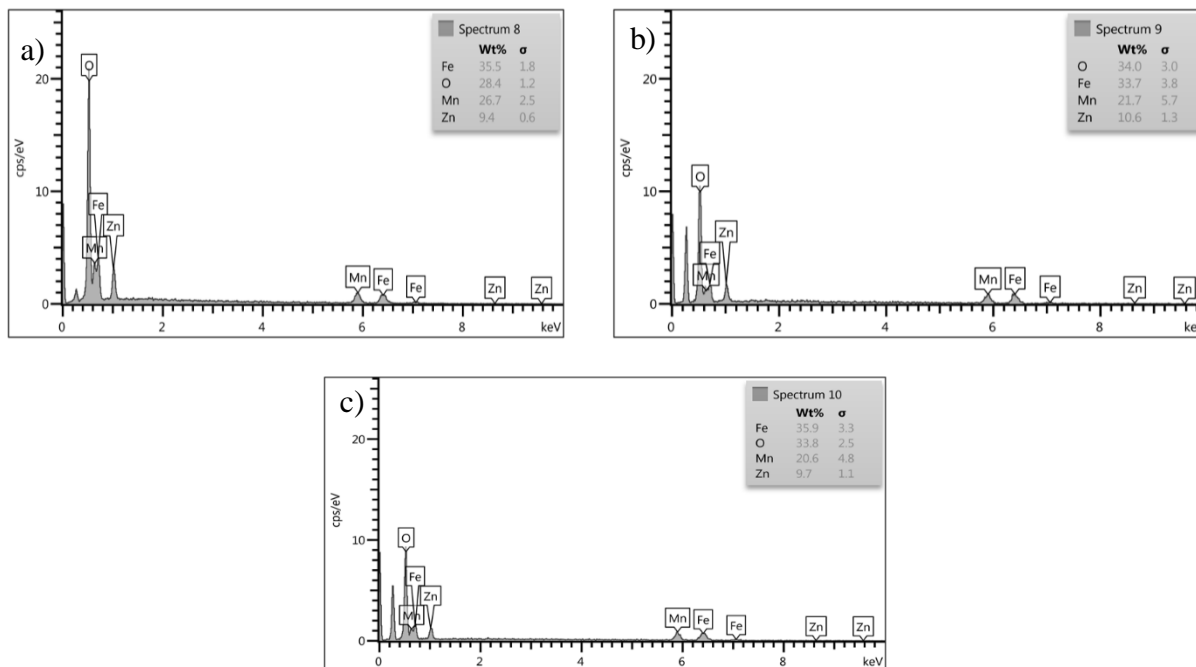
Figures (4-13 to 4-17) illustrate the EDS pattern of nanocrystalline  $\text{ZnMnFe}_2\text{O}_4$  ferrites ( $x= 0, 0.15, 0.25, 0.35,$  and  $0.45$ ) ferrites. The relative atomic abundance of Zn, Mn, Fe, and O species present in the upper surface layers of specimens in the absence of any contaminants. According to EDS analysis, as the content of ( $x$ ) increases, the iron element increases from 328.20 percent to 341.27 at 650 °C, reduces from 348.24 percent to 320.28 at 750 °C, and increases from 321.29 percent to 354.24 at 850 °C. As the concentration of ( $x$ ) increases, the manganese element drops from 336.27 percent to 169.42 percent at 650 °C, climbs from 326.32 to 339.37 at 750 °C, and drops from 329.39 percent to 187.37 at 850 °C [122].



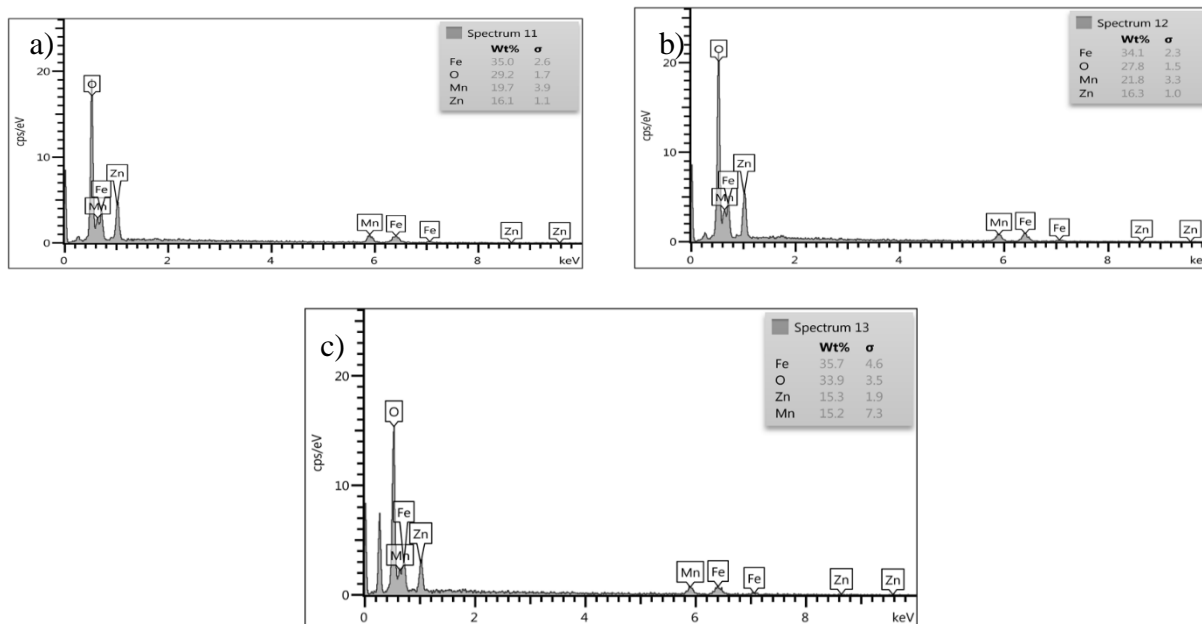
**Figure (4.13):** EDS spectra of  $\text{MnFe}_2\text{O}_4$  nanoferrites for samples (a) calcined at  $650\text{ }^\circ\text{C}$  (b) at  $750\text{ }^\circ\text{C}$  and (c) at  $850\text{ }^\circ\text{C}$ .



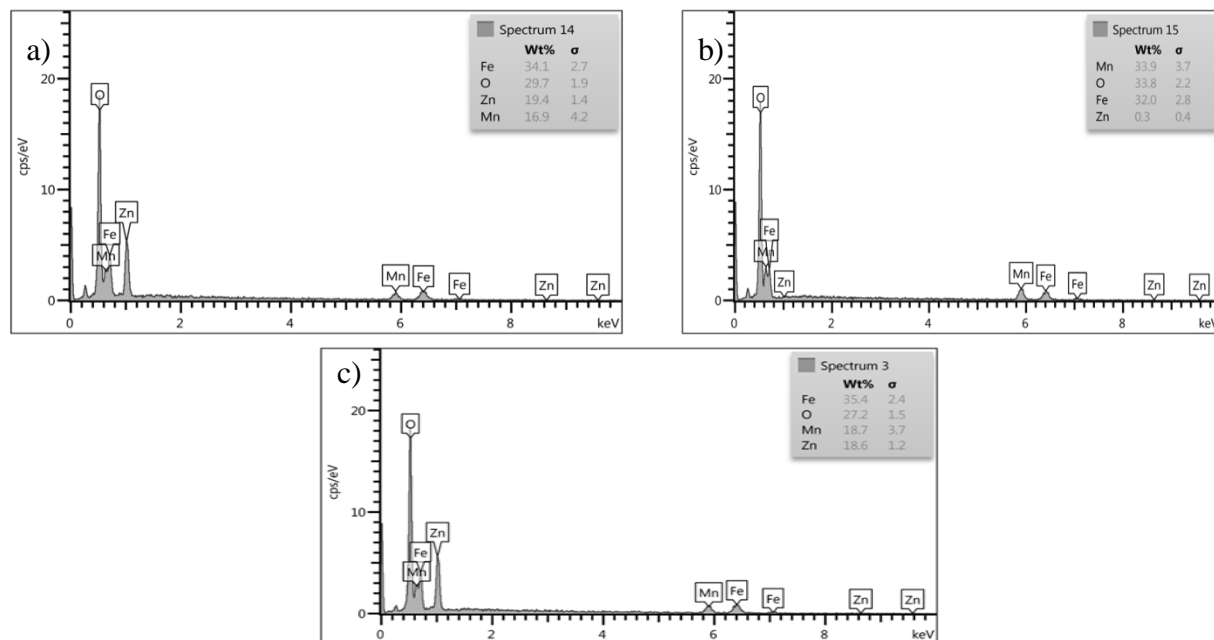
**Figure (4.14):** EDS spectra of  $\text{Zn}_{0.15}\text{Mn}_{0.85}\text{Fe}_2\text{O}_4$  nanoferrites for samples (a) calcined at  $650\text{ }^\circ\text{C}$  (b) at  $750\text{ }^\circ\text{C}$  and (c) at  $850\text{ }^\circ\text{C}$ .



**Figure (4.15):** EDS spectra of  $\text{Zn}_{0.25}\text{Mn}_{0.75}\text{Fe}_2\text{O}_4$  nano ferrites for samples (a) calcined at 650 °C (b) at 750 °C and (c) at 850 °C.



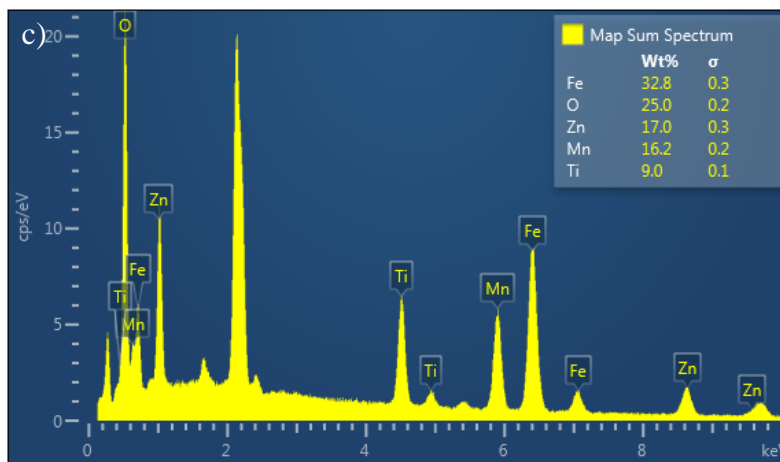
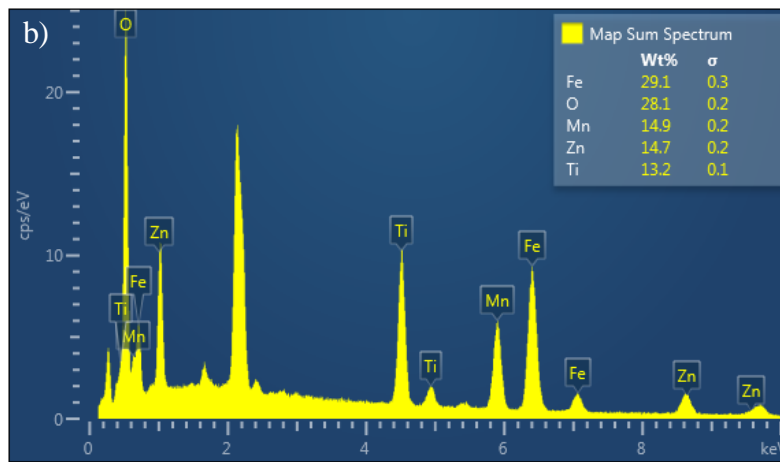
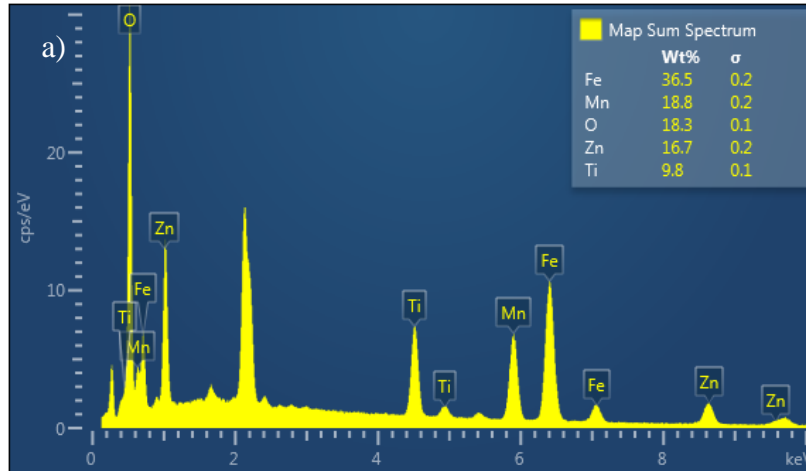
**Figure (4.16):** EDS spectra of  $\text{Zn}_{0.35}\text{Mn}_{0.65}\text{Fe}_2\text{O}_4$  nanoferrites for samples (a) calcined at 650 °C (b) at 750 °C and (c) at 850 °C.



**Figure (4.17):** EDS spectra of  $\text{Zn}_{0.45}\text{Mn}_{0.55}\text{Fe}_2\text{O}_4$  nanoferrites for samples (a) calcined at  $650\text{ }^\circ\text{C}$  (b) at  $750\text{ }^\circ\text{C}$  and (c) at  $850\text{ }^\circ\text{C}$ .

#### 4.2.5 Energy Dispersive Spectroscopy (EDS) of $\text{Zn}_{0.45}\text{Mn}_{0.55}\text{Fe}_2\text{O}_4/\text{TiO}_2$

Figures (4-18) show the EDS pattern of nanocrystalline  $\text{Zn}_x\text{Mn}_{1-x}\text{Fe}_2\text{O}_4$  ferrites ( $x=0.45$ ) ferrites with mixed the  $\text{TiO}_2$  NPs at different concentration (20%, 30%, 40%, 50%, and 60%). The relative atomic abundance of Zn, Mn, Fe, Ti and O species present in the upper surface layers of specimens in the absence of any contaminants. As shown in figure 4.18, the elemental compositions of nanoparticles were studied using an energy dispersive spectroscopy (EDS) method initiated by an electron beam (10 keV). EDS analysis confirms the presence of Zn, Mn, Fe, O, and Ti as major elements in the produced specimens. As the Ti mixing concentration rises, the peak of Ti appears to rise. The weight ratios of Zn, Mn, Fe, O, and Ti, as determined by EDS, as shown in figure 4.18 [123].



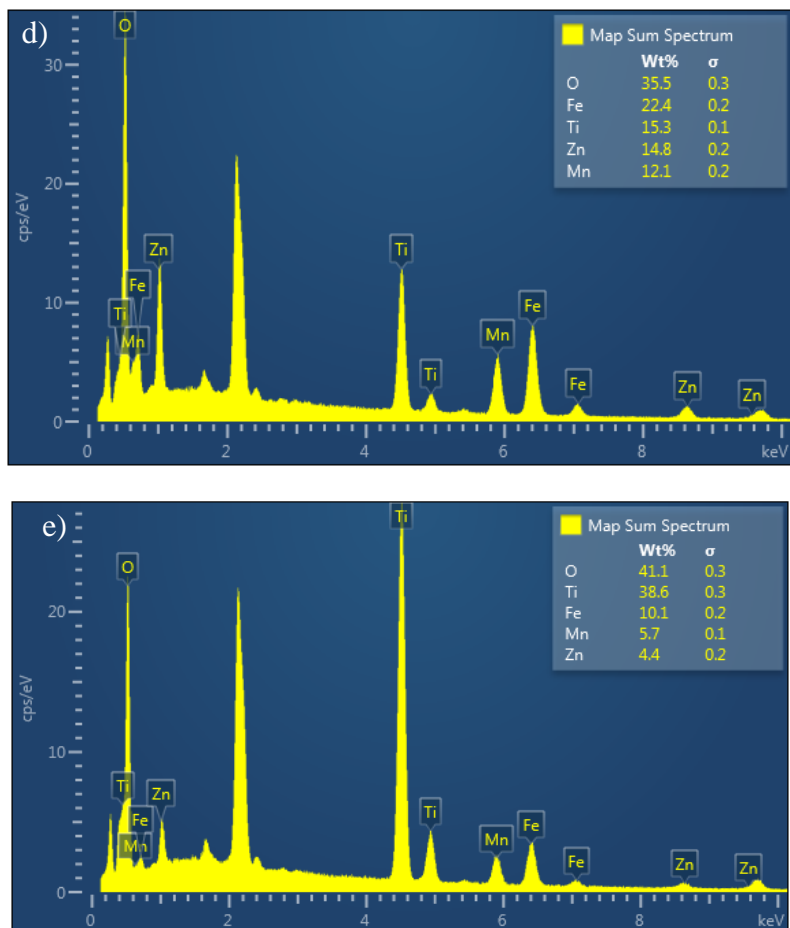


**Figure (4.18):** EDS spectra of  $\text{Zn}_{0.45}\text{Mn}_{0.55}\text{Fe}_2\text{O}_4$  nanoferrites mixed with different ratios of  $\text{TiO}_2$  (a) 20%, (b) 30%, (c) 40%, (d) 50%, (e) 60%.

#### 4.2.6 Fourier Transform Infrared (FT-IR) spectrum of $(\text{Zn}_x\text{Mn}_{1-x}\text{Fe}_2\text{O}_4)/\text{and } \text{Zn}_x\text{Mn}_{1-x}\text{Fe}_2\text{O}_4 / \text{TiO}_2$

The Functional Group Analysis, the absorption peak strong, and the compounds were determining by fourier transform infrared (FT-IR) spectrum of prepared  $\text{Zn}_x\text{Mn}_{1-x}\text{Fe}_2\text{O}_4$  ferrite ( $x = 0, 0.15, 0.25, 0.35$  and  $0.45$ ) at different calcination temperatures ( $650, 750$  and  $850$  °C). Figures (4-18, 4-19, 4-20, 4-21 and 4-22) present the FT-IR spectrum of pure  $\text{MnFe}_2\text{O}_4$  ferrite and doped with different concentrations of zinc metal  $\text{Zn}_x\text{Mn}_{1-x}\text{Fe}_2\text{O}_4$  ( $x= 0.15, 0.25, 0.35$  and  $0.45$ ) respectively, synthesized by sol-gel method.

MnFe<sub>2</sub>O<sub>4</sub> ferrite sample shown in figure (4-18) has a regular spinel MnFe<sub>2</sub>O<sub>4</sub> structure, which is supported by the FT-IR spectrum. An absorption broad band at 3480 cm<sup>-1</sup> (bending mode of H<sub>2</sub>O) showed that MnFe<sub>2</sub>O<sub>4</sub> nanoparticles have water molecules on their surfaces. It was found that stretching vibrations of C=C were the cause of the very weak band at 2334 cm<sup>-1</sup>, the existence of energy absorbance on the MnFe<sub>2</sub>O<sub>4</sub> nanoparticles' surfaces. At (465, 565), (444, 565) and (366, 478) cm<sup>-1</sup> of MnFe<sub>2</sub>O<sub>4</sub>, the strong peaks represent the Fe–O and Mn–O vibrations, respectively, of MnFe<sub>2</sub>O<sub>4</sub> structure at 650, 750, and 850 °C. It gets the peaks became more strong and pure with increasing the calcination temperature at 750 and 850 °C of MnFe<sub>2</sub>O<sub>4</sub> nanocomposite [124 - 125].

The FT-IR spectrum of Zn<sub>x</sub>Mn<sub>1-x</sub>Fe<sub>2</sub>O<sub>4</sub> ferrite nanocomposites at the concentrations (x= 0.15, 0.25 and 0.35), as shown in figures (4-19, 4-20 and 4-21), respectively. Analyses of 465-567-667, 1640 and 3420 cm<sup>-1</sup> show that there are multiple distinct peaks. Mn-O, Fe-O, and Zn-O bonds' vibrations in octahedral and tetrahedral sites are also characterized by peaks in the 465-567-667 cm<sup>-1</sup> frequency range. The FTIR data of the ferrite systems, which have a general spectrum at a frequency of roughly 400-600 cm<sup>-1</sup>, agrees well with these findings [126]. Another study found that the C=C bending was a significant contributor to the vibration at 2338, and 2934 cm<sup>-1</sup> [127].

Figure (4-22) shows the FT-IR spectra of Zn<sub>0.25</sub>Mn<sub>0.75</sub>Fe<sub>2</sub>O<sub>4</sub> ferrite nanocomposites. The asymmetric and symmetric C=O stretching modes are responsible for the bands at 1,516 and 1,600 cm<sup>-1</sup>, respectively, because metal ions coordinate the citric acid's carboxylate groups. The absorption peak at roughly 444, 567, and 665 cm<sup>-1</sup> was clearly proven to be caused by the stretching of Fe–O, and Mn–O, ZnO bonds [128 - 129].

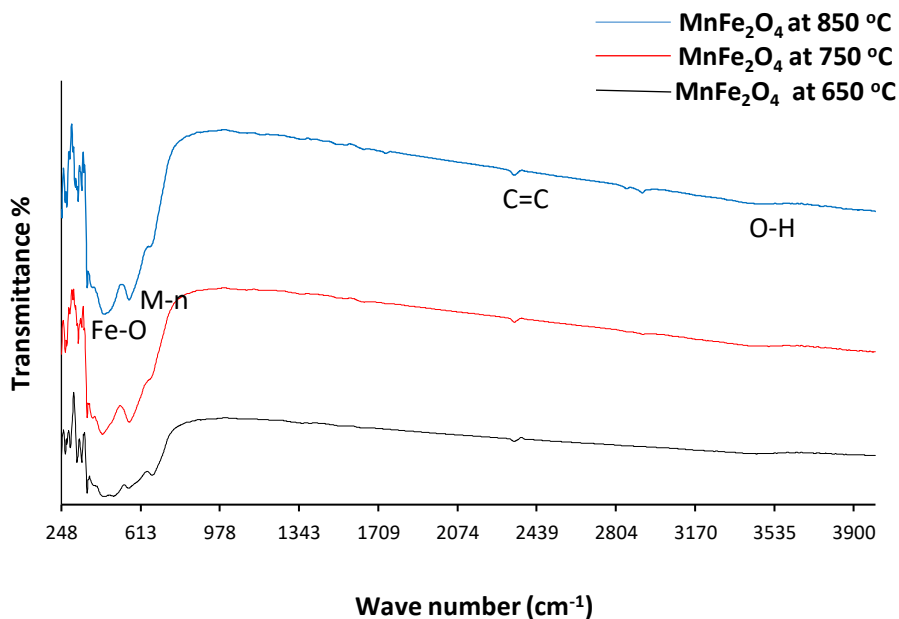


Figure (4.19): FT-IR spectrum of MnFe<sub>2</sub>O<sub>4</sub> ferrites prepared at different calcination temperatures (650, 750, and 850 °C) using sol-gel method.

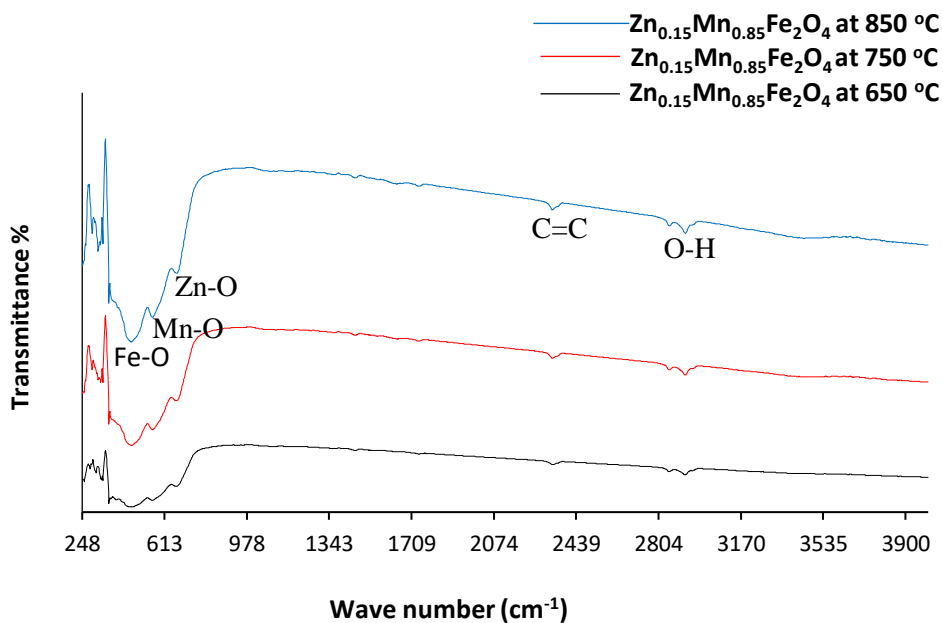


Figure (4.20): FT-IR spectrum of Zn<sub>0.15</sub>Mn<sub>0.85</sub>Fe<sub>2</sub>O<sub>4</sub> ferrites prepared at different calcination temperatures (650, 750, and 850 °C) using sol-gel method.

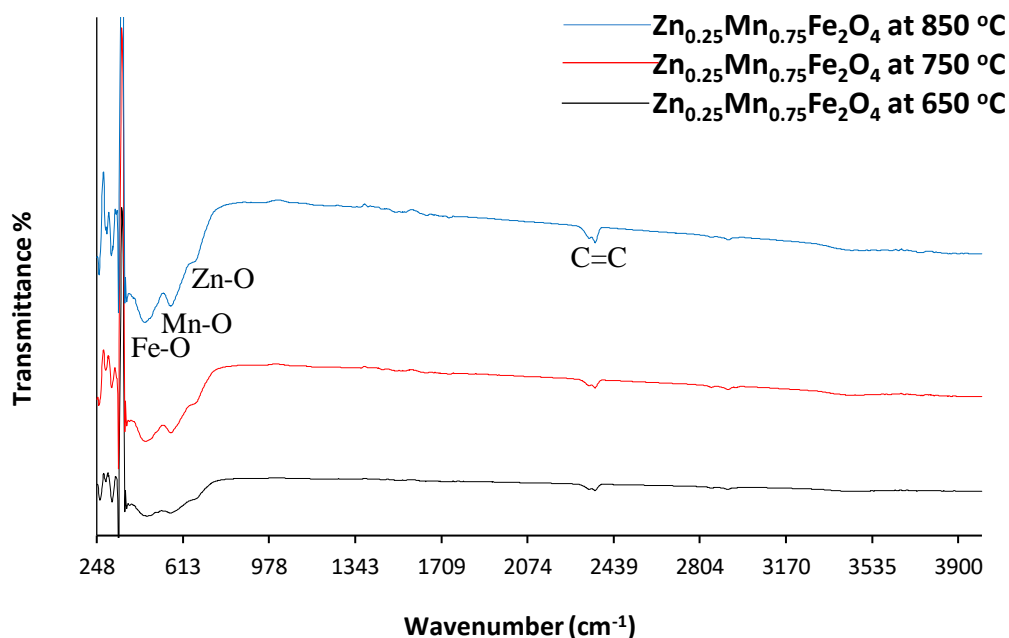


Figure (4.21): FT-IR of  $\text{Zn}_{0.25}\text{Mn}_{0.75}\text{Fe}_2\text{O}_4$  ferrite at different calcination temperatures (650, 750, and 850 °C) by sol-gel method.

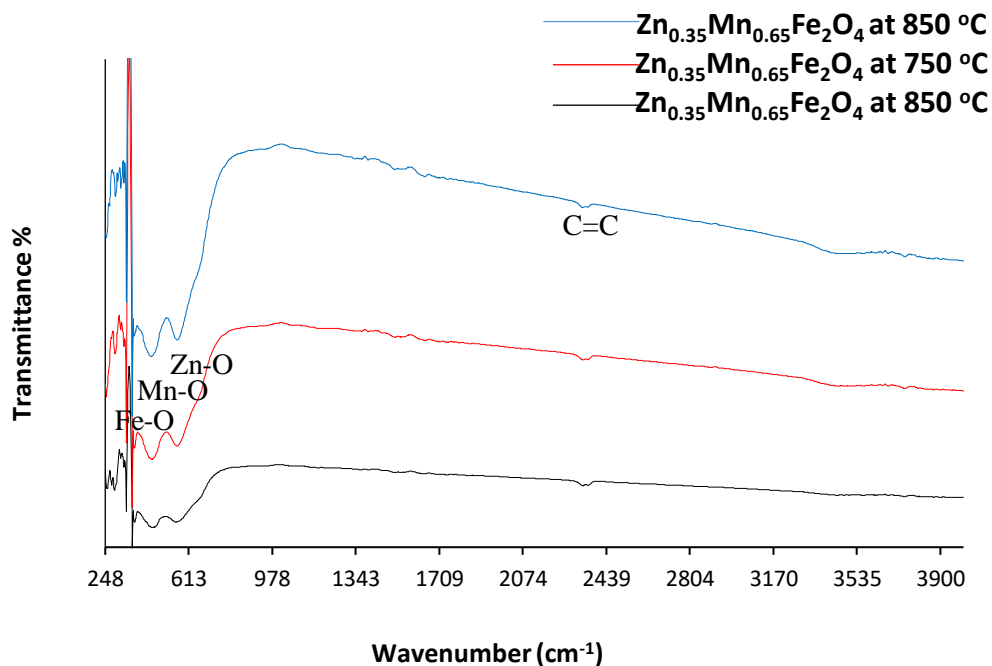


Figure (4.22): FT-IR spectrum of  $\text{Zn}_{0.35}\text{Mn}_{0.65}\text{Fe}_2\text{O}_4$  ferrites prepared at different calcination temperatures (650, 750, and 850 °C) using sol-gel method.

Analysis of the adsorbent's functional groups was carried out using the Fourier-transform infrared spectroscopy developed by BRUKER and the ALPHA model at a range of 400 to 3800  $\text{cm}^{-1}$ . Because each band belongs to a distinct group, the functional groups and the numbers assigned to them can be determined, as illustrated in figure (4-23) [130]. Figure (4-23) shows the FT-IR spectrum of pure  $\text{TiO}_2$  nanoparticles and  $\text{Zn}_{0.45}\text{Mn}_{0.55}\text{Fe}_2\text{O}_4$  mixed with different ratios (20%, 30, 40, 50, and 60 %) of  $\text{TiO}_2$  nanoparticles, which was calcined at 500  $^\circ\text{C}$  to study the produced  $\text{Zn}_{0.45}\text{Mn}_{0.55}\text{Fe}_2\text{O}_4$  ferrite nanocomposite. The peak at 1641  $\text{cm}^{-1}$ , 2344  $\text{cm}^{-1}$  is indicative of the bands in the  $\text{TiO}_2$  substance, whereas the peak at 500  $\text{cm}^{-1}$  to 600  $\text{cm}^{-1}$  is indicative of metal Fe-O, Mn-O and Zn-O bonds [131].

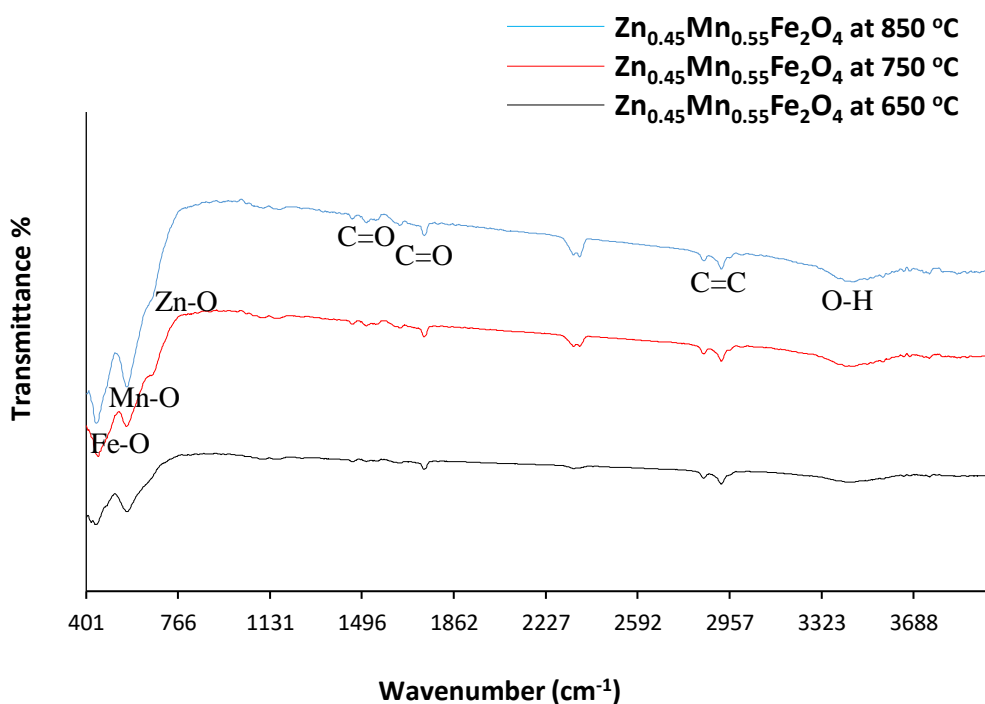


Figure (4.23): FT-IR spectrum of  $\text{Zn}_{0.45}\text{Mn}_{0.55}\text{Fe}_2\text{O}_4$  ferrites prepared at different calcination temperatures (650, 750, and 850  $^\circ\text{C}$ ) using sol-gel method.

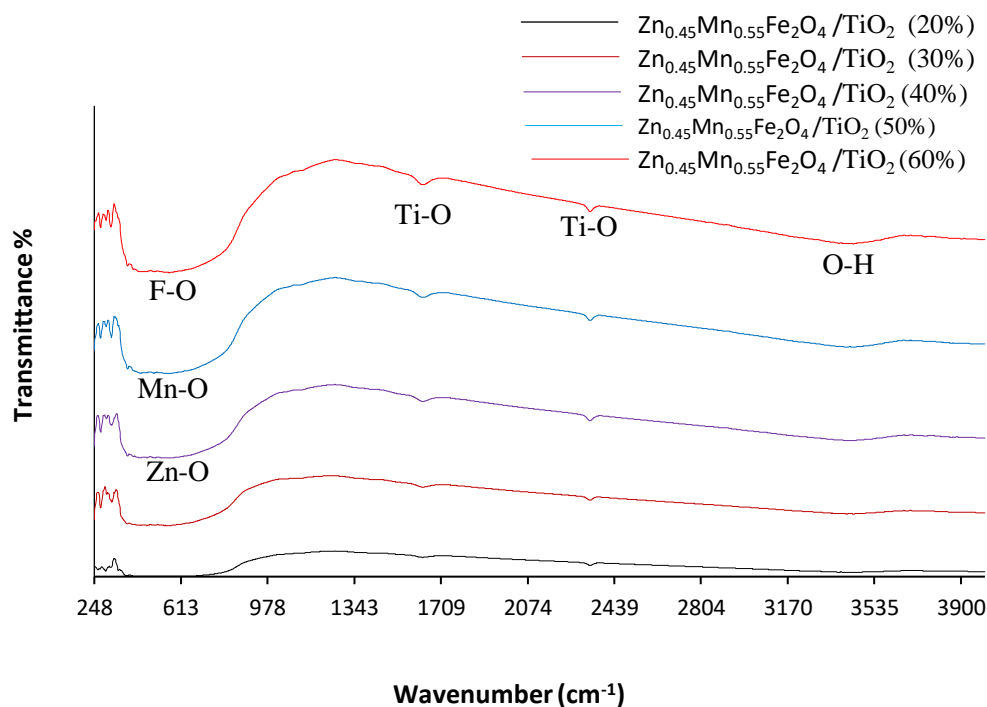


Figure (4.24): FTIR spectrum of  $\text{Zn}_{0.45}\text{Mn}_{0.55}\text{Fe}_2\text{O}_4$  mixed with different ratios of  $\text{TiO}_2$  (20%, 30%, 40%, 50% and 60%) respectively.

The absorption peaks strong of prepared  $\text{Zn}_{0.45}\text{Mn}_{0.55}\text{Fe}_2\text{O}_4$  at different calcination temperature was determined by the FT-IR spectrum peaks, to be (500 to 600  $\text{cm}^{-1}$ ) at the temperature (650, 750 and 850  $^{\circ}\text{C}$ ) respectively, as shown in table (4-4), and (4-5), which shows the FT-IR calculations of created  $\text{Zn}_x\text{Mn}_{1-x}\text{Fe}_2\text{O}_4$ . It gets that the crystalline size slightly increased with raising the calcination temperature and the zinc content which is the common behavior of all synthesized material, attributed to the appearance of the peak with increase the calcination temperature and the zinc content, and this is corresponded with the measured FT-IR spectrum [132-133].

**Table (4.4): FT-IR measurements of  $Zn_xMn_{1-x}Fe_2O_4$  with different content of zinc metal ( $x=0, 0.15, 0.25, 0.35$  and  $0.45$ ) at different calcination temperatures.**

Material	Temp. °C	The strong band ( $cm^{-1}$ )	Compounds types	Absorption regions
<b>MnFe<sub>2</sub>O<sub>4</sub></b>	650	444	Fe-O	fingerprint region
	750	565	Mn-O	fingerprint region
	850	478	Mn-O	fingerprint region
<b>Zn<sub>0.15</sub>Mn<sub>0.85</sub>Fe<sub>2</sub>O<sub>4</sub></b>	650	465	Fe-O	fingerprint region
	750	567	Mn-O	fingerprint region
	850	667	Zn-O	fingerprint region
<b>Zn<sub>0.25</sub>Mn<sub>0.75</sub>Fe<sub>2</sub>O<sub>4</sub></b>	650	465	Fe-O	fingerprint region
	750	567	Mn-O	fingerprint region
	850	667	Zn-O	fingerprint region
<b>Zn<sub>0.35</sub>Mn<sub>0.65</sub>Fe<sub>2</sub>O<sub>4</sub></b>	650	465	Fe-O	fingerprint region
	750	567	Mn-O	fingerprint region
	850	667	Zn-O	fingerprint region
<b>Zn<sub>0.45</sub>Mn<sub>0.55</sub>Fe<sub>2</sub>O<sub>4</sub></b>	650	444	Fe-O	fingerprint region
	750	567	Mn-O	fingerprint region
	850	665	Zn-O	fingerprint region

**Table (4.5): FT-IR measurements of  $Zn_{0.45}Mn_{0.55}Fe_2O_4$  mixed with different content of  $TiO_2$** 

Material	The strong band ( $cm^{-1}$ )	Compounds types	Absorption regions
$Zn_{0.45}Mn_{0.55}Fe_2O_4/TiO_2$ (20%)	500	Fe-O	fingerprint region
	550	Mn-O	fingerprint region
	600	Mn-O	fingerprint region
$Zn_{0.45}Mn_{0.55}Fe_2O_4/TiO_2$ (30%)	500	Fe-O	fingerprint region
	550	Mn-O	fingerprint region
	600	Zn-O	fingerprint region
$Zn_{0.45}Mn_{0.55}Fe_2O_4/TiO_2$ (40%)	500	Fe-O	fingerprint region
	550	Mn-O	fingerprint region
	600	Zn-O	fingerprint region
$Zn_{0.45}Mn_{0.55}Fe_2O_4/TiO_2$ (50%)	500	Fe-O	fingerprint region
	550	Mn-O	fingerprint region
	600	Zn-O	fingerprint region
$Zn_{0.45}Mn_{0.55}Fe_2O_4/TiO_2$ (60%)	1641	Ti-O	bending rocking
	1641	Ti-O	bending rocking
	1641	Ti-O	bending rocking

### 4.3 Magnetic Characterization

#### 4.3.1 Vibrating Sample Magnetometer (VSM) analysis of $(Zn_xMn_{1-x}Fe_2O_4)$ and $Zn_xMn_{1-x}Fe_2O_4 /TiO_2$

$Zn_xMn_{1-x}Fe_2O_4$  ferrite ( $x = 0, 0.15, 0.25, 0.35,$  and  $0.45$ ) were analyzed by VSM to determine the magnetization versus field  $M$  (H) at (650, 750, and 850 °C).

Figures (4-25, 4-26, 4-27, 4-28 and 4-29) show VSM analysis of pure  $\text{MnFe}_2\text{O}_4$  ferrite and doped with different concentrations of zinc metal  $\text{Zn}_x\text{Mn}_{1-x}\text{Fe}_2\text{O}_4$  ( $x=0.15, 0.25, 0.35, \text{ and } 0.45$ ) prepared by using sol-gel method. It was also possible to produce the hysteresis loop of the ( $\text{MnFe}_2\text{O}_4$ ) ferrite using VSM at 300 K by applying magnetic field from -15 to + 15 KOe to the material figure (4-25) (a-b). Using three different temperatures (650, 750, and 850 °C), it was observed that the saturation magnetization ( $M_s$ ) values were (0.81 emu/g, 9.39 emu/g, and 0.80 emu/g), respectively. This information is useful for recurrent magnetic separation. These results indicate that the prepared material exhibits diamagnetic (DM) behavior, as shown in figure 4-25 (a-b) and table (4-6). The values of remanence magnetization ( $M_s$ ) and coercivity ( $H_c$ ) were (17 Oe, 27 Oe, and 75 Oe), respectively, indicating that the prepared material exhibits diamagnetic behavior [134 - 135].

It has been observed that the magnetization is opposed to the applied magnetic field in the  $\text{MnFe}_2\text{O}_4$  ferrite indicating that these samples possess paramagnetic behavior [136]. The magnetic behavior of the  $\text{MnFe}_2\text{O}_4$  ferrite indicates that there is a mixture of diamagnetic (DM) and ferromagnetic (FM) phases, where the diamagnetic phase dominates. It is obvious that the saturation magnetization decrease rapidly with increasing the temperatures (750, and 850 °C) of samples, as shown in figure (4-25), indicating that the ferromagnetism arises rapidly [137].

In addition, the hysteresis loop of the ( $\text{Zn}_x\text{Mn}_{1-x}\text{Fe}_2\text{O}_4$ ) ferrite ( $x=0.15, 0.25, 0.35, \text{ and } 0.45$ ) was obtained using VSM at 29, 26, and 81 K by applying a magnetic field of between -15 and +15 KOe to it (Figure 4-25, 4-26, 4-27 and 4-28) and table (4-7, 4-8, 4-9 and 4-10). The saturation magnetization ( $M_s$ ) values were found to be (0.86 ,12.57, 3.1, and 8.159 emu/g) at (650 °C), (1.52, 3.3, and

0.789 emu/g) at (750 °C), and (1.37, 5.9, and 0.8 emu/g) at (850 °C), respectively, which is suitable for the repetitive magnetic separation of materials at high temperatures. This material exhibits super-paramagnetic behavior, as evidenced by its remanence magnetization ( $M_s$ ) and coercivity ( $H_c$ ) measurements of (17.5, 10, and 2.5 Oe) at (650 °C), (16.3, 17.5, and 80 Oe) at (750 °C), and (57, 31, and 95 Oe) at (850 °C) [138].

The magnetic characteristics of the produced samples have been evaluated at room temperature using a vibrating sample magnetometer (VSM) in the applied field ranging of  $-15$  to  $+15$  kOe. Hysteresis plots illustrating the variation of magnetization ( $M_s$ , emu/g) as a function of applied magnetic field ( $H$ , Oe) were plotted for produced nanocrystalline  $Mn_xZn_{1-x}Fe_2O_4$  ( $x = 0.15, 0.25, 0.35,$  and  $0.45$ ) powders are shown in figure (Figure 4-26, 4-27, 4-28 and 4-29) and table (4-7, 4-8, 4-9 and 4-10). Zn- $Fe_2O_4$  is a soft magnetic material, and when  $Zn^{2+}$  in Zn- $Fe_2O_4$  is substituted by  $Mn^{2+}$  ions, there is a severe change in the magnetic properties such saturation magnetization ( $M_s$ ), remanent magnetization ( $M_r$ ) and coercivity ( $H_c$ ) as illustrated in figure 4-27 (a–b). Until  $x = 0.15$ , the  $M_s$  of the  $Mn_xZn_{1-x}Fe_2O_4$  nanoparticles grew steadily with a rise in  $Mn^{2+}$  content; however, as the concentration of  $Mn^{2+}$  climbed above 0.15, the  $M_s$  decreased fast (as shown in 4-25, 4-26, 4-27, and 4-28). Because both  $Mn^{2+}$  and  $Zn^{2+}$  ions are non-magnetic, the  $M_s$  of  $Mn_xZn_{1-x}Fe_2O_4$  ferrite depends on the distribution of  $Fe^{3+}$  ions among the tetrahedral and octahedral lattice locations.

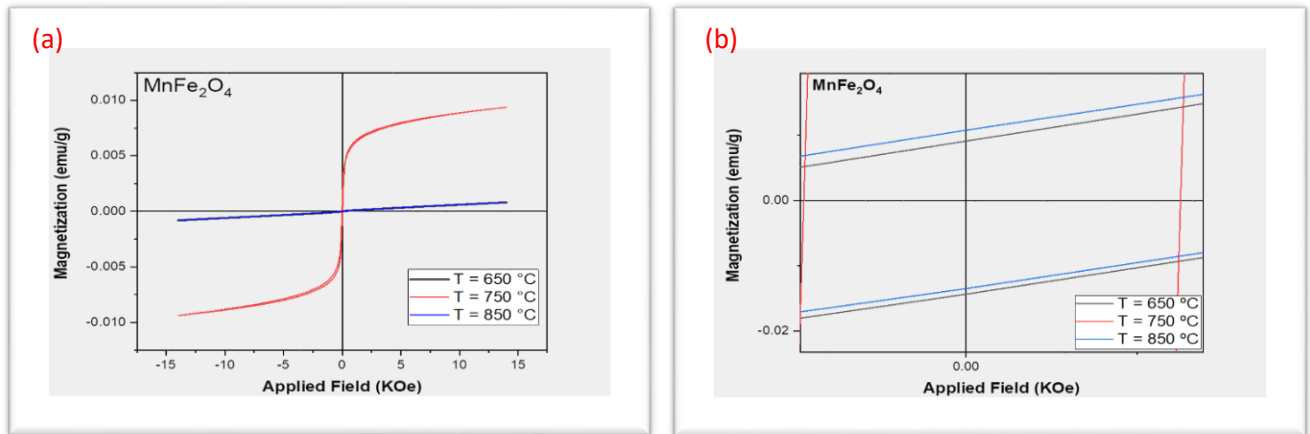


Figure (4.25) (a-b): VSM analysis of  $\text{MnFe}_2\text{O}_4$  ferrites calcined at different temperatures (650, 750, and 850 °C).

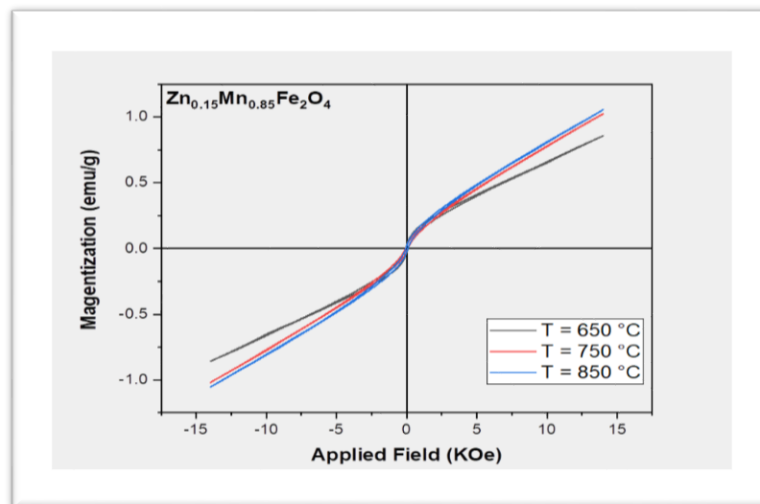


Figure (4.26): VSM analysis of  $\text{Zn}_{0.15}\text{Mn}_{0.85}\text{Fe}_2\text{O}_4$  ferrites calcined at different temperatures (650, 750, and 850 °C).

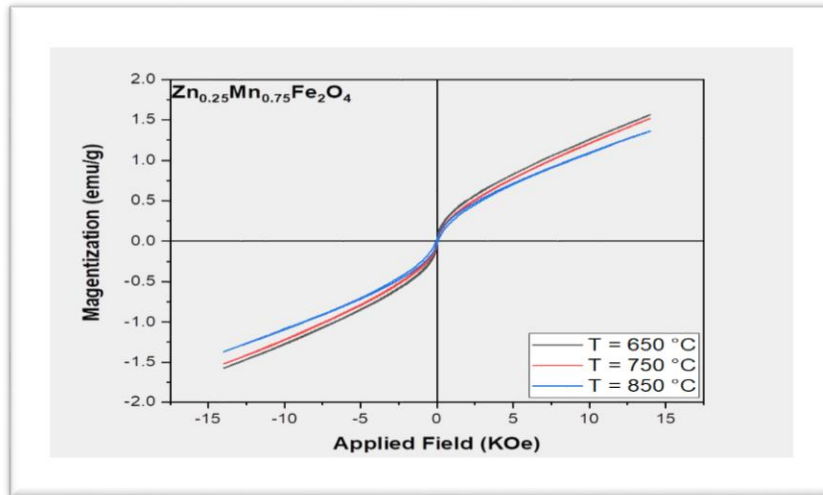


Figure (4.27): VSM analysis of  $\text{Zn}_{0.25}\text{Mn}_{0.75}\text{Fe}_2\text{O}_4$  ferrites calcined at different temperatures (650, 750, and 850 °C).

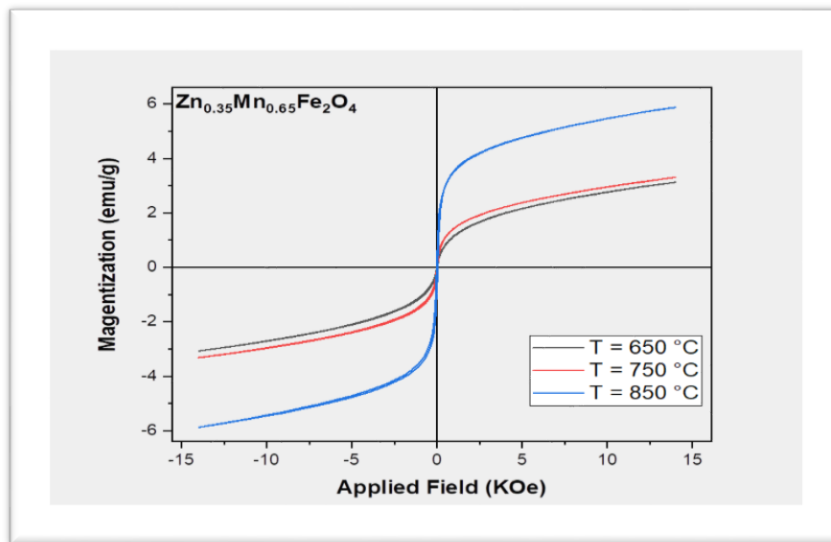


Figure (4.28): VSM analysis of  $\text{Zn}_{0.35}\text{Mn}_{0.65}\text{Fe}_2\text{O}_4$  ferrites calcined at different temperatures (650, 750, and 850 °C).

Because the  $\text{Zn}_{0.45}\text{Mn}_{0.55}\text{Fe}_2\text{O}_4$  ferrite was made, you need to look at it to see how it works. If you want to do this, you can look at Figure 4-28. It shows the

VSM analysis of  $\text{Zn}_{0.45}\text{Mn}_{0.55}\text{Fe}_2\text{O}_4$  mixed with different amounts of  $\text{TiO}_2$ . All of the samples had hard magnetic properties, which can be seen. Figure 4-30 also shows that the saturation magnetization ( $M_S$ ) and remanent magnetization ( $M_r$ ) of the ternary nano-hybrid increases with rarer earth ions (Ti) in it. The sample with the highest remanent and coercivity magnetizations was the one with the rarest earth ions in it. People who make zinc ferrites think that the terbium ions (Ti) will go into the octahedral spots because they are so big. Table 4-7 shows the coercivity, remanence, and saturation magnetization values of the samples that were used [139].

Using VSM at 28, 27, 23, 4 and 6 ( $\text{emu}\cdot\text{Oe}\cdot\text{g}^{-1}$ ) K, a hysteresis loop of the ( $\text{Zn}_x\text{Mn}_{1-x}\text{Fe}_2\text{O}_4$  ferrite) ( $x=0, 0.15, 0.25, 0.35, 0.45$ )  $\text{TiO}_2$  mixed with different ratios (20%, 30%, 40%, 50% and 60%) of  $\text{TiO}_2$  nanoparticles was achieved by applying a magnetic field of between -15 and +15 KOe to it figure (4-30). Using these saturation magnetization ( $M_s$ ) values, it was possible to repeatedly separate materials at high temperatures of (650 °C), (750 °C), and (850 °C), with  $M_s$  values of (4.7), (4.05), (3.7), (0.84), and (0.73)  $\text{emu/g}$ . Measurements of its remanence magnetization ( $M_s$ ) and coercivity ( $H_c$ ) is (5.75), (6.5), (6), (95), and (8) show that this material is super-paramagnetic [139].

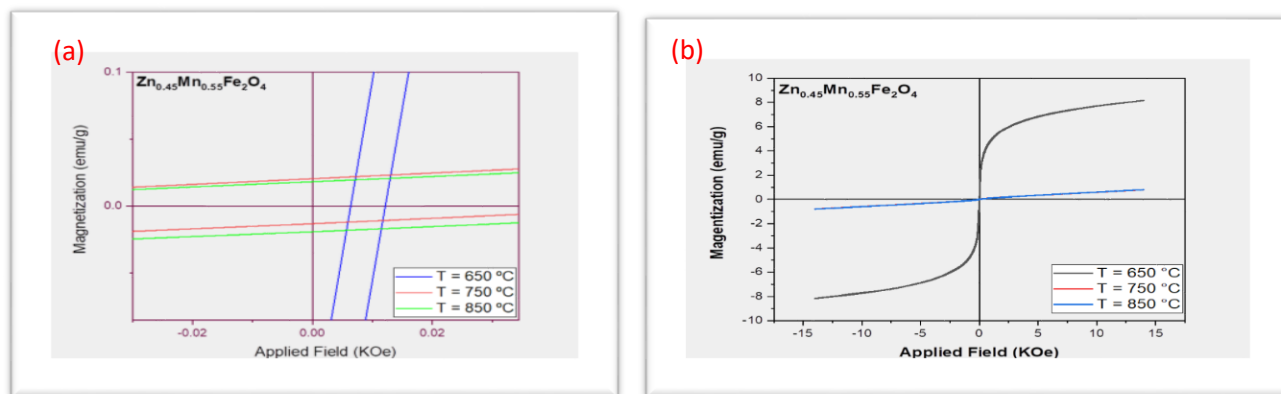


Figure (4.29) (a-b): VSM analysis of  $\text{Zn}_{0.45}\text{Mn}_{0.55}\text{Fe}_2\text{O}_4$  ferrites nano composites calcined at different temperatures (650, 750, and 850 °C).

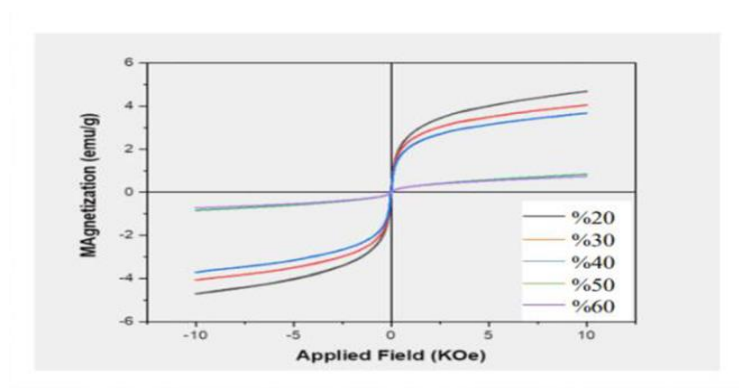


Figure (4.30): VSM analysis of (a)  $\text{Zn}_{0.45}\text{Mn}_{0.55}\text{Fe}_2\text{O}_4$  mixed with different ratios of  $\text{TiO}_2$  (20, 30, 40, 50 and 60%) respectively.

Table (4.6): VSM measurements of  $\text{MnFe}_2\text{O}_4$  calcined at different temperatures (650, 750, and 860) °C.

Temp	Hc (Oe)	Mr (emu/g)	Ms (emu/g)	Mr/Ms	nB ( $\mu_B$ )	K (emu.Oe.g <sup>-1</sup> )
650	17	0.01	0.81	0.0218	0.029	60
750	27	0.95	9.39	0.1012	0.334	26
850	75	0.02	0.80	0.0286	0.029	63

Table (4.7): VSM measurements of  $Zn_{0.15}Mn_{0.85}Fe_2O_4$  mixed with different content of zinc metal and calcined at different temperatures (650, 750, and 860) °C.

Temp	Hc (Oe)	Mr (emu/g)	Ms (emu/g)	Mr/Ms	nB ( $\mu_B$ )	K (emu.Oe.g <sup>-1</sup> )
650	100	0.03	0.86	0.0350	0.0310	89
750	75	0.02	1.02	0.0196	0.0365	80
850	70	0.02	1.06	0.0190	0.0379	77

Table (4.8): VSM measurements of  $Zn_{0.25}Mn_{0.85}Fe_2O_4$  mixed with different content of zinc metal and calcined at different temperatures (650, 750, and 860) °C.

Temp	Hc (Oe)	Mr (emu/g)	Ms (emu/g)	Mr/Ms	nB ( $\mu_B$ )	K (emu.Oe.g <sup>-1</sup> )
650	17.5	0.022	12.57	0.0018	0.057	29
750	16.3	0.015	1.52	0.0095	0.055	26
850	57	0.030	1.37	0.0220	0.049	81

Table (4.9): VSM measurements of  $Zn_{0.35}Mn_{0.75}Fe_2O_4$  mixed with different content of zinc metal and calcined at different temperatures (650, 750, and 860) °C.

Temp	Hc (Oe)	Mr (emu/g)	Ms (emu/g)	Mr/Ms	nB ( $\mu_B$ )	K (emu.Oe.g <sup>-1</sup> )
650	10	0.034	3.1	0.0109	0.1123	32
750	17.5	0.103	3.3	0.0311	0.12	61
850	31	0.600	5.9	0.1020	0.213	190

Table (4.10): VSM measurements of  $Zn_{0.45}Mn_{0.55}Fe_2O_4$  mixed with different content of zinc metal and calcined at different temperatures (650, 750, and 860) °C.

Temp	Hc (Oe)	Mr (emu/g)	Ms (emu/g)	Mr/Ms	nB ( $\mu_B$ )	K (emu.Oe.g <sup>-1</sup> )
650	2.5	0.073	8.159	0.0090	0.297	21
750	80	0.017	0.789	0.0215	0.0287	66
850	95	0.019	0.8	0.0238	0.029	79

Table (4.11): VSM measurements of  $Zn_{0.45}Mn_{0.55}Fe_2O_4$  mixed with different content of  $TiO_2$ .

Sample	Hc (Oe)	Mr (emu/g)	Ms (emu/g)	Mr/Ms	nB ( $\mu$ B)	K (emu.Oe.g <sup>-1</sup> )
20%	5.75	0.07	4.7	0.015	0.15	28
30%	6.5	0.086	4.05	0.020	0.12	27
40%	6	0.06	3.7	0.016	0.10	23
50%	5	0.004	0.84	0.005	0.02	4
60%	8	0.01	0.73	0.013	0.017	6

## 4.4 Electrical Characterization

### 4.4.1 Electrical Properties of $(Zn_xMn_{1-x}Fe_2O_4)$ and $Zn_xMn_{1-x}Fe_2O_4/TiO_2$

#### 4.4.1.1 Dielectric constant

The LCR meter carried out to investigate the values of different dielectric parameters such as the dielectric constant ( $\epsilon'$ ), the loss factor ( $\epsilon''$ ), the dielectric loss tangent  $\tan \delta$  and  $\sigma_{ac}$  of prepared  $Zn_xMn_{1-x}Fe_2O_4$  ferrite ( $x = 0, 0.15, 0.25, 0.35$  and  $0.45$ ) at different calcination temperatures at (400, 600 and 800 °C).

The frequency dependent dielectric characteristics of  $(MnFe_2O_4)$  ferrite were examined at varied operating temperatures at (400, 600 and 800 °C) in frequency range from 200 KHz to 2 MHz. The change in the values of different dielectric characteristics such as  $\epsilon'$ ,  $\epsilon''$ ,  $\tan \delta$  and  $\sigma_{ac}$  by increasing the temperatures of  $MnFe_2O_4$  nanoparticles at (400, 600 and 800 °C), were determined, compared and explained. When the sample is subjected to the external applied electric AC-field, the energy stored in the sample is represented by the real part of the dielectric constant ( $\epsilon'$ ). Koop's theory and Maxwell–Wagner model were utilized to describe the dielectric phenomenon in ferrites as well as in ferrites at various applied frequencies, as shown in figure (4-31) and table (4-12). For various applied frequencies, Koop's theory and the Maxwell–Wagner model were utilized to

explain the dielectric phenomena in ferrites [140]. In accordance with Koop's idea, a dielectric material is made up of conducting grains and non-conducting grain-boundary regions. Electrons can hop over grain boundaries in the presence of an external applied field. There are fewer electrons that can travel from the grains to the grain borders as the frequency increases [141].

$Zn_xMn_{1-x}Fe_2O_4$  ferrite at concentrations ( $x= 0.15, 0.25, 0.35,$  and  $0.45$ ) are shown in figures (4-32, 4-33, 4-34 and 4-35) and Table (4-13, 4-14, 4-15 and 4-16) accordingly. Figures (4-32, 4-33, 4-34 and 4-35) show the temperature dependence of the dielectric constant ( $\epsilon'$ ) for  $Zn_xMn_{1-x}Fe_2O_4$  ferrite at four fixed frequencies (200 KHz, 500 kHz, 1 MHz, 1.5 MHz and 2 MHz). The ( $\epsilon'$ ) increases with temperature at all frequencies, as can be seen in the figure (4-33, and 4-34). A rise in dielectric constant and loss as a function of rising temperature [142]. There are four distinct ways in which the dielectric constant of ferrite material can be attributed: interfacial, dipolar, electronic and ionic. Low-frequency polarizations, such as interfacial and dipolar, are very temperature dependent. The buildup of charge carriers at the grain boundary causes interfacial polarization. Charge carriers (electrons and holes) become more thermally activated and wander faster when the temperature rises. A rise in dielectric constant with rising temperature is a result of the increased electron hopping caused by this [143]. For the purpose of studying the  $Zn_{0.45}Mn_{0.55}Fe_2O_4$  ferrite nanocomposite calcined at 500 °C, Figure 4-35 shows the electric properties of pure  $TiO_2$  nanoparticles and  $Zn_{0.45}Mn_{0.55}Fe_2O_4$  combined with different  $TiO_2$  nanoparticle ratios (20%, 30%, 40%, 50%, and 60 %). Figure 4-36 depicts the variation of dielectric constant ( $\epsilon'$ ) at room temperature for all samples. Low frequency ( $\epsilon'$ ) measurements showed larger values due to the existence of space charge, dipolar and ionic as well as electronic polarizations. When  $TiO_2$  was doped with  $Zn_{0.45}Mn_{0.55}Fe_2O_4$ , the dielectric constant dropped due

to interfacial charge transfer at room temperature in the low-frequency zone. With Zn substitution, a rapid drop in dielectric constant ( $\epsilon'$ ) was seen in the low-frequency zone because of a smaller grain size and an entirely different polarization process. There are three factors that contribute to the polarization of nanomaterials: charge transfer between localized states, dipole displacement in response to applied fields, and space charge polarization. According to Koops, grain boundaries have a greater impact at lower frequencies. Thickness of  $\text{TiO}_2$  grain boundaries decreases the polarization and dielectric constant ( $\epsilon'$ ) of  $\text{Zn}_{0.45}\text{Mn}_{0.55}\text{Fe}_2\text{O}_4$  loaded onto  $\text{TiO}_2$ , as demonstrated in figure (4-36) and table (4-17) [144].

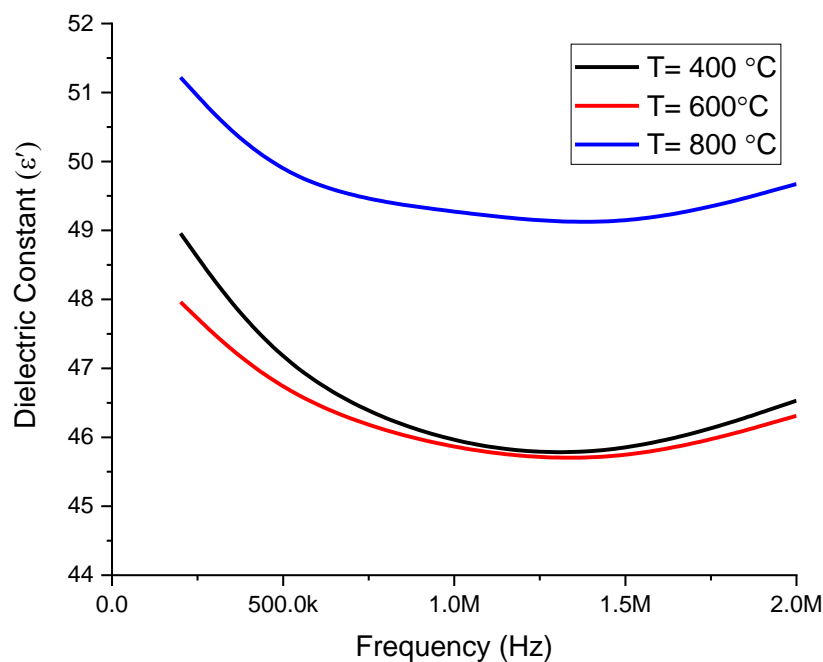


Figure (4.31): Frequency dependence of real part ( $\epsilon'$ ) of  $\text{MnFe}_2\text{O}_4$  ferrite at different calcination temperatures (400, 600, and 800  $^\circ\text{C}$ ).

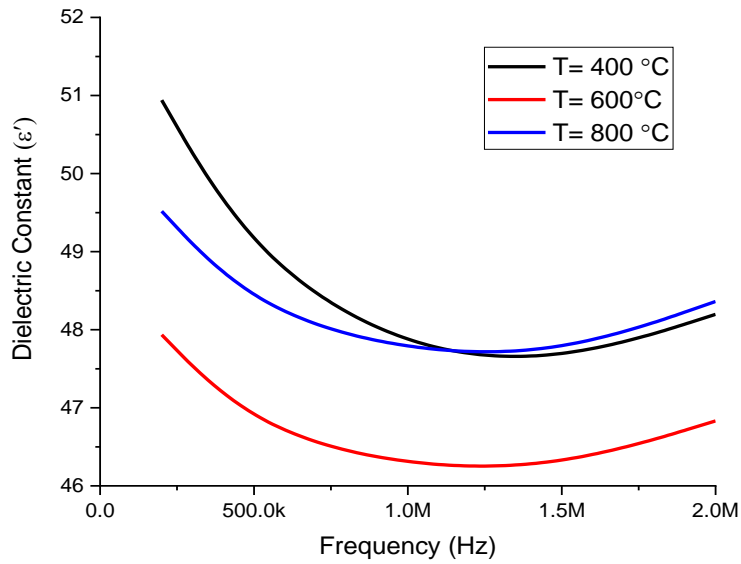


Figure (4.32): Frequency dependence of real part ( $\epsilon'$ ) of  $\text{Zn}_{0.15}\text{Mn}_{0.85}\text{Fe}_2\text{O}_4$  ferrite calcined at different temperatures (400, 600, and 800 °C).

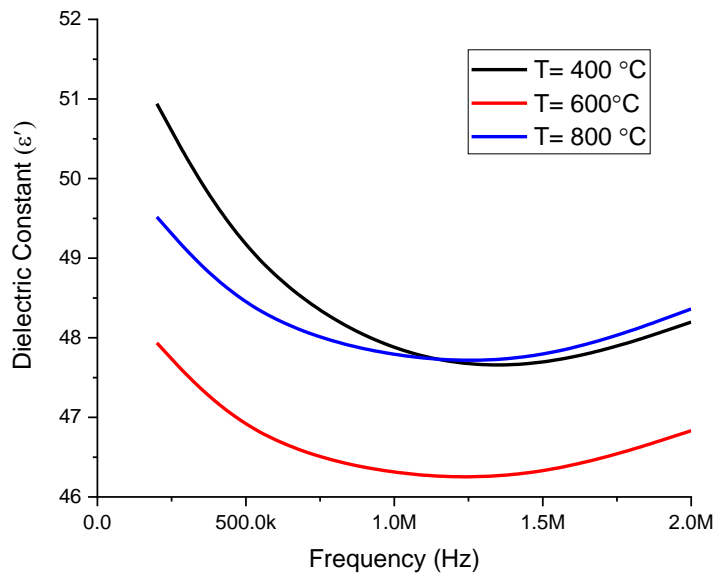


Figure (4.33): Frequency dependence of real part ( $\epsilon'$ ) of  $\text{Zn}_{0.25}\text{Mn}_{0.75}\text{Fe}_2\text{O}_4$  ferrite calcined at different temperatures (400, 600, and 800 °C).

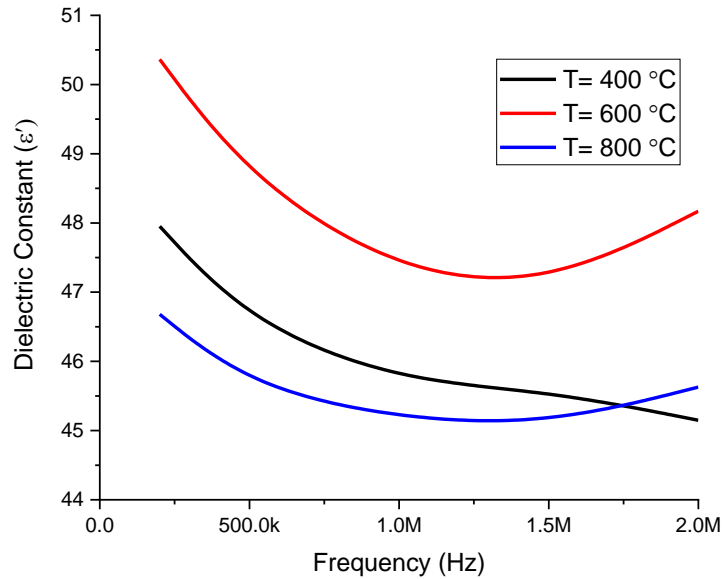


Figure (4.34): Frequency dependence of real part ( $\epsilon'$ ) of  $\text{Zn}_{0.35}\text{Mn}_{0.65}\text{Fe}_2\text{O}_4$  ferrite calcined at different temperatures (400, 600, and 800 °C).

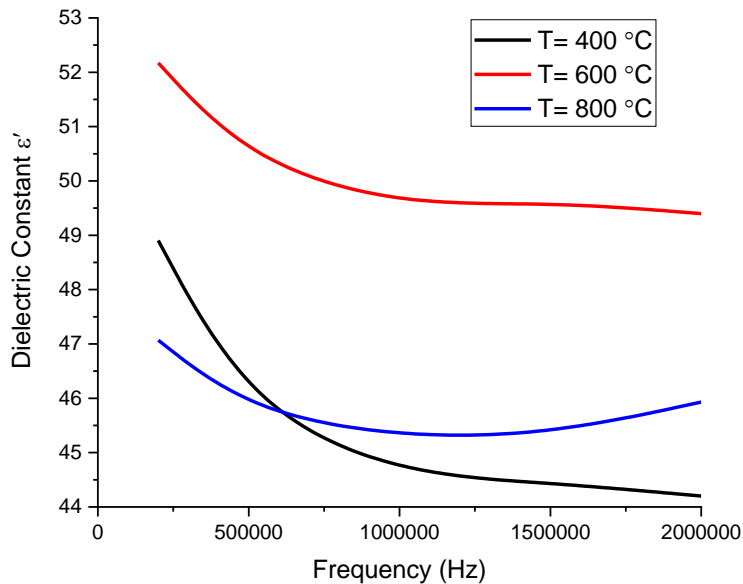


Figure (4.35): Frequency dependence of real part ( $\epsilon'$ ) of  $\text{Zn}_{0.45}\text{Mn}_{0.55}\text{Fe}_2\text{O}_4$  ferrite calcined at different temperatures (400, 600, and 800 °C).

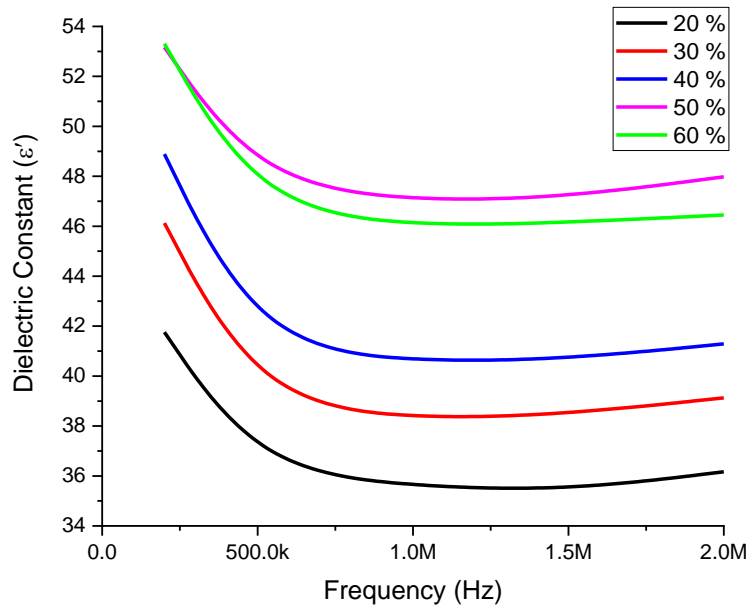


Figure (4.36): Frequency dependence of real part ( $\epsilon'$ ) of  $\text{TiO}_2 \text{ Zn}_{0.45}\text{Mn}_{0.55}\text{Fe}_2\text{O}_4$  mixed with different ratios of  $\text{TiO}_2$  (20, 30, 40, 50 and 60%) respectively.

#### 4.4.1.2 Dielectric loss

It is the imaginary component of the dielectric constant ( $\epsilon''$ ), which is obtained from conductance (G) measured experimentally, that represents the energy absorbed by the sample when subjected to an external applied field.

The variation in  $\epsilon''$  with frequency from 200 KHz to 2 MHz at different temperatures from 400, 600, and 800 °C for ( $\text{MnFe}_2\text{O}_4$ ) samples is shown in Figure (4-37) and table (4-12) [145].

Figures (4-38, 4-39, 4-40 and 4-41) and table (4-13, 4-14, 4-15 and 4-16) presents the electric properties of  $\text{Zn}_x\text{Mn}_{1-x}\text{Fe}_2\text{O}_4$  ferrite at the concentrations ( $x = 0.15, 0.25, 0.35$  and  $0.45$ ) correspondingly. The significant energy dissipation in the material can be blamed for the rise in ( $\epsilon''$ ) with increasing temperature for all of

these samples. There were greater values of ( $\epsilon''$ ) at lower frequencies, which fell as the frequency increased and became linear at higher frequencies.

Figure (4-42) and table (4-17) shows the LCR meter readings of pure  $\text{TiO}_2$  nanoparticles and  $\text{Zn}_{0.45}\text{Mn}_{0.55}\text{Fe}_2\text{O}_4$  with varying  $\text{TiO}_2$  nanoparticle ratios calcined at  $500\text{ }^\circ\text{C}$  for the research of the  $\text{Zn}_{0.45}\text{Mn}_{0.55}\text{Fe}_2\text{O}_4$  ferrite nanocomposite (20%, 30%, 40%, 50%, and 60 %).

The greater values of ( $\epsilon''$ ) at relatively low frequency may be attributable to the contribution originating from both the conduction and relaxation losses[146]. At higher frequencies, the relaxation losses are the only causes of dielectric loss. It is also found that ( $\epsilon''$ ) grows with greater conducting [146].

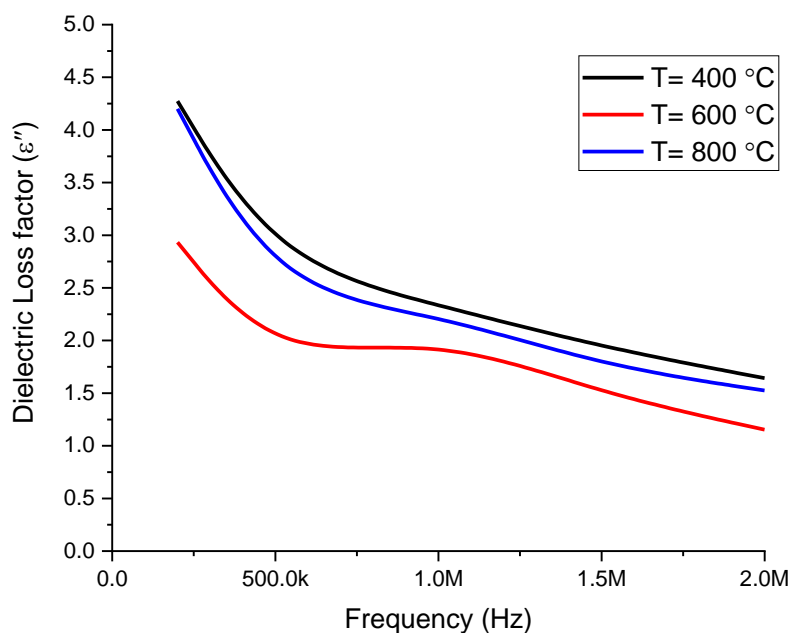
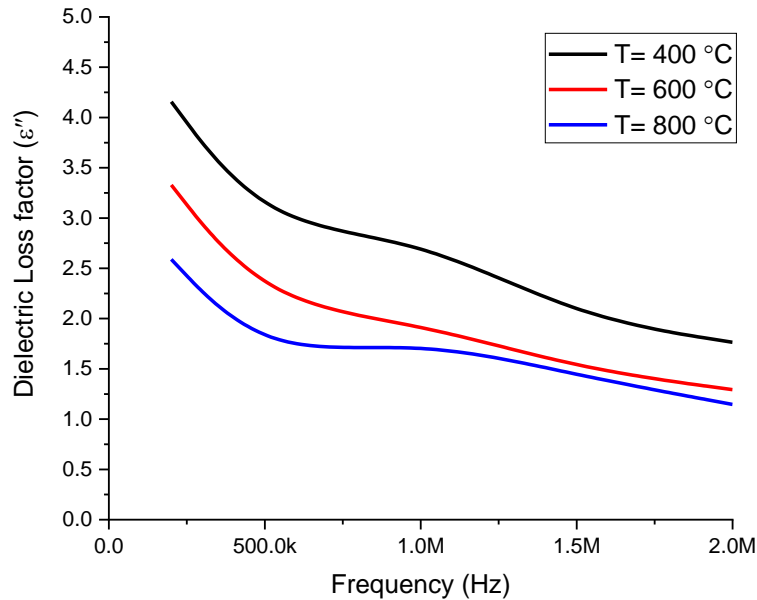
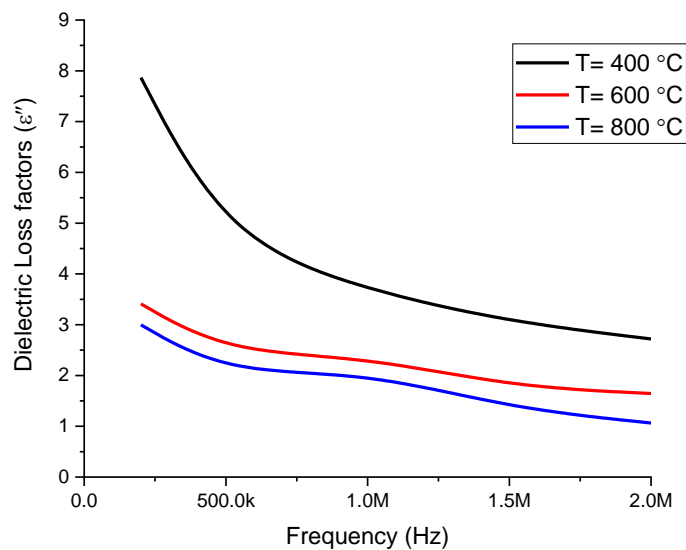


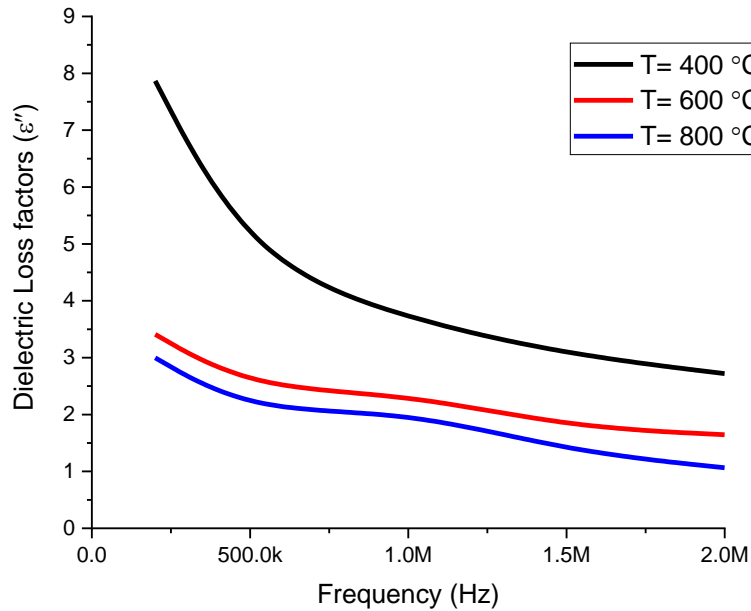
Figure (4.37): variation of ( $\epsilon''$ ) with  $f$  (Hz) of  $\text{MnFe}_2\text{O}_4$  ferrite calcined at different temperatures (400, 600, and  $800\text{ }^\circ\text{C}$ ).



Figure(4.38):variation of ( $\epsilon''$ ) with f (Hz) of  $\text{Zn}_{0.15}\text{Mn}_{0.85}\text{Fe}_2\text{O}_4$  ferrite calcined at different temperatures (400, 600, and 800 °C).



Figure(4.39):variation of ( $\epsilon''$ ) with f (Hz) of  $\text{Zn}_{0.25}\text{Mn}_{0.75}\text{Fe}_2\text{O}_4$  ferrite calcined at different temperatures (400, 600, and 800 °C).



Figure(4.40):variation of ( $\epsilon''$ ) with f (Hz) of  $\text{Zn}_{0.35}\text{Mn}_{0.65}\text{Fe}_2\text{O}_4$  ferrite calcined at different temperatures (400, 600,and 800 °C).

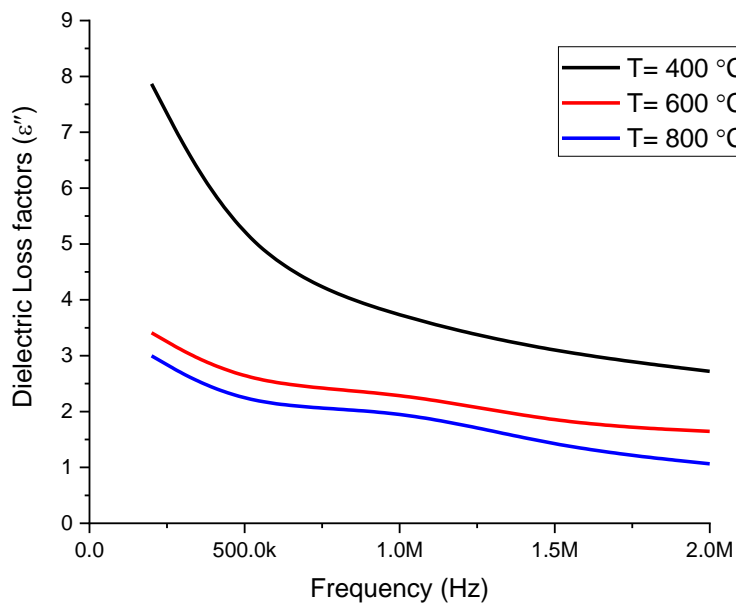


Figure (4.41):variation of ( $\epsilon''$ ) with f (Hz) of  $\text{Zn}_{0.45}\text{Mn}_{0.55}\text{Fe}_2\text{O}_4$  ferrite calcined at different temperatures (400, 600,and 800 °C).

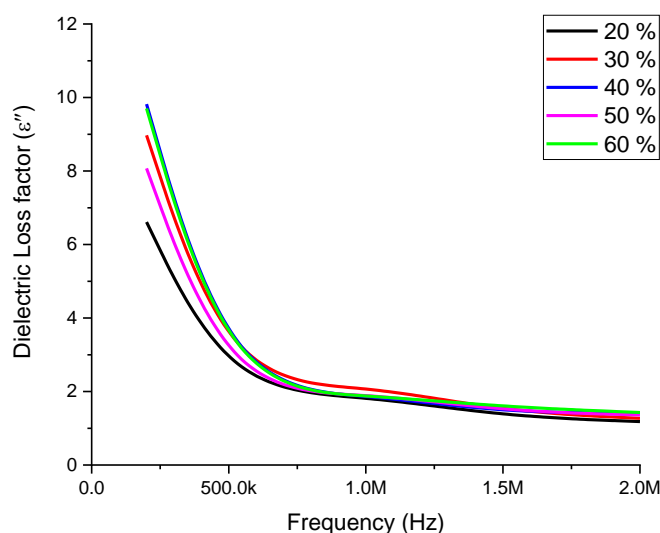


Figure (4.42): variation of ( $\epsilon''$ ) with  $f$  (Hz) of  $\text{TiO}_2$  with  $\text{Zn}_{0.45}\text{Mn}_{0.55}\text{Fe}_2\text{O}_4$  mixed with different ratios of  $\text{TiO}_2$  (20%, 30%, 40%, 50% and 60%) respectively.

#### 4.4.1.3 Dielectric loss ( $\tan \delta$ )

Figure (4-43) and table (4-12) depicts the frequency dependence of the loss tangent ( $\tan \delta$ ) for each sample. The aggregate contribution of charge carriers in the material led to a tiny all aberrant behavior for all samples at lower frequencies. There were distinct peaks in the loss spectra, which indicated the presence of relaxing dipoles in each sample. However, the  $\text{Mn-Fe}_2\text{O}_4$  samples had a significantly greater tangent loss peak frequency than the pure sample. In order to calculate the dielectric loss factor (the amount of energy dissipated in the material), the equation (4-2) is used [147].

Figures (4-44, 4-45, 4-46, and 4-47) and tables (4-13, 4-14, 4-15 and 4-16) shows the change in  $\tan \delta$  for  $(\text{Zn}_x\text{Mn}_{1-x}\text{Fe}_2\text{O}_4)$  samples at the concentrations ( $x = 0.15, 0.25, 0.35$  and  $0.45$ ), correspondingly with applied frequencies ranging from (200 to 2) MHz and temperatures ranging from 400, 600, and 800 °C. At 200 Hz,

the plots in the inset revealed the change in  $(\tan\delta)$ .  $T$ , which suggested a drop in  $\tan\delta$  with the increase in  $T$  ( $\tan\delta$ ) began to drop with rising frequency and became linear at its lowest values for all samples at higher frequencies. Since the polarizability of  $(\text{Zn}_x\text{Mn}_{1-x}\text{Fe}_2\text{O}_4)$  ferrite increased with temperature, the value of  $\tan\delta$  decreased, indicating that the energy retained was greater than the energy lost [148].

To investigate the  $\text{Zn}_{0.45}\text{Mn}_{0.55}\text{Fe}_2\text{O}_4$ , the Dielectric loss or dissipation factor ( $\tan \delta$ ) with frequency measurements of pure  $\text{TiO}_2$  nanoparticles, as well as  $\text{Zn}_{0.45}\text{Mn}_{0.55}\text{Fe}_2\text{O}_4$  with various  $\text{TiO}_2$  nanoparticle ratios, are shown in figure (4-48) and table (4-17), (20%, 30%, 40%, 50%, and 60 %).

The movement of free charge carriers causes dielectric loss, which is the dissipation of electrical energy. Figure 4-48 shows the fluctuation of dielectric loss or dissipation factor ( $\tan \delta$ ) with frequency as a function of  $\text{Zn}_{0.45}\text{Mn}_{0.55}\text{Fe}_2\text{O}_4/\text{TiO}_2$  nanocomposite loading. The dielectric loss increases in direct proportion to the drop in frequency. It's because there is longer time for the free charge carriers to pass across the network. As a result, more energy is available for dissipation factor ( $\tan \delta$ ) in this scenario. Nanocomposite  $\text{Zn}_{0.45}\text{Mn}_{0.55}\text{Fe}_2\text{O}_4/\text{TiO}_2$  loaded increases the ( $\tan \delta$ ) values in general [148]

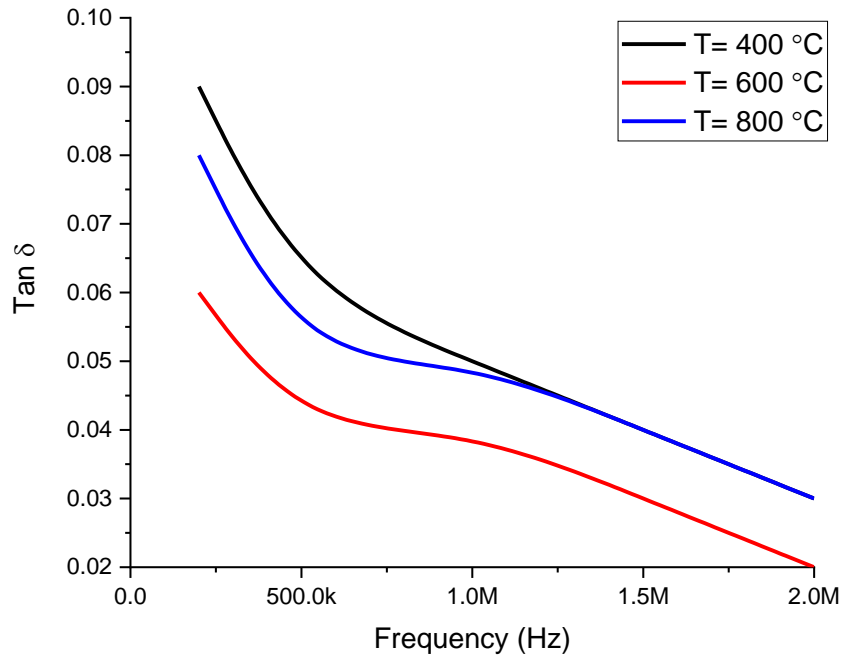


Figure (4.43): variation of  $\tan \delta$  with  $f$  (Hz) of  $\text{MnFe}_2\text{O}_4$  ferrite calcined at different temperatures (400, 600, and 800  $^\circ\text{C}$ ).

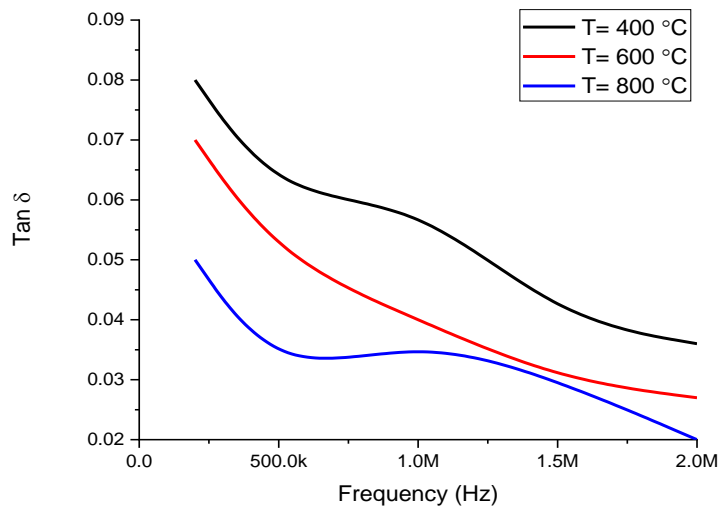


Figure (4.44): variation of  $\tan \delta$  with  $f$  (Hz) of  $\text{Zn}_{0.15}\text{Mn}_{0.85}\text{Fe}_2\text{O}_4$  ferrite calcined at different temperatures (400, 600, and 800  $^\circ\text{C}$ ).

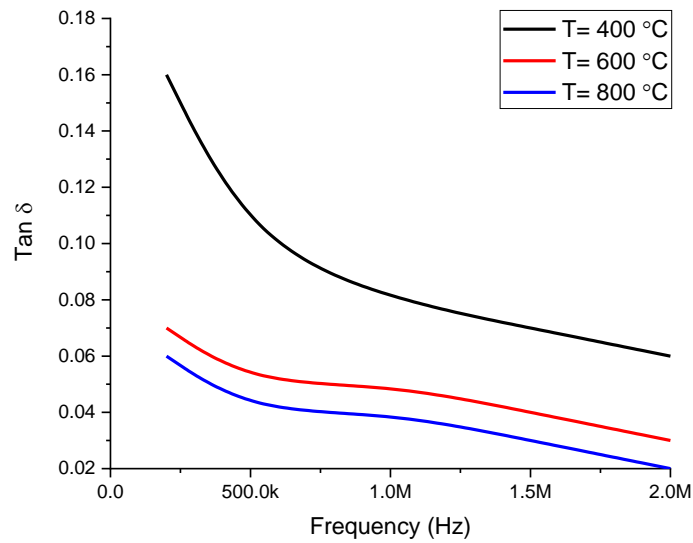


Figure (4.45):variation of  $\tan \delta$  with  $f$  (Hz) of  $\text{Zn}_{0.25}\text{Mn}_{0.75}\text{Fe}_2\text{O}_4$  ferrite calcined at different temperatures (400, 600, and 800 °C).

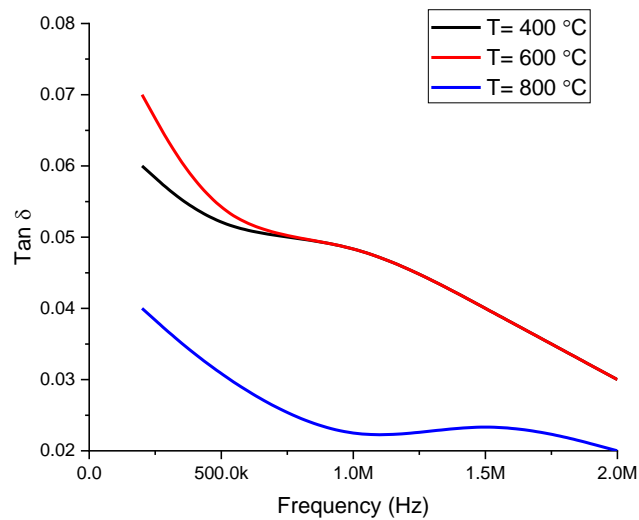


Figure (4.46):variation of  $\tan \delta$  with  $f$  (Hz) of  $\text{Zn}_{0.35}\text{Mn}_{0.65}\text{Fe}_2\text{O}_4$  ferrite calcined at different temperatures (400, 600, 800 °C).

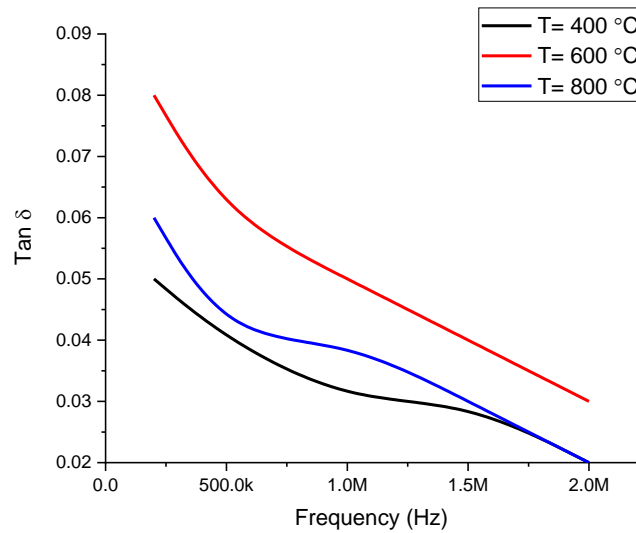


Figure (4.47): variation of  $\tan \delta$  with  $f$  (Hz) of  $\text{Zn}_{0.45}\text{Mn}_{0.55}\text{Fe}_2\text{O}_4$  ferrite calcined at different temperatures (400, 600, 800  $^\circ\text{C}$ ).

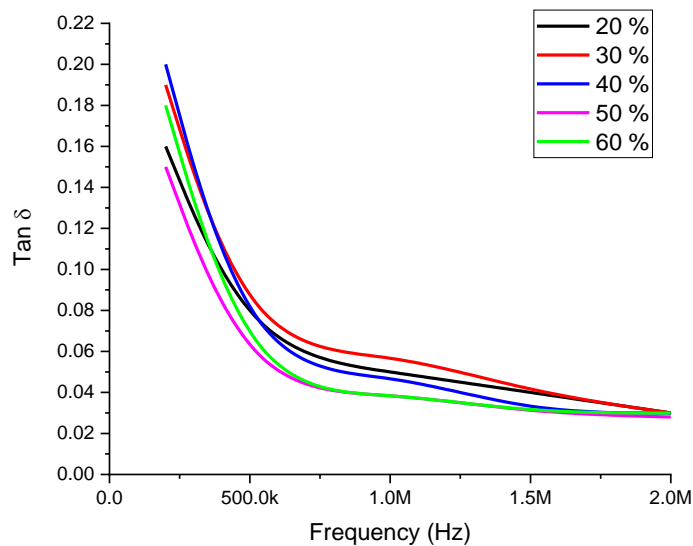


Figure (4.48): variation of  $\tan \delta$  with  $f$  (Hz) of  $\text{TiO}_2$ , with  $\text{Zn}_{0.45}\text{Mn}_{0.55}\text{Fe}_2\text{O}_4$  mixed with different ratios of  $\text{TiO}_2$  (20%, 30%, 40%, 50% and 60%) respectively.

#### 4.4.1.4 AC conductivity

The electrical conductivity ( $\sigma$ ) was calculated from the experimental data of the imaginary part ( $\epsilon''$ ) of dielectric permittivity according to ( $\sigma_{A.C} = 2\pi f \epsilon_0 \epsilon_r''$ ), where  $\epsilon_0$  is the permittivity of vacuum,  $\epsilon_{00}$  the dielectric permittivity and  $\nu$  is the measurement frequency. At low frequencies (below 1 MHz), the dielectric permittivity and the electrical conductivity of composites are strongly dependent on Mn-Fe<sub>2</sub>O<sub>4</sub> concentration.

Figure (4-49) and table (4-12) displays the AC conductivity as a function of frequency of MnFe<sub>2</sub>O<sub>4</sub> nanocomposite. The AC conductivity of MnFe<sub>2</sub>O<sub>4</sub> showed an upward trend in the complete frequency range tested. Generally, the electrical conductivity of mix nanocomposites depends on the synergistic effect of the filler dispersion and blend morphology [149-152].

Figure (4-50, 4-51, 4-52, and 4-53) and tables (4-13, 4-14, 4-15 and 4-16) shows the variation of the AC conductivity as a function of frequency for the samples at different temperature (400, 600, and 800) °C. It was observed that, in all the samples, the AC conductivity was constant up to 100 kHz but increased steeply thereafter, as in disordered materials such as the change in the AC conductivity for (Zn<sub>x</sub>Mn<sub>1-x</sub>Fe<sub>2</sub>O<sub>4</sub>) composite samples at the concentrations ( $x = 0.15, 0.25, 0.35$  and  $0.45$ ), correspondingly with applied frequencies ranging from (200 to 2) MHz and temperatures ranging from (400, 600, and 800) °C [153].

Figure (4-54) and table (4-17) shows the AC conductivity readings of pure and Zn<sub>0.45</sub>Mn<sub>0.55</sub>Fe<sub>2</sub>O<sub>4</sub> with varying TiO<sub>2</sub> nanoparticle ratios calcined at 500 °C for the research of the Zn<sub>0.45</sub>Mn<sub>0.55</sub>Fe<sub>2</sub>O<sub>4</sub>/ TiO<sub>2</sub> ferrite nanocomposite (20%, 30%, 40%, 50%, and 60 %) [154-155].

The AC conductivity of the  $\text{Zn}_{0.45}\text{Mn}_{0.55}\text{Fe}_2\text{O}_4/\text{TiO}_2$  ferrite was further lowered by  $\text{TiO}_2$  addition at higher frequencies. As the particle size fell, the surface-to-volume ratio increased and substantial surface scattering occurred, which resulted in a reduction in the electronic conductivity [156-157]. The increased conductivity at higher frequencies confirms the short-range intrawell hopping of charge carriers between localized states. As a result of  $\text{TiO}_2$  loading, conductivity was found to be reduced because the effective number of charge carriers dropped [158-160].

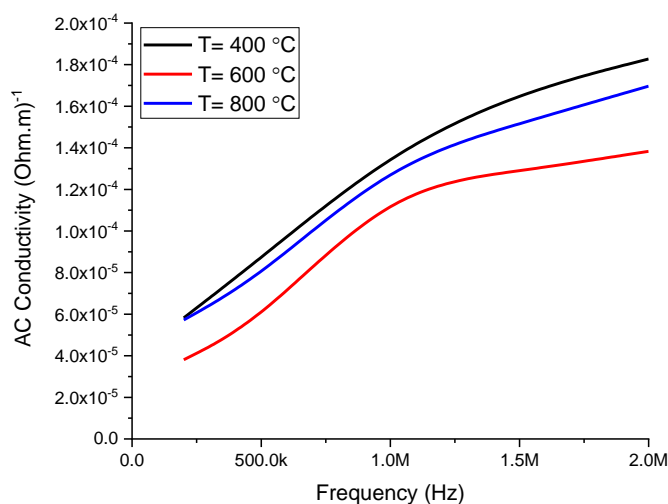


Figure (4.49): The AC conductivity of  $\text{MnFe}_2\text{O}_4$  ferrite calcined at different temperatures (400, 600, and 800 °C).

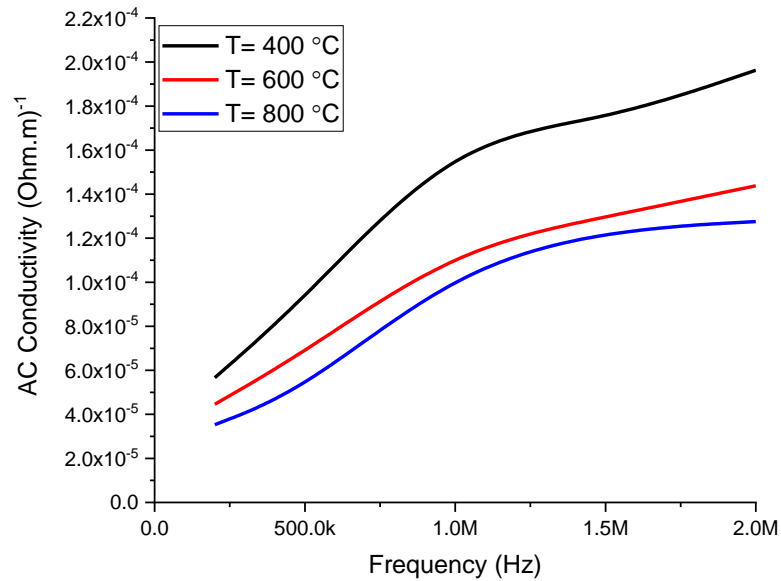


Figure (4.50): The AC conductivity of  $Zn_{0.15}Mn_{0.85}Fe_2O_4$  ferrite calcined at different temperatures (400, 600, and 800 °C).

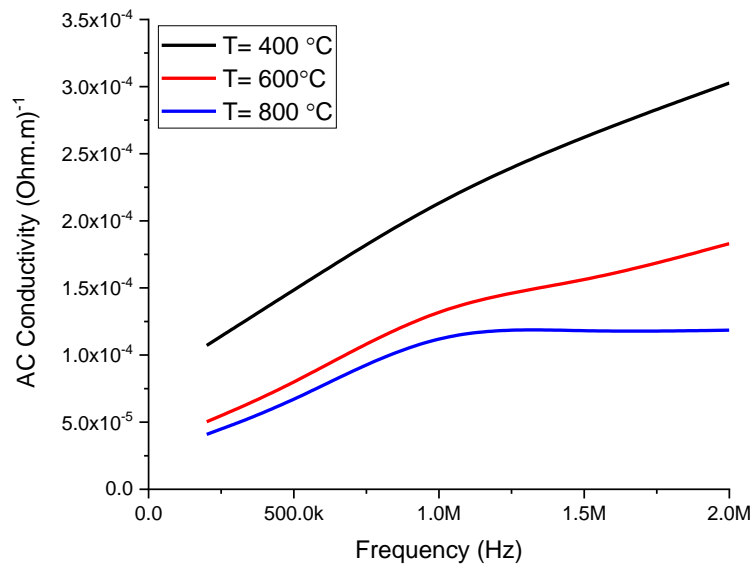


Figure (4.51): The AC conductivity of  $Zn_{0.25}Mn_{0.75}Fe_2O_4$  ferrite calcined at different temperatures (400, 600, and 800 °C).

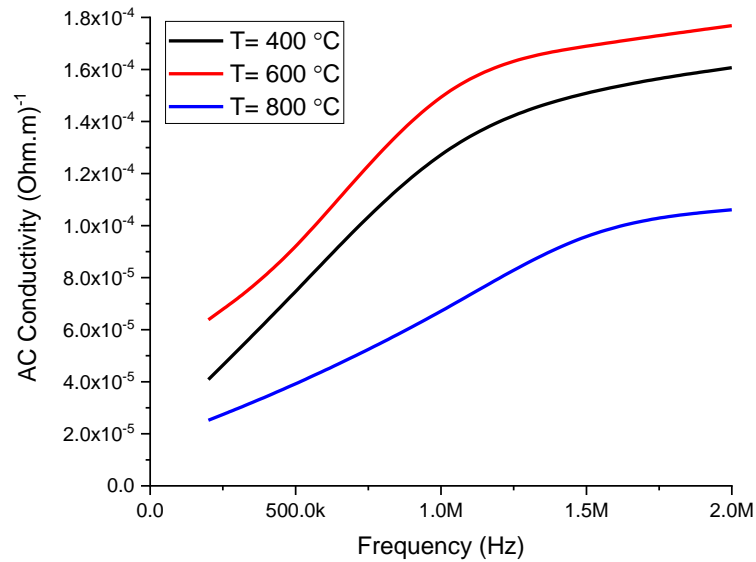


Figure (4.52): The AC conductivity of  $\text{Zn}_{0.35}\text{Mn}_{0.65}\text{Fe}_2\text{O}_4$  ferrite calcined at different temperatures (400, 600, and 800 °C).

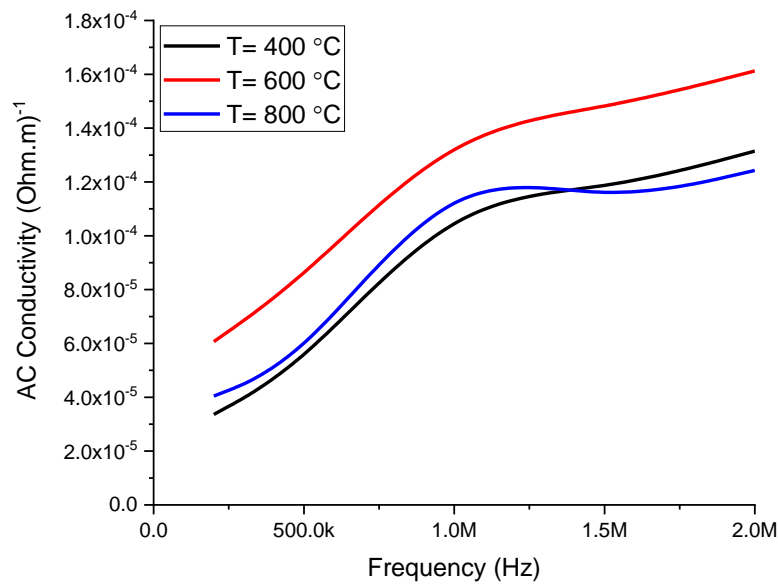


Figure (4.53): The AC conductivity of  $\text{Zn}_{0.45}\text{Mn}_{0.55}\text{Fe}_2\text{O}_4$  ferrite calcined at different temperatures (400, 600, and 800 °C).

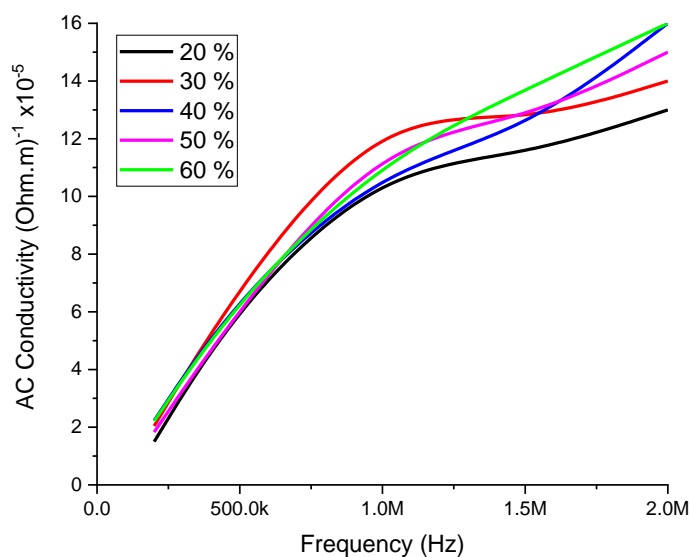


Figure (4.54): The AC conductivity of  $Zn_{0.45}Mn_{0.55}Fe_2O_4$  mixed with different ratios of  $TiO_2$  (20, 30, 40, 50 and 60%) respectively.

Table (4.12): LCR dielectric parameters ( $\epsilon''$ ), ( $\epsilon'$ ), ( $\tan \delta$ ) and ( $\sigma_{ac}$ ) of  $MnFe_2O_4$  for samples calcined at different calcination temperatures (400, 600, and 800) °C.

<i>Frequency</i>	<i>Dielectric Parameters</i>	<i>400 °C</i>	<i>600 °C</i>	<i>800 °C</i>
<b>200 KHz</b>	$\epsilon'$	48.96	84	51.22
	$\epsilon''$	4.27	2.93	4.28
	$\tan \delta$	0.09	0.06	0.08
	$\sigma_{ac} \times 10^{-5}$	5.82	3.81	5.72
<b>500 KHz</b>	$\epsilon'$	46.87	46.6	49.68
	$\epsilon''$	2.74	1.79	2.46
	$\tan \delta$	0.06	0.04	0.05
	$\sigma_{ac} \times 10^{-5}$	8.7	5.7	7.82
<b>1 MHz</b>	$\epsilon'$	45.8	45.8	49.26
	$\epsilon''$	2.34	2.05	2.25
	$\tan \delta$	0.05	0.04	0.05

	$\sigma_{a.c} \times 10^{-5}$	1.38	0.121	0.133
<b>1.5 MHz</b>	$\epsilon'$	45.78	45.6	48.99
	$\epsilon''$	1.93	1.49	1.76
	$\tan \delta$	0.04	0.03	0.04
	$\sigma_a \times 10^{-5}$	1.67	0.129	0.152
<b>2 MHz</b>	$\epsilon'$	46.53	46.3	49.67
	$\epsilon''$	1.64	1.15	1.52
	$\tan \delta$	0.03	0.02	0.03
	$\sigma_{a.c} \times 10^{-5}$	1.83	0.138	0.17

Table (4.13): LCR dielectric parameters ( $\epsilon''$ ), ( $\epsilon'$ ), ( $\tan \delta$ ) and ( $\sigma_{ac}$ ) of  $Zn_{0.15}Mn_{0.85}Fe_2O_4$  nanocomposite for samples calcined at different temperatures (400, 600, and 800) °C.

<b>Frequency</b>	<b>Dielectric Parameters</b>	<b>400 °C</b>	<b>600 °C</b>	<b>800 °C</b>
<b>200 KHz</b>	$\epsilon'$	50.94	47.9	49.51
	$\epsilon''$	4.16	3.33	2.68
	$\tan \delta$	0.08	0.07	0.05
	$\sigma_{a.c} \times 10^{-5}$	5.66	4.45	3.53
<b>500 KHz</b>	$\epsilon'$	48.89	46.7	48.25
	$\epsilon''$	2.90	2.14	1.60
	$\tan \delta$	0.06	0.05	0.03
	$\sigma_{a.c} \times 10^{-5}$	9.25	6.82	5.11
<b>1 MHz</b>	$\epsilon'$	47.71	46.2	47.71
	$\epsilon''$	2.81	1.96	1.79
	$\tan \delta$	0.06	0.04	0.037
	$\sigma_{a.c} \times 10^{-5}$	1.66	0.115	0.106

<b>1.5 MHz</b>	$\dot{\epsilon}$	47.57	46.2	47.68
	$\ddot{\epsilon}$	2.01	1.50	1.43
	$\tan \delta$	0.04	0.03	0.03
	$\sigma_{a.c} \times 10^{-5}$	1.73	0.13	0.12
<b>2 MHz</b>	$\dot{\epsilon}$	48.19	46.8	48.36
	$\ddot{\epsilon}$	1.76	1.29	1.15
	$\tan \delta$	0.036	0.027	0.02
	$\sigma_{a.c} \times 10^{-5}$	1.96	0.144	0.128

Table (4.14): LCR dielectric parameters ( $\epsilon''$ ), ( $\epsilon'$ ), ( $\tan \delta$ ) and ( $\sigma_{ac}$ ) of  $Zn_{0.25}Mn_{0.75}Fe_2O_4$  nanocomposite for samples calcined at different temperatures (400, 600, and 800) °C.

<b>Frequency</b>	<b>Dielectric Parameters</b>	<b>400 °C</b>	<b>600 °C</b>	<b>800 °C</b>
<b>200 KHz</b>	$\dot{\epsilon}$	48.90	52.2	47.07
	$\ddot{\epsilon}$	7.87	3.41	2.99
	$\tan \delta$	0.16	0.07	0.06
	$\sigma_{a.c} \times 10^{-5}$	1.07	5.03	4.09
<b>500 KHz</b>	$\dot{\epsilon}$	45.80	50.4	45.77
	$\ddot{\epsilon}$	4.67	2.45	2.04
	$\tan \delta$	0.10	0.05	0.04
	$\sigma_{a.c} \times 10^{-5}$	1.49	7.80	6.49
<b>1 MHz</b>	$\dot{\epsilon}$	44.59	49.5	45.27
	$\ddot{\epsilon}$	3.67	2.37	2.07
	$\tan \delta$	0.08	0.05	0.04
	$\sigma_{a.c} \times 10^{-5}$	2.17	0.14	0.12

<b>1.5 MHz</b>	$\epsilon'$	44.45	49.6	45.33
	$\epsilon''$	3.05	1.78	1.35
	$\tan \delta$	0.07	0.04	0.03
	$\sigma_{a.c} \times 10^{-5}$	26.4	0.154	0.117
<b>2 MHz</b>	$\epsilon'$	44.2	49.9	45.93
	$\epsilon''$	2.72	1.65	1.07
	$\tan \delta$	0.06	0.03	0.02
	$\sigma_{a.c} \times 10^{-5}$	30.3	0.18	0.12

Table (4.15): LCR dielectric parameters ( $\epsilon''$ ), ( $\epsilon'$ ), ( $\tan \delta$ ) and ( $\sigma_{ac}$ ) of  $Zn_{0.35}Mn_{0.65}Fe_2O_4$  nanocomposite for samples calcined at different temperatures (400, 600, and 800) °C.

<b>Frequency</b>	<b>Dielectric Parameters</b>	<b>400 °C</b>	<b>600 °C</b>	<b>800 °C</b>
<b>200 KHz</b>	$\epsilon'$	47.95	50.4	46.68
	$\epsilon''$	2.99	3.67	1.85
	$\tan \delta$	0.06	0.07	0.04
	$\sigma_{a.c} \times 10^{-5}$	4.08	6.38	2.52
<b>500 KHz</b>	$\epsilon'$	46.55	48.6	45.63
	$\epsilon''$	2.33	2.59	1.21
	$\tan \delta$	0.05	0.05	0.03
	$\sigma_{a.c} \times 10^{-5}$	7.41	8.81	3.86
<b>1 MHz</b>	$\epsilon'$	45.71	47.3	45.16
	$\epsilon''$	2.27	2.60	1.12
	$\tan \delta$	0.05	0.05	0.02
	$\sigma_{a.c} \times 10^{-5}$	1.34	0.16	6.59
	$\epsilon'$	45.57	47.1	45.08

<b>1.5 MHz</b>	$\tilde{\epsilon}$	1.77	1.69	1.17
	$\tan \delta$	0.04	0.04	0.025
	$\sigma_{a.c} \times 10^{-5}$	15.3	0.17	0.10
<b>2 MHz</b>	$\dot{\epsilon}$	45.15	48.2	45.63
	$\tilde{\epsilon}$	1.44	1.59	0.95
	$\tan \delta$	0.03	0.03	0.02
	$\sigma_{a.c} \times 10^{-5}$	1.61	0.18	0.11

Table (4.16): LCR dielectric parameters ( $\epsilon''$ ), ( $\epsilon'$ ), ( $\tan \delta$ ) and ( $\sigma_{ac}$ ) of  $Zn_{0.45}Mn_{0.55}Fe_2O_4$  nanocomposite for samples calcined at different temperatures (400, 600, and 800) °C.

<b>Frequency</b>	<b>Dielectric Parameters</b>	<b>400 °C</b>	<b>600 °C</b>	<b>800 °C</b>
<b>200 KHz</b>	$\dot{\epsilon}$	48.69	48.6	47.03
	$\tilde{\epsilon}$	2.47	3.74	2.97
	$\tan \delta$	0.05	0.08	0.06
	$\sigma_{a.c} \times 10^{-5}$	3.36	6.06	4.04
<b>500 KHz</b>	$\dot{\epsilon}$	47.39	47.7	46.16
	$\tilde{\epsilon}$	1.93	2.65	1.69
	$\tan \delta$	0.04	0.06	0.04
	$\sigma_{a.c} \times 10^{-5}$	5.18	8.42	5.36
<b>1 MHz</b>	$\dot{\epsilon}$	46.89	46.6	45.63
	$\tilde{\epsilon}$	1.54	2.37	2.15
	$\tan \delta$	0.03	0.05	0.047
	$\sigma_{a.c} \times 10^{-5}$	1.15	0.14	0.13
	$\dot{\epsilon}$	46.70	47.2	45.63
	$\tilde{\epsilon}$	1.35	1.70	1.29

<b>1.5 MHz</b>	<b><math>\tan \delta</math></b>	0.03	0.04	0.03
	<b><math>\sigma_{a.c} \times 10^{-5}</math></b>	1.17	0.15	0.11
<b>2 MHz</b>	<b><math>\dot{\epsilon}</math></b>	47.46	47.5	46.34
	<b><math>\ddot{\epsilon}</math></b>	1.18	1.45	1.12
	<b><math>\tan \delta</math></b>	0.02	0.03	0.02
	<b><math>\sigma_{a.c} \times 10^{-5}</math></b>	1.31	0.161	0.124

Table (4.17): LCR dielectric parameters ( $\epsilon''$ ), ( $\epsilon'$ ), ( $\tan \delta$ ) and ( $\sigma_{ac}$ ) of  $Zn_{0.45}Mn_{0.55}Fe_2O_4$  nanocomposite mixed with different content of  $TiO_2$ .

<b>Frequency</b>	<b>Dielectric Parameters</b>	<b>20 %</b>	<b>30 %</b>	<b>40 %</b>	<b>50%</b>	<b>60%</b>
<b>200 KHz</b>	<b><math>\dot{\epsilon}</math></b>	41.76	46.13	48.89	53.17	53.31
	<b><math>\ddot{\epsilon}</math></b>	6.61	8.97	9.82	8.07	9.70
	<b><math>\tan \delta</math></b>	0.16	0.19	0.2	0.15	0.18
	<b><math>\sigma_{a.c} \times 10^{-5}</math></b>	1.50	2.04	2.23	1.83	2.21
<b>500 KHz</b>	<b><math>\dot{\epsilon}</math></b>	36.30	39.04	41.28	47.82	46.80
	<b><math>\ddot{\epsilon}</math></b>	2.00	2.19	2.09	1.95	2.06
	<b><math>\tan \delta</math></b>	0.06	0.06	0.05	0.04	0.04
	<b><math>\sigma_{a.c} \times 10^{-5}</math></b>	6.37	6.99	6.67	6.19	6.55
<b>1 MHz</b>	<b><math>\dot{\epsilon}</math></b>	35.57	38.25	40.55	46.97	45.98
	<b><math>\ddot{\epsilon}</math></b>	1.89	2.19	1.92	1.98	1.91
	<b><math>\tan \delta</math></b>	0.05	0.06	0.05	0.04	0.04
	<b><math>\sigma_{a.c} \times 10^{-5}</math></b>	11	13	11	12	11.3
<b>1.5 MHz</b>	<b><math>\dot{\epsilon}</math></b>	35.41	38.47	40.68	47.16	46.15
	<b><math>\ddot{\epsilon}</math></b>	1.32	1.45	1.42	1.46	1.58
	<b><math>\tan \delta</math></b>	0.04	0.04	0.03	0.03	0.03
	<b><math>\sigma_{a.c} \times 10^{-5}</math></b>	11.4	12.5	12.2	12.6	13.7

<b>2 MHz</b>	$\dot{\epsilon}$	36.17	39.13	41.29	47.98	46.45
	$\ddot{\epsilon}$	1.18	1.27	1.42	1.36	1.43
	$\tan \delta$	0.03	0.03	0.03	0.028	0.03
	$\sigma_{a.c} \times 10^{-5}$	13	14	16	15	16

#### 4.5 Conclusions:

$Zn_xMn_{1-x}Fe_2O_4$  ferrite and  $Zn_xMn_{1-x}Fe_2O_4/TiO_2$  nanocomposites ( $x = 0, 0.15, 0.25, 0.35$  and  $0.45$ ) successfully synthesized at different calcination temperatures (650, 750 and 850 °C) using Sol-Gel method. These nanostructure used to study the structure, magnetic, and electrical properties. This method having characteristic like, very simple, cost low, eco-friendly with which the method can be scaled up economic viability with high-quality products of different nanostructures.

According to the presented results in this work, it can be concluded the following points:

1-The XRD patterns referred that the crystalline growth of  $MnFe_2O_4$  ferrite was in the same cubic crystal structure at the different temperatures.

From figure 4-5 on can observed that at the concentration of zinc metal ( $x=0.45$ ), a pure single-phase cubic spinel  $Zn_xMn_{1-x}Fe_2O_4$  structure was obtained with space group (Fd-3m no. 277), crystal dimensions ( $a = b = c = 8.438 \text{ \AA}$ ) and crystal angles ( $\alpha = \beta = \gamma = 90^\circ$ ).

2- It's also note the coalescence of adjacent grains with each other due to the increase in the concentration of  $TiO_2$ . The particle size measured using FE-SEM micrographs is larger than the XRD data estimates.

3- The FT-IR calculations of created  $Zn_xMn_{1-x}Fe_2O_4$ . It gets that the crystalline size slightly increased with raising the calcination temperature and the zinc content which is the common behavior of all synthesized material, attributed to the appearance of the peak with increase the calcination temperature and the zinc content, and this is corresponded with the measured FT-IR spectrum.

4- With  $M_s$  values of (4.7), (4.05), (3.7), (0.84), and (0.73) emu/g. Measurements of its remanence magnetization ( $M_s$ ) and coercivity ( $H_c$ ) is (5.75), (6.5), (6), (95), and (8) show that this material is super-paramagnetic.

5-The change in the values of different dielectric characteristics such as  $\epsilon'$ ,  $\epsilon''$ ,  $\tan \delta$  and  $\sigma_{ac}$  by increasing the temperatures of  $Zn_xMn_{1-x}Fe_2O_4$  nanoparticles at (400, 600 and 800 oC), were determined, compared and explained.

6-This method having characterisitic like, very simple, cost low, eco-friendly with which the method can be scaled up economic viability with high-quality products of different nanostructures. Magnetically flexible ferrites are used in cores for transformer windings, electric motors, and transceiver antennas, In HF technology, in the construction of antennas and in parts for moderators, In headphones for electronic recording equipment, video equipment, and hard disks, and Stealth and camouflage technology (ferrites absorb radar waves).

#### 4.6 Future works:

The excellent results obtained in this work impel us to offer some suggestions for the development of future studies such as:

1. Synthesis of  $Zn_xMn_{1-x}Fe_2O_4$  ferrite nano composite NPs in vacuum and using microorganisms to get a clean sample. Preparing of  $Zn_xMn_{1-x}Fe_2O_4$  ferrite nanocomposite NPs by hydrothermal and microwave irradiation method with comparing results. Synthesis of metal oxide using chemical methods and study applications in removal heavy metals.
2. Discovery could be targeted for the promising potential applications including metal alloys industry, drug delivery, transistors, and treatment of cancer tissue .
3. Studying of optoelectronic applications such as solar cell and photodetector for  $Zn_xMn_{1-x}Fe_2O_4$  ferrite nanocomposite NPs/PS samples that prepared in this research.
4.  $Zn_xMn_{1-x}Fe_2O_4/TiO_2$  NPs using as doping copper materials by electrolyte solution during prepare porous silicon and their results are compared with current work.

5. Viral novel green approaches methods for synthesizing NPs using different natural sources such as algae, bacteria, and fungi extracts and evaluation of their catalytic activity.



---

# References

---





## References

---

### References

- [1] T. Pradeep, "Nano: the Essentials: Understanding Nanoscience and Nanotechnology", McGraw-Hill Education,( 2007).
- [2] S. Mahalakshmi, K. SrinivasaManja, and S. Nithiyantham, "Electrical Properties of Nanophase Ferrites Doped with Rare Earth Ions", Journal of Superconductivity and Novel Magnetism, Vol. 27, No. 9, pp. 2083-2088, (2014).
- [3] A. M. Kumar, M. C. Varma, C. L. Dube, K. Rao, and S. C. Kashyap, "Development of Ni–Zn Nanoferrite Core Material with Improved Saturation Magnetization and DC resistivity," Journal of Magnetism and Magnetic Materials, Vol. 320, No. 14, pp. 1995-2000, (2008).
- [4] Y. Hwang, "Microwave Absorbing Properties of Ni Zn-ferrite Synthesized From Waste Iron Oxide Catalyst," Materials Letters, Vol. 60, No. 27, pp. 3277-3280, (2006).
- [5] W. Yan, Q. Li, H. Zhong, and Z. Zhong, "Characterization and Lowtemperature Sintering of Ni<sub>0.5</sub>Zn<sub>0.5</sub>Fe<sub>2</sub>O<sub>4</sub> Nano-Powders Prepared by Refluxing Method," PowderTechnology, Vol. 192, No. 1, pp. 23-26, (2009).
- [6] M. Javed Iqbal, z. Ahmad, t. Meydan, and y. Melikhov, "Physical, Electrical andMagnetic Properties of Nano-Sized co-cr Substituted Magnesium Ferrites," Gournal of Applied Physics, Vol. 111, No. 3, pp. 033906, (2012).
- [7] M. Srivastava, S. Chaubey, and A. K. Ojha, "Investigation on Size Dependent Structural And Magnetic Behavior Of Nickel Ferrite Nanoparticles Prepared By Sol– gel and Hydrothermal Methods," Materials Chemistry and Physics, Vol. 118, No. 1, pp. 174-180,( 2009).
- [8] A. Rafferty, Y. Gun'ko, And R. Raghavendra,"An Investigation Of Co-fired Varistor-NiZn Ferrite Multilayers", Materials Research Bulletin, Vol. 44, No. 4, pp. 747-752,(2009).

## References

---

- [9] M. Zenger, "Modern Ferrite Technologies And Products," International Journal of Materials and Product Technology, Vol. 9, No. 4-6, pp. 265-280, (1994).
- [10] M. Wen, Q. Li, and Y. Li, "Magnetic, Electronic And Structural Properties of  $Zn_xFe_{3-x}O_4$ ," Journal of Electron Spectroscopy and Related Phenomena, Vol. 153, No. 3, pp. 65-70, (2006).
- [11] P. Roy, and J. Bera, "Enhancement of The Magnetic Properties of Ni-Cu-Zn Ferrites with The Substitution of A Small Fraction Of Lanthanum For Iron," Materials Research Bulletin, Vol. 42, No. 1, pp. 77-83, (2007).
- [12] Z. Lazarević, Č. Jovalekić, A. Milutinović, M. Romčević, and N. Romčević, "Preparation and Characterization of Nano Ferrites," Acta Physica Polonica, A., Vol. 121, No. 3, pp. 682-687, (2012).
- [13] D. Bhalla, S.K. Aggarwal, G.P. Govil and Ish Kakkar," Manufacturing of Manganese-Zinc Soft Ferrite by Powder Metallurgy", The Open Materials Science Journal, Vol. 4, pp. 26-31, (2010).
- [14] N. Deraz, and A. Alarifi, "Structural, Morphological And Magnetic Properties Of Nano-Crystalline Zinc Substituted Cobalt Ferrite System," Journal of Analytical And Applied Pyrolysis, Vol. 94, pp. 41-47, (2012).
- [15] D. Varshney, K. Verma and A. Kumar, "Structural And Vibrational Properties Of  $Zn_xMn_{1-x}Fe_2O_4$  ( $x = 0.0, 0.25, 0.50, 0.75, 1.0$ ) Mixed Ferrites", Materials Chemistry And Physics, Vol. 131, pp. 413-419, (2011).
- [16] M. Arana , P.G. Bercoffa, S. E. Jacoboc," Li-Substituted Mn-Zn Ferrite: Structural And Magnetic Properties After Different Thermal Treatments", Procedia Materials Science, pp. 620 – 627, (2012).
- [17] M. Zhang, Z. Zi, Q. Liu, P. Zhang, X. Tang, J. Yang, X. Zhu, Y. Sun, and J. Dai, "Size Effects On Magnetic Properties of  $Ni_{0.5}Zn_{0.5}Fe_2O_4$  Prepared By Sol-

## References

---

- Gel Method,” *Advances in Materials Science and Engineering*, Vol., ( 2013).
- [18] Veverka, M. Zaveta, K. Kaman, O. Veverka, P. Knizek, K. Pollert, E. Burian, M. Kaspar, “Magnetic Heating By Silica-Coated Co-Zn Ferrite Particles”, *Journal of Physics D: Applied Physics*, Vol. 47, pp. 6, ( 2014).
- [19] R. Rajendra, B. Pushpinder and N. Rajlakshmi, “Structural and Electric Properties of Titanium Substituted Ni-Cu-Zn Ferrite”, *International Journal of Chemical and Physical Sciences*, Vol. 3, 2014.
- [20] R. J. Joseyphus, A. Narayanasamy, B. Jeyadevan, K. Shinoda and K. Tohji, “Superparamagnetic Particle Size Limit of Mn-Zn Ferrite Nanoparticles Synthesised Through Aqueous Method”, Balachandran Jeyadevan, 2015.
- [21] C. Stergiou, “Microstructure and Electromagnetic Properties of Ni-Zn-Co Ferrite upto 20 GHz”, *Hindawi Publishing Corporation Advances in Materials Science and Engineering*, pp. 7, 2016.
- [22] S.B. Singh, Ch. Srinivas, B.V. Tirupanyam, C.L. Prajapat, M.R. Singh, S.S. Meena, Pramod Bhatt, S.M. Yusuf, D.L. Sastry, “Structural, Thermal And Magnetic Studies of  $Mg_xZn_{1-x}Fe_2O_4$  Nanoferrites: Study Of Exchange Interactions On Magnetic Anisotropy”, *Ceramics International*, Vol. 42, pp. 19188-19195, (2016).
- [23] V. J. Angadi, L. Choudhury, K. Sadhana, Hsiang-Lin Liu, R. Sandhya, S. Matteppanavar, B. Rudraswamy, V. Pattar, R.V. Anavekar, K. Praveena, “Structural, Electrical And Magnetic Properties Of  $Sc^{3+}$  Doped Mn-Zn Ferrite Nanoparticles”, *Journal of Magnetism and Magnetic Materials*, Vol. 424, pp. 111, (2017).
- [24] L. G. Petrescu, M. C. Petrescu, V. Ionit, E. Cazacu and C. D. Constantinescu, “Magnetic Properties of Manganese-Zinc Soft Ferrite Ceramic for High Frequency Applications”, *materials*, Vol. 12, pp. 3173, (2019).

## References

---

- [25] N. Vahdati and A. Sedghi, Synthesis of nano Mn-Zn ferrites by gel combustion method with three different fuels and investigation of their structure and properties, *Materials Science-Poland*, Vol. 38, pp. 350-358, (2020).
- [26] N. Jahan, M. N. Khan, and J. I. Khandaker, "Exploration through Structural, Electrical, and Magnetic Properties of Al<sup>3+</sup> Doped Ni-Zn-Co Nanospinel Ferrites", *ACS Omega*, Vol. 6, pp. 32852-3286, (2021).
- [27] S. Akhter, M.A. Hakim, S.M. Hoque, H.N. Das, Disorder Magnetic Behavior Of Zn-Substituted Cu<sub>1-x</sub>Zn<sub>x</sub>Fe<sub>2</sub>O<sub>4</sub> Spinel Ferrites", *Solid State Communications*, Vol. 326, pp. 114181, (2021).
- [28] H.-Y. Chen, C. Tu, T.-H. Wang, Y. Ding, T. Liao, L. Jou, F. Jou, and Y.-D. Yao, "Synthesis and Magnetic Properties of BiFeO<sub>3</sub>, (BiFeO<sub>3</sub>)<sub>0.95</sub>(BaTiO<sub>3</sub>)<sub>0.05</sub>, and (Bi<sub>0.95</sub>Ba<sub>0.05</sub>)(Fe<sub>0.95</sub>Ti<sub>0.05</sub>)O<sub>3</sub> Ceramics," *IEEE Transactions on Magnetics*, Vol. 47, No. 3, pp. 706-709, (2011).
- [29] Justine Wallyn, Nicolas Anton and Thierry F. Vandamme, "Synthesis, Principles, and Properties of Magnetite Nanoparticles for In Vivo Imaging Applications-A Review", *Pharmaceutics*, Vol.11, No.11:601, pp.1-29, (2019).
- [30] Tiefenauer, L. X., Kuehne, G., & Andres, R. Y. (1993). Antibody-magnetite nanoparticles: in vitro characterization of a potential tumor-specific contrast agent for magnetic resonance imaging. *Bioconjugate chemistry*, 4(5), 347-352.
- [31] Stephen Blundell, "Magnetism in Condensed Matter" Oxford University Press, (2001).

## References

---

- [32] Soshin Chikazumi, "Physics of Magnetism", John Wiley and Sons, Inc, New York, (1964).
- [33] William D. Callister, Jr., "Materials Science and Engineering: An Introduction", 7th Ed, John Wiley & Sons, Inc, (2007).
- [34] Michael E. McHenry, "Magnetic Moment and Magnetization", Characterization of Materials, (2002).
- [35] J. B. Goodenough "Theory of the Role of Covalence in the Perovskite-Type Manganites [La, M(II)]MnO<sub>3</sub>" Phys. Rev, 100, Vol. 564 (1955).
- [36] F. Kubel and H. Schmid, "Structure of a Ferroelectric and Ferroelastic Monodomain Crystal of the Perovskite BiFeO<sub>3</sub>" Acta Crystallogr B, Vol 46 part 6, pp 698-702 (1990).
- [37] Muhammad Ajmal, "Fabrication and Physical Characterization of Ni<sub>1-x</sub>Zn<sub>x</sub>Fe<sub>2</sub>O<sub>4</sub> and Cu<sub>1-x</sub>Zn<sub>x</sub>Fe<sub>2</sub>O<sub>4</sub>" PhD Thesis. Quaid-i-Azam University Ferrites Islamabad, Pakistan, (2008).
- [38] I. Harris, and A. Williams, "Material Science and Engineering, Vol. II, Magnetic Materials," IR Harris and AJ Williams School of Metallurgy and Materials-University of Birmingham-Birmingham-UK, 2000.
- [39] S. Blundell, "Magnetism in condensed matter," American Association of Physics Teachers, 2003.
- [40] I. Harris, and A. Williams, "Material Science and Engineering, Vol. II, Magnetic Materials," IR Harris and AJ Williams School of Metallurgy and Materials-University of Birmingham-Birmingham-UK, 2000.
- [41] Muhammad Ajmal, "Fabrication and Physical Characterization of Ni<sub>1-x</sub>Zn<sub>x</sub>Fe<sub>2</sub>O<sub>4</sub> and Cu<sub>1-x</sub>Zn<sub>x</sub>Fe<sub>2</sub>O<sub>4</sub>" PhD Thesis. Quaid-i-Azam University Ferrites Islamabad, Pakistan, (2008).

## References

---

- [42] And Kaa Farhan al-Jubouri, d. Fahr Ghaleb Hayati, "The Electrical and Magnetic Properties of Materials", University of Mosul, Dar Al-Kutub for Printing and Publishing (1985).
- [43] Tahseen Hussein Mubarak, "Preparing The Electrical Transformer Core And Studying Its Structural And Physical Properties" Phd Thesis, University of Technology, Department of Applied Sciences, (2003).
- [44] Vijaya, Rangarajan, "Materials Science", McGraw-Hill Publishing Company Limited, New Delhi, (2000).
- [45] Muhammad Ajmal, "Fabrication and Physical Characterization of  $Ni_{1-x}Zn_xFe_2O_4$  and  $Cu_{1-x}Zn_xFe_2O_4$ " Islamabad, Pakistan, (2008) PhD Thesis. Quaid-i-Azam University
- [46] S. O. Pillai, *Solid State Physics*, New Age International Publications: New Delhi, (2010).
- [47] J. Sólyom, *Fundamentals of the Physics of Solids: Volume 1: Structure and Dynamics*, Springer Science & Business Media: Verlag, Heidelberg, (2007).
- [48] W. Heer, and V. Kresin, "In Handbook of Nanophysics; Sattler KD, editor., Ed," CRC Press: Singapore, (2011).
- [49] S. O. Pillai, *Solid State Physics*, New Age International Publications: New Delhi, (2010).
- [50] Muhammad Ajmal, "Fabrication and Physical Characterization of  $Ni_{1-x}Zn_xFe_2O_4$  and  $Cu_{1-x}Zn_xFe_2O_4$ " Islamabad, Pakistan, (2008). Quaid-i-Azam University

## References

---

- [51] W. Callister, *Materials Science And Engineering An Introduction*, Sixth ed. New York: John Wiley & Sons, Inc, (2003).
- [52] B. D. Cullity, "Introduction to Magnetic Materials", Addison-Wesley Publishing, (1972).
- [53] B. D. Cullity, "Introduction to Magnetic Materials", Addison-Wesley Publishing, (1972).
- [54] Reitz, Milford, Chrisly, *Foundations of Electromagnetic Theory* ", 3rd Ed. Addison-Wesley Publishing Company, London (1979).
- [55] E.Veena Gopalan, , and M. R. Anantharaman. "On the Synthesis and Multifunctional Properties of Some Nanocrystalline Spinel Ferrites and Magnetic Nanocomposites." PhD diss., Cochin University of Science and Technology, (2009).
- [56] A. Muhammad ,Ph. D. Thesis, physics Department, Quaid-i-Azam University, Islamabad, Pakistan. (2008).
- [57] Rabani, Joseph, et al. "Fundamental Reactions In Illuminated Titanium Dioxide Nanocrystallite Layers Studied By Pulsed Laser." *The Journal of Physical Chemistry B* 102.10 (1998): (1689-1695).
- [58] R. Valenzuela, *Magnetic Ceramics: Capitulo 2. Preparation of Magnetic Ceramics*. Ed. Cambridge, Cambrigge, USA, (1994).
- [59] T. H. Mubarak, K. H. Hassan, and N. Z. Khalaf, "Preparation of Barium Ferrite Nanoparticles in Ethanol/Water Media and Study of its Physical Properties," *International Journal of Current Research*, Vol. 6, no. 4, pp. 6213-6217, 2014.
- [60] M. S. Reddi, M. Ramesh, T. Sreenivasu, G. Rao, and K. Samatha, "Investigation Of Structural, Magnetic And Dielectric Properties Of Cr<sup>3+</sup> Substituted Cu<sub>0.75</sub>co<sub>0.25</sub>fe<sub>2</sub>-Xo<sub>4</sub> Ferrite Nanoparticles," 2nd International Conference on Condensed Matter and Applied Physics (ICC 2017), pp. 030202, (2018).
- [61] N. Sivakumar, A. Narayanasamy, N. Ponpandian, and G. Govindaraj, "Grain

## References

---

- Size Effect On The Dielectric Behavior Of Nanostructured Ni<sub>0.5</sub>Zn<sub>0.5</sub>Fe<sub>2</sub>O<sub>4</sub>,” *Journal Of Applied Physics*, Vol. 101, no. 8, pp. 084116, (2007).
- [62] K. J. Standley, *Oxide Magnetic Materials: 2nd ed.*, Clarendon Press, Oxford, (1972).
- [63] W. Bragg, “The Structure Of Magnetite And The Spinel,” *Nature*, Vol. 95, No. 2386, pp. 561-561, (1915).
- [64] R. J. Hill, J. R. Craig, and G. Gibbs, “Systematics Of The Spinel Structure Type,” *Physics And Chemistry Of Minerals*, Vol. 4, No. 4, pp. 317-339, (1979).
- [65] D. S. Mathew, and R.-S. Juang, “An Overview Of The Structure And Magnetism Of Spinel Ferrite Nanoparticles And Their Synthesis In Microemulsions,” *Chemical engineering journal*, Vol. 129, No. 1-3, pp. 51-65, (2007).
- [66] N. Marcuvitz “Waveguide Handbook” Institution of Electrical Engineers, New York, (1985).
- [67] Nicola A. Spaldin, “Magnetic Materials: Fundamentals and Device Applications”, Cambridge University Press, (2003) .
- [68] N. A. Spaldin, *Magnetic Materials: Fundamentals And Applications: 2nd Edition*. Cambridge, New York, (2010).
- [69] R. Valenzuela, “Novel Applications Of Ferrites,” *Physics Research International*, vol. (2012), (2012).
- [70] N. A. Spaldin, *Magnetic Materials: Fundamentals And Applications: 2nd Edition*. Cambridge, New York, (2010).
- [71] R. Valenzuela, “Novel Applications Of Ferrites,” *Physics Research International*, vol. (2012), (2012).
- [72] E. Garskaite, K. Gibson, A. Leleckaite, J. Glaser, D. Niznansky, A. Kareiva, and H.-J. Meyer, “On The Synthesis And Characterization Of Iron-Containing Garnets (Y<sub>3</sub>Fe<sub>5</sub>O<sub>12</sub>, YIG and Fe<sub>3</sub>Al<sub>5</sub>O<sub>12</sub>, IAG),” *Chemical physics*, Vol. 323, No. 2-3, pp. 204-210, (2006).

## References

---

- [73] M. N. Akhtar, M. A. Khan, M. Ahmad, G. Murtaza, R. Raza, S. Shaukat, M. Asif, N. Nasir, G. Abbas, and M. Nazir, "Y<sub>3</sub>Fe<sub>5</sub>O<sub>12</sub> Nanoparticulate Garnet Ferrites: Comprehensive Study On The Synthesis And Characterization Fabricated By Various Routes," *Journal Of Magnetism And Magnetic Materials*, Vol. 368, pp. 393-400, (2014).
- [74] K. J. Standley, "Oxide Magnetic Materials" 2nd ed., Oxford University Press, (1972).
- [75] Fernando Arteaga-Cardona, Umapada Pal, José María Alonso, Patricia de la Presa, María-Eugenia Mendoza-Álvarez, Ulises Salazar-Kuri and Miguel Á. Méndez-Rojas, " Tuning Magnetic And Structural Properties Of MnFe<sub>2</sub>O<sub>4</sub> Nanostructures By Systematic Introduction Of Transition Metal Ions M<sup>2+</sup> (M= Zn, Fe, Ni, Co) " *Journal of Magnetism and Magnetic Materials*, Vol. 490: 165496, (2019).
- [76] Ihab Obaidat, Bashar Issa, Virendra Mohite and Yousef Haik, "Controlling the Curie-temperature of Magnetic Nanoparticles for Hyperthermia" , *Dynamic Biochemistry, Process Biotechnology and Molecular Biology*, Vol.5No.2, pp.85-88,(2011).
- [77] Yang Qu, Jianbo Li, Jie Ren, Junzhao Leng, Chao Lin, And Donglu Shi, " Enhanced Magnetic Fluid Hyperthermia By Micellar Magnetic Nanoclusters Composed Of Mn<sub>x</sub>Zn<sub>1-x</sub>Fe<sub>2</sub>O<sub>4</sub> Nanoparticles For Induced Tumor Cell Apoptosis " , *ACS applied materials and interfaces*, Vol.6, No.19, pp.16867-16879, (2014).
- [78] W. Ervens and H. Wilmesmeier, *Ullmann's Encyclopedia of Industrial Chemistry*, Fifth Edition, V, A16, P. 1-51, (1990).
- [79] Z. Yue, L. Li, J. Zhou, H. Zhang, and Z. Gui, "Preparation And Characterization Of NiCuZn Ferrite Nanocrystalline Powders By Auto-Combustion Of Nitrate-Citrate Gels," *Materials Science And Engineering: B*, Vol. 64, no. 1, pp. 68-72,(1999).

## References

---

- [80] N. Algarou, Y. Slimani, M. Almessiere, A. Baykal, S. Guner, A. Manikandan, and I. Ercan, "Enhancement On The Exchange Coupling Behavior Of SrCo<sub>0.02</sub>Zr<sub>0.02</sub>Fe<sub>11.96</sub>O<sub>19</sub>/MFe<sub>2</sub>O<sub>4</sub> (M= Co, Ni, Cu, Mn and Zn) As Hard/Soft Magnetic Nanocomposites," *Journal Of Magnetism And Magnetic Materials*, vol. 499, pp. 166308, (2020).
- [81] S. Hirosawa, A. Hanaki, H. Tomizawa and A. Hamamura, *Physica B*, V, 164, P. 117-123, (1990).
- [82] J.D. Livingston, "A review of coercivity mechanisms", *Journal. Appl. Phys*, P. 522-541, (1981).
- [83] Min Chen and David E. Nikles, *Nano Lett*, P. 211–214, (2002).
- [84] W. G. Hurley, and W. H. Wölflé, *Transformers And Inductors For Power Electronics: Theory, Design And Applications: John Wiley & Sons Ltd.*, (2013).
- [85] Soshin Chikazumi, "Book of Physics of Magnetism" Published by John Wiley and Sons. 554 pages (1964).
- [86] S. O. Kasap " Principles Of Electronic Materials And Devices" Published By Tata McGraw-Hill Education Pvt. Ltd., ISBN 10: 0070648204 / ISBN 13: 9780070648203 (2007).
- [87] V. Petkov, T. Ohta, Y. Hou, Y. Ren, "Atomic-Scale Structure of Nanocrystals by High-Energy X-ray Diffraction and Atomic Pair Distribution Function Analysis Nanoparticles" *J. Phys. Chem. C* 111, pp. 714-720, (2007).
- [88] R. Sharma, D. Bisen, U. Shukla, and B. Sharma, "X-ray Diffraction: A Powerful Method Of Characterizing Nanomaterials," *Recent Research In Science And Technology*, Vol. 4, No. 8, (2012).
- [89] R. Sharma, D. Bisen, U. Shukla, and B. Sharma, "X-ray Diffraction: A Powerful Method Of Characterizing Nanomaterials," *Recent Research In Science And Technology*, Vol. 4, No. 8, (2012).
- [90] F. Sher, " Crystal Structure Determination I", *Pakistan Institute of Engineering and Applied Sciences* ,1-20, (2010) .

## References

---

- [91] J. Connolly, "Elementary Crystallography for X-Ray Diffraction", Introduction to X-Ray Powder Diffraction, Springer, (2012).
- [92] A.K. Zak, "X-ray analysis of ZnO Nanoparticles by Williams one-Hall and Size Strain Plot Methods", Journal Solid State Sciences, (13), 251-256, (2011).
- [93] W. Ervens and H. Wilmesmeier, Ullmann's Encyclopedia of Industrial Chemistry, fifth edition, Vol, A16, Pp. 1-51, (1990).
- [94] Waqar Ahmed and Mark J. Jackson, "Emerging Nanotechnologies For Manufacturing", Micro and Nanotechnology Series, second ed., Elsevier, London, (2015).
- [95] Barbara H. Stuart, "Infrared Spectroscopy: Fundamentals and Applications", John Wiley and Sons, (2004).
- [96] G.D. Tang, Z.F. Shang, X.Y. Zhang, J. Xu, Z.Z. Li, C.M. Zhen, W.H. Qi, L.L. Lang, "evidence from infrared spectra for the magnetic moment directions of Cr Cations in the spinel ferrites (2015). Physica B: Condensed Matter, vol.463, pp.26-29,
- [97] A.V. Anupama, V. Rathod, V.M. Jali and B. Sahoo, "Composition Dependent Elastic And Thermal Properties Of Li-Zn ferrites", Journal of Alloys and Compounds, Vol.728, pp. 1091-1100, (2017).
- [98] Zeches, R.J.; Rossell, M.D.; Zhang, J.X.; Hatt, A.J.; He, Q.; Yang, C.-H.; Kumar, A.; Wang, C.H.; Melville, A.; Adamo, C.; Sheng, G.; Chu, Y.-H.; Ihlefeld, J.F.; Ederer, C.; Gopalan, V.; Chen, L.Q.; Schlom, D., "Strain-Driven Morphotropic Phase Boundary in BiFeO<sub>3</sub>", Science, Vol.326, No. 5955, pp.977-980, (2012).
- [99] S. Foner, "Versatile And Sensitive Vibrating-Sample Magnetometer," Review of Scientific Instruments, Vol. 30 No. 7, pp. 548-557, (1959).
- [100] S. K. Kulkarni, Nanotechnology: principles and practices: Capital Publishing Company, India, (2015).
- [101] J. He., "Synthesis And Dip-pen Nanolithographical Patterning Of Ferrite Nanoparticles," M.Sc. Thesis, University of Texas, Arlington (2010).

## References

---

- [102] K. H. Rao, S. B. Raju, K. Aggarwal and R. G. Mendiratta " Effect of Cr Impurity on the dc Resistivity of Mn-Zn ferrites " J. Appl. Phys. Vol. 52, 1376 (1981)
- [103] M. A. Wahab " The Effect Of Residual Strains On The Progressive Damage Modelling Of Environmentally Degraded Adhesive Joints" Pages 525-547, Vol. 19 (2005).
- [104] Eerenstein, W, Mathur, N. D and Scott, J. F., Nature" Multiferroic and Magnetoelectric Materials" Vol. 442, pp 759-765, (2006).
- [105] G. Shankaramurthy, "Studies On Electrical And Magnetic Properties Of Some Ferrites," (2009).
- [106] P. Phillips, T. Whall, and V. Brabers, "Hopping Conduction And Possible Coulomb Gap Effects In Manganese And Zinc Ferrous Ferrite," Philosophical Magazine B, Vol. 71, No. 1, pp. 23-39, (1995).
- [107] Y. Fukuda, S. Nagata, and K. Echizenya, "Electrical Conductivity of MnZn Ferrite Single Crystals With A Small Number of Fe<sup>2+</sup> ions," Journal Of Magnetism And Magnetic Materials, vol. 279, No. 2-3, pp. 325-330, (2004).
- [108] E. Verwey, P. Haayman, and F. Romeijn, "Physical Properties And Cation Arrangement Of Oxides With Spinel Structures II. Electronic Conductivity," The Journal Of Chemical Physics, Vol. 15, No. 4, pp. 181-187, (1947).
- [109] W. D. Kingery, H. K. Bowen, and D. R. Uhlmann, "Introduction To Ceramics , Wiley New York, (1976).
- [110] Brian S. Mitchell, " An Introduction to Materials Engineering and Science for Chemical and Materials Engineers John Wiley & Sons,, (2004).
- [111] J. Crangle, "Solid State Magnetism", Edward Arnold: London, U.K., (1991).
- [112] D. L. Leslie-Pelecky, and R. D. Rieke, "Magnetic Properties Of Nanostructured Materials", Chemistry of Materials, vol. 8, No. 8, pp. 1770-1783, (1996).

## References

---

- [113] D. Gubbins, and E. Herrero-Bervera, "Encyclopedia of geomagnetism and paleomagnetism" Springer, Berlin, (2007).
- [114] Hauser, H., Jiles, D. C., Melikhov, Y., Li, L., & Grössinger, R. (2006). An approach to modeling the dependence of magnetization on magnetic field in the high field regime. *Journal of Magnetism and Magnetic Materials*, 300(2), 273-283.
- [114] Brian S. Mitchell, "An Introduction to Materials Engineering and Science for Chemical and Materials Engineers" John Wiley & Sons., (2004).
- [115] Burda, C.; Chen, X.; Narayan, R.; El-Sayed, M. A. *Chem. Rev.* 105, 1025, (2005).
- [116] Park, J.; Privman, V.; Matijevic, E. *J. Phys. Chem. B*, 11630, (2001)
- [117] Ting Ke Tseng, Yi Shing Lin, Yi Ju Chen and Hsin Chu, "A Review of Photo catalysts Prepared by Sol-Gel Method for VOCs Removal", *International Journal of Molecular Sciences*, No.11, pp2336-2361, (2010).
- [118] James D. Patterson, Bernard C. Bailey, "Solid State Physics Introduction to the Theory", Springer-Verlag Berlin Heidelberg, (2007), p.(509), (2007).
- [119] Jassim, K. A., Fadhil, N. Q., & Mahdi, S. H. (2016). Study The Effect Of (y<sub>2</sub>o<sub>3</sub>, sbo<sub>2</sub>) Additives On The Dielectrically Properties Of The [Hg-1223] Compounds. *IJST*, 11(1), 129.
- [120] Choroszucho, A., & Butryło, B. (2013). Wpływ Materiałów Budowlanych Na Rozkład Pola Elektromagnetycznego Wewnątrz Pomieszczenia Mieszkalnego Zaprojektowanego W Różnych Technologiach Budowlanych. *Napędy i Sterowanie*, 15(6), 96-102.
- [121] R.A. Levy, "Principle Of Solid State Physics", 4th Edition, Academic Press (1976)

## References

---

- [122] West, A. R. Solid State Chemistry and its Applications; John Wiley & Sons:Singapore, (1989).
- [123] B. S. Mitchell, An Introduction To Materials Engineering And Science For Chemical And Materials Engineers: John Wiley & Sons,( 2004).
- [124]C. Ragupathi, J. J. Vijaya, L. J. Kennedy, and M. Bououdina,“Combustion Synthesis, Structure, Magnetic And Optical Properties OfCobalt Aluminate Spinel Nanocrystals,” *Ceramics International*, Vol. 40, No. 8, pp. 13067-13074,( 2014).
- [125] V. Rajendran, A. Marikani, Materials Science, Tata McGraw-Hill PublishingCompany Limited, New Delhi, (2004).
- [126] B. S. Mitchell, An Introduction To Materials Engineering And Science For Chemical And Materials Engineers: John Wiley & Sons, (2004).
- [127] V. Rajendran, A. Marikani, Materials Science, Tata McGraw-Hill PublishingCompany Limited, New Delhi, (2004).
- [128] B. S. Mitchell, An Introduction To Materials Engineering And Science For Chemical And Materials Engineers: John Wiley & Sons,( 2004).
- [129] V. Rajendran, A. Marikani, Materials Science, Tata McGraw-Hill PublishingCompany Limited, New Delhi, (2004).
- [130] B. S. Mitchell, An Introduction To Materials Engineering And Science For Chemical And Materials Engineers: John Wiley & Sons, (2004).
- [131] Abdullah, M. Z., Al-Timimi, M. H., Albanda, W. H., Dumitru, M., Balan, A.E., Ceaus, C., ... & Stamatina, I. (2019). Structural And Electrochemical Properties Of  $P3-Na0.67Mn0.3Co0.7O2$  Nanostructures Prepared By Citric-Urea Self-Combustion Route As Cathode For Sodium Ion Battery. *Digest Journal Of Nanomaterials And Biostructures*, 14(4), 1179-1193.
- [132] Rath, C., Anand, S., Das, R. P., Sahu, K. K., Kulkarni, S. D., Date, S. K., & Mishra, N. C. (2002). Dependence On Cation Distribution Of Particle Size, Lattice Parameter, And Magnetic Properties In Nanosize Mn–Zn

## References

---

- ferrite. *Journal of Applied Physics*, 91(4), 2211-2215.
- [133] Varshney, D., Verma, K., & Kumar, A. (2011). Structural and Vibrational Properties Of  $Zn_xMn_{1-x}Fe_2O_4$  ( $x= 0.0, 0.25, 0.50, 0.75, 1.0$ ) Mixed Ferrites. *Materials Chemistry And Physics*, 131(1-2), 413-419.
- [134] Sarala, E., Madhukara Naik, M., Vinuth, M., Rami Reddy, Y. V., & Sujatha, H. R. (2020). Green Synthesis Of Lawsonia Inermis-Mediated Zinc Ferrite Nanoparticles For Magnetic Studies And Anticancer Activity Against Breast Cancer (MCF-7) cell lines. *Journal of Materials Science: Materials in Electronics*, 31(11), 8589-8596.
- [134] S.H. Vajargah, H.R.M. Hosseini, Z.A. Nemat, J. Alloys Compd. 430 (2007) 339–343.
- [135] M.J.N. Isfahani, M. Myndyk, D. Menzel, A. Feldhoff, J. Amighian, V. Sepelak, J. Magn. Mater. 321 (2009) 152–156.
- [136] Ge, Y., Lakshmipriya, T., Gopinath, S. C., Anbu, P., Chen, Y., Hariri, F., & Li, L. (2019). Glucose Oxidase Complexed Gold-Graphene Nanocomposite On A Dielectric Surface For Glucose Detection: A Strategy For Gestational Diabetes Mellitus. *International Journal of Nanomedicine*, 14, 7851.
- [137] Rahimi, R., Kerdari, H., & Rabbani, M. (2010, November). Adsorptive Removal Of Crystal Violet (CV), A Carcinogenic Textile Dye, From Aqueous Solution By Conducting Polyaniline/Hollow Manganese Ferrite Nanocomposites. In *Proceedings of the ECSOC-14: the 14th International Electronic Conference On Synthetic Organic Chemistry, Basel, Switzerland* (pp. 1-30).
- [138] Manohar, A., Krishnamoorthi, C., Pavithra, C., & Thota, N. (2021). Magnetic Hyperthermia And Photocatalytic Properties Of  $MnFe_2O_4$  Nanoparticles Synthesized By Solvothermal Reflux Method. *Journal of Superconductivity and Novel Magnetism*, 34(1), 251-259.
- [139] Wiriya N, Bootchanont A, Maensiri S and Swatsitang E 2014 Magnetic

## References

---

- Properties of  $Zn_{1-x}Mn_xFe_2O_4$  Nanoparticles Prepared By Hydrothermal Method *Microelectron. Eng.* 126 1– 8
- [140] Suharyadi, E., Setiadi, E. A., Shabrina, N., Kato, T., & Iwata, S. (2014). Magnetic Properties And Microstructures Of Polyethylene Glycol (PEG)-Coated Cobalt Ferrite ( $CoFe_2O_4$ ) Nanoparticles Synthesized By Coprecipitation Method. In *Advanced Materials Research* (Vol. 896, pp. 126-133). Trans Tech Publications Ltd.
- [141] S.J. Moeen, M.R. Vaezi, A.A. Yousefi, *Prog. Color Colorants Coat.* 3, 9 (2010).
- [142] Wang, K.; Jinwen, G.; Yin, N. Efficient Removal of Pb (II) and Cd (II) Using  $NH_2$ -functionalized Zr-MOFs via Rapid Microwave-promoted Synthesis. *Ind. Eng. Chem. Res.* 2017, 56(7), 1880–1887. DOI: 10.1021/acs.iecr.6b04997.
- [143] Alamery, N.; Abid, H. R.; Wang, S. Adsorptive Study of Removing Harmful Dye (Methyl Orange) by Three Types of UiO-66 Metal Organic Framework. *Chemeca.* 2018, 2018, 156.
- [144] Nasehi, Pedram; Abbaspour, Seyed Foad; Rafiee, Masoud; Moghaddam, Mojtaba Saei (2020).
- [145] Chichiriccò, G., & Poma, A. (2015). Penetration And Toxicity Of Nanomaterials In Higher 461 plants. *Nanomaterials*, 5(2), 851-873.
- [146] Tombuloglu, Huseyin; Tombuloglu, Guzin; Slimani, Yassine; Ercan, Ismail; Sozeri, Hüseyin; Baykal, Abdulhadi (2018).
- [147] Köseoğlu, Y., Baykal, A., Toprak, M. S., Gözüak, F., Başaran, A. C., & Aktaş, B. (2008). Synthesis And Characterization Of  $ZnFe_2O_4$  Magnetic Nanoparticles Via A Peg-Assisted Route. *Journal of Alloys and Compounds*, 462(1-2), 209-213.
- [148] Rostami, Mojtaba; Rahimi-Nasrabadi, Mehdi; Ganjali, Mohammad Reza; Ahmadi, Farhad; Shojaei, Abdollah Fallah; Delavar Rafiee, Mahboube (2017). *Facile Synthesis And Characterization Of  $TiO_2$ –*

## References

---

*graphene– ZnFe<sub>2–x</sub>TbxO<sub>4</sub>ternary Nano-Hybrids.*

- [149] P. Tiwari, R. Verma, S.N. Kane, T. Tatarchuk, F. Mazaleyrat, Effect of Zn Addition On Structural, Magnetic Properties And Antistructural Modeling Of Magnesium-Nickel Nano Ferrites. *Mater. Chem. Phys.* 229, 78–86 (2019)
- [150] S. Rahman, K. Nadeem, M. Anis-ur-Rehman, M. Mumtaz, S. Naeem, I. Letofsky-Papst, Structural And Magnetic Properties Of ZnMg-ferrite Nanoparticles Prepared Using The Co-Precipitation Method. *Ceram. Int.* 39(5), 5235–5239 (2013)
- [151] S. Hajarpour, A.H. Raouf, K. Gheisari, Structural Evolution And Magnetic Properties Of Nanocrystalline Magnesium–Zinc Soft Ferrites Synthesized By Glycine–Nitrate Combustion Process. *J. Magn. Magn. Mater.* 363, 21–25 (2014)
- [152] Abdel Maksoud, M. I. A., El-Sayyad, G. S., Abokhadra, A., Soliman, L. I., El-Bahnasawy, H. H., & Ashour, A. H. (2020). Influence of Mg<sup>2+</sup> Substitution On Structural, Optical, Magnetic, And Antimicrobial Properties of Mn–Zn Ferrite Nanoparticles. *Journal Of Materials Science: Materials In Electronics*, 31(3), 2598-2616.
- [153] K.W. Wagner, Theory Of Imperfect Dielectrics. *Ann. Phys.* 345, 817 (1913)
- [154] C.G. Koops, On The Dispersion Of Resistivity And Dielectric Constant Of Some Semiconductors At Audio Frequencies. *Phys. Rev.* 83, 121 (1951).
- [155] P. Ben-Ishai, E. Sader, Y. Feldman, I. Felner, M. Weger, Dielectric Properties of Na<sub>0.7</sub>CoO<sub>2</sub> And Of The Superconducting Na<sub>0.3</sub>CoO<sub>2</sub>·1.3 H<sub>2</sub>O. *J. Supercond.* 18,455 (2005)
- [156] A.K. Pradhan, S. Saha, T.K. Nath, *Appl. Phys. A.* 123, 715(2017)
- [157] N. Ahmad, S. Khan, M.M.N. Ansari, *Ceram. Int.* 44,15972–15980(2018).

## References

---

- [158] M. Naveed, M. Mumtaz, R. Khan, A.A. Khan, M. Nasir Khan, Conduction Mechanism And Impedance Spectroscopy Of (MnFe<sub>2</sub>O<sub>4</sub>) X/Cutl-1223 Nanoparticles-Superconductor Composites. *J. Alloys Comp.* 712, 696 (2017)
- [159] H. Zhang, S.-S. Yu, H.-B. Duan, A Hybrid Crystal With High Dielectric Constant And Relaxation Dielectric Behavior. *Inorg. Chem. Commun.* 93, 1–5 (2018)
- [160] M. T. Ramesan, V. Santhi, B. K. Bahuleyan, M. A. Al-Maghrabi, *Mater. Chem. Phys.* 2018, 211, 343.

## الخلاصة

الهدف من هذه الرسالة هو تصنيع ودراسة الخصائص التركيبية والمغناطيسية والكهربائية للجسيمات النانوية المحضرة من المنغنيز والزنك الفريت باستخدام الصيغة المتكافئة  $Zn_xMn_{1-x}Fe_2O_4$  (x=0,0.15,0.25,0.35,0.45) على التوالي ، تم تحضيرها باستخدام عملية الاحتراق التلقائي سول جل. بعد الاحتراق ، تم تكلسنة المساحيق المحترقة عند 650 و 750 و 850 درجة مئوية لمدة ساعتين لزيادة التجانس وإزالة المتبقيات العضوية ، حيث العينات المحترقة والتي تم تكلسها عند 650 و 750 و 850 درجة مئوية. يضاف لها PVA خمسة قطرات كمادة رابطة للضغط عليه في اقراص دائرية قطرها 1 سم وسمكها 3 مم. تم تلييد الاقراص المحضرة عند 400 و 600 و 800 لمدة ساعتين لتكثيف العينات ، وتم السماح لها ببطء بتبريدها بشكل طبيعي لفحص الخصائص العازلة. والغرض الآخر من هذا العمل هو مزج  $TiO_2$  ودراسة الخصائص الهيكلية والمغناطيسية والكهربائية. للمنغنيز والزنك الفريت والمركبات النانوية عند 500 باستخدام الصيغة  $Zn_xMn_{1-x}Fe_2O_4 / TiO_2$  بنسب مختلفة (20% ، 30% ، 40% ، 50% و 60%) على التوالي. محضرة بطريقة السيراميك التقليدية. في الفريت المنتج من Mn-Zn. في حالة Mn-Zn-ferrites و  $TiO_2$  أفضل النتائج الحجم الحبيبي في هذا البحث كانت بحجم 15 إلى 38 نانومتر مع هيكل مكعب الذي تحديده بواسطة XRD، بينما كان الحجم الحبيبي لل Mn-Zn-ferrites /  $TiO_2$  من 10 إلى 30 نانومتر مع هيكل مكعب يحدده حيود الأشعة السينية (XRD) التحليلات. تم العثور على FE-SEM للنانو فرايت ( $ZnMnFe_2O_4$ ) بحجم جسيمي من 25 إلى 66 نانومتر. بينما يتراوح حجم الجسيمي للمركب النانوي  $Zn_xMn_{1-x}Fe_2O_4 / TiO_2$  من 37 إلى 72 نانومتر. لاحظت أن النتيجة أقل من مركب نانو  $Zn-Mn-Fe_2O_4$ .

أشارت قمم امتصاص FT-IR عند 400 و 500 سم<sup>-1</sup> إلى وجود نطاقات اهتزازية Fe-O و Mn-O و Zn-O. أظهرت النتائج من VSM أن الطبيعة المغناطيسية للمواد تغيرت بشكل كبير مع زيادة المغنطة وتناقصت بشكل قسري مع Mn-Zn-ferrites nanoparticles. أخيرًا ، تم الحصول على قيمة المعلمة المغناطيسية المثلى ( $M_s = 0.80 \text{ emu / g}$  و  $H_c = 75 \text{ Oe}$ ) عند (850 °C) من البيانات. يتم قياس خصائص العزل الكهربائي باستخدام مقياس (LCR) في نطاق تردد (200 هرتز - 1 ميجاهرتز) عند درجة حرارة الغرفة. ثابت العزل الكهربائي ( $\epsilon'$ )، زاوية فقدان العزل الكهربائي ( $\tan\delta$ ) وعامل فقد العزل الكهربائي ( $\epsilon''$ ) هي للفريتات النانوية  $Mn-Zn-Fe_2O_4$  عند 400 و 600 و 800 °C و Mn-Zn- $Fe_2O_4 / TiO_2$  nanocomposites بنسب مختلفة (20% ، 30% ، 40% ، 50% و 60% على التوالي) وجد

أنها تنخفض مع زيادة درجات الحرارة. تم تلييد الاقراص المحضرة عند 500C لمدة ساعتين لتكثيف العينات والسماح لها ببطء بالتبريد بشكل طبيعي لفحص الخواص العازلة.



جمهورية العراق  
وزارة التعليم العالي  
والبحث العلمي  
جامعة ديالى  
كلية العلوم  
قسم الفيزياء

الخصائص التركيبية والكهربائية والمغناطيسية للفائق المغناطيسي زنك - منغنيز نانو  
فرايت الممزوج بثنائي اوكسيد التيتانيوم  
رسالة مقدمة

الى مجلس كلية العلوم جامعة ديالى استيفاء جزئي لمتطلبات درجة ماجستير العلوم في الفيزياء

من قبل

مثنى الطيف عباس

(بكالوريوس علوم الفيزياء 2007-2006)

بأشراف

ا.م. زينة محمد علي عباس

١٤٤٣ هـ

٢٠٢٢ م